Confronting the new generation of stellar model atmospheres with observations

Tiago Mendes Domingos Pereira

A thesis submitted for the degree of

Doctor of Philosophy

of The Australian National University

THE AUSTRALIAN NATIONAL UNIVERSITY

Research School of Astronomy & Astrophysics

September 2009

She held up a small crystal phial: it glittered as she moved it, and rays of white light sprang from her hand. “In this phial,” she said, “is caught the light of Eärendil’s star, set amid the waters of my fountain. It will shine still brighter when night is about you. May it be a light to you in dark places, when all other lights go out.”

J. R. R. Tolkien
The Fellowship of the Ring

Disclaimer

I hereby declare that the work in this thesis is that of the candidate alone, except where indicated below.

Chapter 2, has been submitted as a paper to the international journal *Astronomy & Astrophysics*. It is co-authored by M. Asplund, R. Trampedach and R. Collet. They have provided the 3D solar model atmosphere that is used throughout the thesis, helped to write §2.2.1, and provided suggestions and comments to the manuscript.

Chapters 3 and **4** have been accepted for publication in *Astronomy & Astrophysics*, and are currently in press. They are co-authored with D. Kiselman and M. Asplund. The solar observations were obtained by the candidate and D. Kiselman, who provided programs that were used to build the initial part of the data reduction pipeline. The data selection, reduction and analysis were performed by the candidate. M. Asplund helped to write §3.4.1. Both co-authors helped in the interpretation of the results and provided suggestions and comments for the manuscripts of the chapters.

Tiago M. D. Pereira
21st September 2009

Acknowledgments

It is a difficult task to choose who to thank first. A few years have passed, and so many people helped me though my thesis, in so many ways. But first I would like to thank my supervisor, Martin Asplund. Without Martin's never-ending enthusiasm, encouragement and support (many times from half-way around the globe), this thesis would never have been possible. It was a big step to come all the way to Australia to work with a supervisor I had never met. But it was definitely worth it. I have learned a lot from your dedication, positiveness and rigour. Thank you Martin, for all your help!

I would also like to thank my other supervisor, Dan Kiselman. This thesis is greatly indebted to your attention to detail and meticulousness. And I am most thankful for your hospitality and generosity in taking me as a Marie Curie trainee in Stockholm. I had a great time in Sweden, both scientifically and personally. I apologise for not being able to speak much Swedish yet – it was one of my goals for the three-month stay. At the moment I cannot say much more than tack så mycket!

I am also indebted to my wife Catherine. My achievements (our achievements) would not have been possible without your constant love and support. Thank you for all your strength to go through the hard times, for managing things very gracefully and for being the wonderful person you are. To my family in Portugal, in particular my parents, thank you for your constant support in helping me to come here and do my thesis. I would also like to thank my dear friends Jacqueline, Fred, Simon, Nic, Wolfgangs (yes, both of you), Eduard, the students at Stromlo and the people at the ANU Mountaineering club who shared the Australian outdoors with me. I am very fortunate to have met you all.

A special thank you also goes to everyone at Stromlo for their warm welcome and help, and for making Stromlo a great place to be. I thank my local supervisor Mike Bessell, for his care in making sure everything was going well in Martin's absence. And I would also like to thank the other member of my supervisory panel, Regner Trampedach, for always having an open door and helping me in all the problems I came up to you.

I gratefully acknowledge the financial support from a PhD scholarship from Fundação para a Ciência e Tecnologia, ref. SFRH/BD/21888/2005, as well as from the ANU RSAA for the last months of my thesis, and the ANU top-up scholarship. I also acknowledge the support from the USO-SP International Graduate School for Solar Physics under a Marie Curie Early Stage Training Fellowship (project MEST-CT-2005-020395) from the European Union. This research has been partly funded by a grant from the Australian Research Council (DP0558836).

In no particular order, I would like to thank Andreas Schweitzer and Peter Hauschildt for kindly providing the PHOENIX models; Paul Barklem for providing me with his hydrogen and electron collisional data; Sven Wedemeyer-Böhm for his observed and synthetic intensity distributions; Carlos Allende Prieto for providing his straylight code; Pit Sütterlin for his kind assistance with the Dutch Open Telescope; Nicolas Grevesse for fruitful discussions and many good dinners in Garching; Jacques Sauval for his help and data from the molecular line database and Jaime de la Cruz Rodríguez for helping at the SST. The Swedish 1-m Solar Telescope is operated on the island of La Palma by the Institute for Solar Physics of the Royal Swedish Academy of Sciences in the Spanish Observatorio del Roque de los Muchachos of the Instituto de Astrofísica de Canarias.

Abstract

Stellar model atmospheres are a fundamental tool for our understanding of stars. Because the chemical composition of stars cannot be measured directly, the inferred stellar parameters are model dependent. In recent years great progress has been made in the modeling of stellar atmospheres, allowing the relaxation of simplifying assumptions made in previous models. The use of new 3D model atmospheres to infer the solar chemical composition has resulted in a decrease of the solar metallicity. This result has caused some controversy and is being challenged.

The main aim of this thesis is to ascertain if the new models of stellar atmospheres are realistic and can be trusted to derive the chemical composition of stars in general, and the Sun in particular. Other objectives also include the study of line formation in the Sun at high spatial resolution, and possible implications in the modeling.

The Sun is the ideal test-bench for detailed analyses of stellar atmospheres. With the solar surface being resolved in great detail and at different viewing angles, a wealth of information can be gathered that allows for very robust tests of atmosphere models. The testing detailed here addresses several fronts. On one hand, the model's temperature structure is directly tested with the classical tests of continuum centre-to-limb variations and absolute fluxes. On the other hand, the line formation is tested at different viewing angles and high spatial and spectral resolution. Here the main focus is on oxygen lines, as oxygen has an important contribution for the total solar metallicity. However, other lines are also tested. High quality data were specifically obtained for these line formation tests, using the Swedish 1-m Solar Telescope.

For the temperature structure tests we find a surprisingly good agreement between the 3D model and the observations, surpassing even semi-empirical models. The solar 1D non-LTE models have a very similar behaviour to 1D LTE models, confirming that LTE is a good approximation in the solar photosphere. The 3D theoretical model performs consistently better than its 1D counterparts. The oxygen line formation tests are carried out in great detail, with a careful wavelength calibration, revised atomic data, and allowing for departures from LTE. Again we find a reassuring agreement between the 3D model predictions and the observations, both for the centre-to-limb variation of the lines and the line formation at high spatial resolution. The observations at different viewing angles also allowed the empirical determination of the role of hydrogen collisions with oxygen, important when deriving the oxygen abundance.

The tests undertaken here show that the 3D model atmospheres are indeed very realistic. Their predicted temperature structure and velocity fields compare very favourably with observations of the Sun. Together with previous tests, this indicates they can be relied upon to derive the chemical composition of the Sun and similar late-type stars.

CONTENTS

Disclaimer . . . i

Acknowledgments . . . ii

Abstract . . . iii

Table of contents . . . v

List of figures . . . ix

List of tables . . . xiii

1 Introduction **1**

1.1 Why stellar photospheres are important . . . 2

1.2 Classical models of stellar atmospheres . . . 3

1.3 The new generation of stellar model atmospheres . . . 5

1.4 The solar interior modeling crisis . . . 8

1.5 More testing is needed for the new models . . . 10

1.6 Thesis outline . . . 11

2 How realistic are solar model atmospheres? **13**

2.1 Introduction . . . 14

2.2 Model atmospheres . . . 15

2.2.1 3D Model . . . 15

2.2.2 1D Models . . . 16

2.3 Continuum centre-to-limb variations . . . 19

2.3.1 Context . . . 19

2.3.2 Observations . . . 19

2.3.3 Results and discussion . . . 20

2.4 Absolute flux distribution 23
2.4.1 Context 23
2.4.2 Observations 23
2.4.3 Results and discussion 24
2.5 Continuum intensity distribution 26
2.6 Conclusions 27

3 Oxygen lines in solar granulation at high resolution 29
3.1 Introduction 30
3.2 Observations 31
3.2.1 Telescope, instruments and programme 31
3.2.2 Pointing accuracy 33
3.3 Data reduction 33
3.3.1 Dark currents, flat fields and spectrograph distortions 33
3.3.2 Wavelength and intensity calibrations 34
3.3.3 Correction for straylight in the spectrograph 35
3.3.4 Normalization 36
3.3.5 Frame selection and sampling 37
3.3.6 Fourier filtering 38
3.3.7 Extracting line quantities 39
3.4 Simulations 40
3.4.1 Atmospheric model 40
3.4.2 Line formation and departures from LTE 41
3.4.3 Atomic data 42
3.4.4 Image degradation and instrumental profiles 43
3.5 Results and discussion 46
3.5.1 Line shifts 46
3.5.2 Line strengths 48
3.5.3 Line asymmetries 50
3.5.4 Line FWHM 51
3.5.5 Departures from LTE in oxygen lines 53
3.5.6 Summary quantities of line variations 55
Definitions 55
Results 56
3.6 Conclusions 59

4 **Centre-to-limb variation of solar oxygen lines** **61**
  4.1 Introduction 62
  4.2 Observations 63
    4.2.1 Overview 63
    4.2.2 Comparison with previous studies 64
  4.3 Theoretical line profiles 68
  4.4 Results 69
    4.4.1 O I infrared triplet 69
      Context 69
      Comparison with observations 70
      Comparison with previous work 75
      Effect of blends and electron collisions on the inferred S_{H} and abundances 75
    4.4.2 [O I] 630.03 nm and Ni I blend 76
      Context 76
      Ni I blend 76
      Wavelength calibration 77
      Continuum level and fitting range 78
      Comparison with observations 79
      Comparison with previous work 81
    4.4.3 O I 615.81 nm 81
      Context 81
      Wavelength calibration 82
      Molecular blends and comparison with observations 83
    4.4.4 Lines from other species than O I 85
  4.5 Conclusions 87

5 **Summary and future outlook** **89**
  5.1 Chapter 2 90
  5.2 Chapter 3 90
  5.3 Chapter 4 91
  5.4 Where to, from here? 92

References **93**

Appendices **99**

A Results for the old 3D model **101**

A.1 From Chapter 2 101

A.2 From Chapter 3 104

A.3 From Chapter 4 111

B Line quantities in solar granulation **117**

LIST OF FIGURES

1.1 Temperature structure of the solar atmosphere 2
1.2 The solar atmosphere in the spectral continuum around 436.4 nm 6
1.3 Effect of the new abundances on the solar interior models 8
1.4 The solar chemical composition 9
1.5 Solar oxygen abundance over the last 80 years 10

2.1 Temperature structure of the 3D and 1D models 18
2.2 Continuum centre-to-limb observations 19
2.3 Continuum centre-to-limb variations in the visible/infrared 20
2.4 Continuum centre-to-limb variations in the near infrared 21
2.5 Difference between observations and models in the centre-to-limb variation 22
2.6 Comparison of original absolute fluxes, continuum fluxes and 3D model 24
2.7 Absolute continuum fluxes for the models and observations 25
2.8 Continuum flux differences between the models and the observations . . 26
2.9 Continuum intensity distributions 26

3.1 Position of the observations on the solar disk 33
3.2 Normalization of the mean spectrum 36
3.3 Example spectrogram, before and after reduction 38
3.4 Effect of the Fourier filter in the spectra 39
3.5 Degrading the simulations to match the observations 45
3.6 Effects of different PSF shapes on the simulation degradation 46
3.7 Line shifts over the solar granulation 47
3.8 Equivalent widths over the solar granulation 49

3.9 Line asymmetries at disk-centre 50
3.10 Line asymmetries vs. line shifts 51
3.11 Line FWHM at disk-centre 52
3.12 NLTE effects on equivalent widths and FWHM 54
3.13 Variation of the α parameter with equivalent width 57
3.14 Variation of the γ parameter with E_{low} 58

4.1 Observed profiles of O I lines at disk-centre and limb 65
4.2 Observations of the centre-to-limb variation of O I 777 nm 67
4.3 Comparison of the mean temperature structure of the 3D models 68
4.4 NLTE effects in the centre-to-limb variation of O I 777 nm, 3D model . . 71
4.5 NLTE effects in the centre-to-limb variation of O I 777 nm, 1D models . . 72
4.6 Predicted line profiles for the 3D model at $\mu = 1, 0.2$ for different S_{H} . . 73
4.7 Variation of χ^2 with S_{H} for O I 777 nm 74
4.8 Line profile fits for [O I]+Ni I 630.03 nm 79
4.9 Centre-to-limb variation of equivalent width for [O I]+Ni I 630.03 nm . . 80
4.10 Line profile fits and effects of blends in O I 615.81 nm 82
4.11 Centre-to-limb variation of equivalent width for O I 615.81 nm 84
4.12 Centre-to-limb variation of equivalent width for other lines 86

A.1 Continuum centre-to-limb variations in the visible/infrared 102
A.2 Continuum centre-to-limb variations in the near infrared 102
A.3 Difference between observations and models in the centre-to-limb variation 103
A.4 Absolute continuum fluxes for the models and observations 103
A.5 Continuum flux differences between the models and the observations . . 104
A.6 Line shifts over the solar granulation 105
A.7 Equivalent widths over the solar granulation 106
A.8 Line asymmetries at disk-centre 107
A.9 Line FWHM at disk-centre 107
A.10 NLTE effects on equivalent widths and FWHM 108
A.11 Variation of the α parameter with equivalent width 109
A.12 Variation of the γ parameter with E_{low} 110
A.13 NLTE effects in the centre-to-limb variation of O I 777 nm, old 3D model 112
A.14 Predicted line profiles for the old 3D model at $\mu = 1, 0.2$ for different S_{H} 113
A.15 Variation of χ^2 with S_{H} for O I 777 nm 114
A.16 Line profile fits for [O I]+Ni I 630.03 nm 114

A.17 Centre-to-limb variation of equivalent width for [O I]+Ni I 630.03 nm . . 114
A.18 Line profile fits and effects of blends in O I 615.81 nm 115
A.19 Centre-to-limb variation of equivalent width for O I 615.81 nm 115
A.20 Centre-to-limb variation of equivalent width for other lines 116

B.1 Line shifts over the solar granulation, 615 nm region 118
B.2 Line shifts over the solar granulation, 630 nm region 119
B.3 Line shifts over the solar granulation, 777 nm region 120
B.4 Line asymmetries over the solar granulation 121
B.5 Line FWHMs over the solar granulation 122
B.6 Line minima over the solar granulation 123

LIST OF TABLES

2.1 Comparison of ΔI_{rms} between models and observations 27

3.1 Observing runs selected for analysis 32
3.2 Lines studied in the present work and their parameters 43

4.1 Observed centre-to-limb variation of equivalent widths 66
4.2 Derived oxygen abundances from O I 777 nm, for different S_{H} 74
4.3 Ni I isotopes used and scaled $\log gf$ values 77
4.4 Molecular lines included in the 615.8 nm region. 84

CHAPTER 1

Introduction

Our understanding of the Universe is closely linked to our understanding of stars. They are the basic building blocks of clusters, galaxies and other larger structures. Big and small, their life and death has a profound impact on their surroundings, from planetary systems to other stars and the interstellar medium. The evolution of galaxies is strongly influenced by the distribution of their stars, how they were formed, how they interact among themselves and with the surrounding gas. The repercussions of the study of stars on Astronomy, Astrophysics and Cosmology are immense. And yet, the amount of information we can gather from a star is essentially limited to the radiation that is emitted from very close to its surface. The interiors of stars are usually hot (by any standard) and often dense, which makes them opaque to the electromagnetic radiation. It is only in their surface, when the density and temperature drop, that the photons generated in the star's interior can travel freely to Earth and be detected. The inescapable consequence is that one must understand the surfaces of stars if one wants to understand stars, the Universe and everything else.

What happens in the surface of a star? First, the concept of 'surface' in a star is difficult to define. Stars are made of hot plasma, whose density decreases smoothly outwards, unlike in the Earth and other planets where the abrupt density transition between solid/liquid and the atmosphere defines a surface. In stars, the surface is not so obviously defined. The surface of a star is typically defined as the point where the majority of photons can travel freely. This does not happen at one single point, but at a range of depths. This range of depths is the region of the star where most of the light that reaches us is emitted. While the outer layers of a star are by definition called the atmosphere, this region where light is formed is called the photosphere[1]. So instead of "what happens in the surface of a star?", the question should really be "what happens in the photosphere of a star?". This question drives the motivation of this, and many other theses.

---

[1] The term is derived from the greek $\phi\omega\tau o\varsigma$ (*photos*, meaning light) and $\sigma\phi\alpha\iota\rho\alpha$ (*sphaira*, meaning ball).

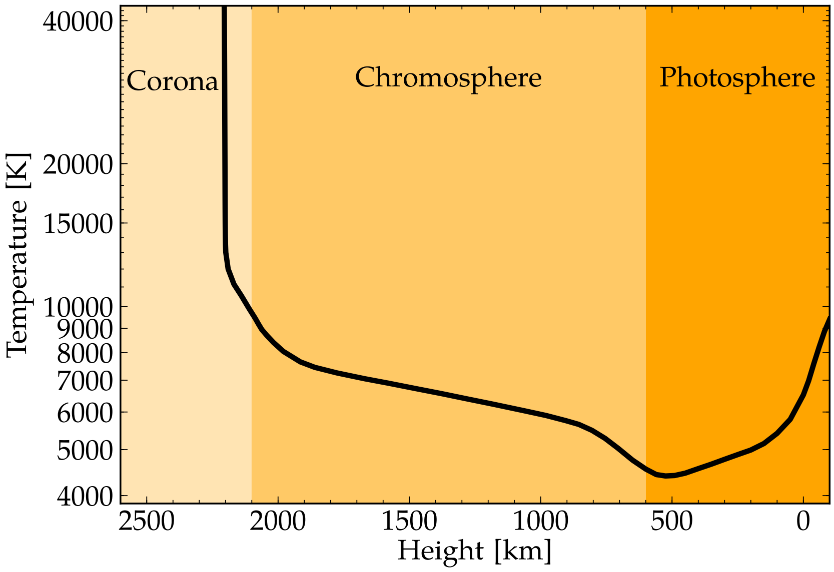

Figure 1.1 Temperature structure of the solar atmosphere, as given by the FAL III C semi-empirical model (Fontenla et al., 1993). Plotted against height, where zero is the surface (defined as where the optical depth at 500 nm reaches unity). This an idealized view to illustrate the different regions of the atmosphere. It represents the classical viewpoint from plane parallel models. The modern-day viewpoint emphasizes less on a static separation of different regions and more on the dynamics and structures taking place at different depths: granules, spicules, flux tubes, loops (Ayres, 1998; Rutten, 1998).

1.1. Why stellar photospheres are important

The radiation that reaches us from stars is in most cases the only tool available to study them. The stellar radiation has encoded information about its formation place, the photosphere. The photosphere is typically a very small layer when compared to the stellar radius. In the Sun its length is about 1000 km (to the solar radius, this thickness has a similar proportion as the apple skin to the apple). Despite its relatively thin size, the importance of the photosphere is considerable. Most of a star's spectrum is formed in the photosphere, making it the only region that can be extensively studied for the majority of stars.

A simplified view of the structure of the solar atmosphere, including the photosphere, is given in Fig. 1.1. Throughout this work the more loosely defined term 'atmosphere' will be used to refer to the photosphere, unless stated otherwise. This is because models of stellar photospheres are computed for the photosphere and surrounding regions, but usually do not include the chromosphere or other higher regions. Yet they are called models of stellar atmospheres, although they are constructed to study the photospheres.

It is of the utmost importance to understand the physical processes that take place in the photosphere so that information about the star can be inferred. Quantities like effective temperature, gravity, radius, rotation and chemical composition can be obtained by studying stellar photospheres.

The most interesting property that can be obtained through the study of photospheres and spectra is arguably the chemical composition of stars. The chemical composition traces the history of the Universe. It allows astronomers and cosmologists to trace the origin and evolution of elements, which ultimately provides insight in a multitude of disciplines. Its study can provide the answers to questions like how did the Big Bang create heavy elements, how galaxies form and evolve, which stellar systems have the conditions to host life, etc.

Observationally it is not possible to measure the chemical composition of stars directly. When all one has is the stellar light and its spectrum, there are too many unknowns. Instead, the usual approach is to build a model atmosphere. Theoretical model atmospheres are built from first principles physics, simulating the processes that take place in the atmosphere and deriving the temperatures, densities and pressures for the stellar atmosphere. A model atmosphere is then used to compute the theoretical or synthetic spectrum of the star. Comparing the theoretical and observed spectra, one can derive the chemical composition, the abundances of different elements. One of the consequences of this time tested method is that the extracted abundances are dependent on the assumed model of the atmosphere. Hence, realistic atmospheres are essential for a reliable determination of the elemental abundances from spectral lines, which has a far-reaching impact in many disciplines.

1.2. Classical models of stellar atmospheres

The modeling of stellar atmospheres varies greatly with the spectral type. The discussion onwards from this point concerns mainly late-type, cool stars. They are the most common types of stars found, because their evolutionary stages are the longest lived, and thus the most used in studies of galactic chemical evolution.

The term 'classical model atmospheres' generally refers to the models employing simplifying assumptions about radiative transfer, geometry and convection, which were historically employed in the first theoretical models of stellar atmospheres.

The first of these assumptions is that of local thermodynamical equilibrium (LTE). In LTE, collisions between the atoms and electrons ensure that the level populations and ionization fractions depend only on the local temperature, as given respectively by the Boltzmann and Saha equations. This is a powerful approximation, and also implies that the source function S_ν, which controls the ratio between emitted and absorbed radiation, can be approximated by $B_\nu(T)$, the Planck function. The source function is determinant in the radiative transfer equation:

$$\frac{\mathrm{d}I_\nu}{\mathrm{d}\tau_\nu} = S_\nu - I_\nu, \tag{1.1}$$

which in LTE is significantly simplified. In non-LTE (NLTE) conditions, S_ν departs from the Planck function and is dependent on the radiation intensity I_ν. By (1.1) I_ν also depends on S_ν, there is a cyclic dependence: the intensity depends on the source function and vice-versa, everywhere along the optical path. Modeling these NLTE effects becomes increasingly complex. Because of this complexity and because LTE is believed to be a very good approximation for a wide range of conditions in stellar atmospheres, the classical models assume LTE. It is usually when the temperature and density drop that departures from LTE start to have an influence in the photospheric structure. In the Sun, for example, it has been shown to be a good approximation for the photosphere.

The second approximation is related to the treatment of convection and geometry. Convection is difficult to model. It is the mixing of heat and mass that usually takes place at the outer layers of late-type stars. The classical models typically employ a treatment of convection based on the mixing-length theory. This is a local theory that describes convection as a 'blob' of hot material that travels up some distance in the atmosphere (the mixing-length, l) until it cools down and reaches thermal equilibrium with the surrounding material. This simplified view assumes the atmosphere to be horizontally homogeneous and time-independent. Thus classical models have a simplified one-dimensional (1D) stratification with no time dependence (hydrostatic equilibrium). The mixing-length l is for all effects a free parameter in the modeling. In addition, to explain the broadening of the spectral lines due to velocity fields not present in the models, they require the use of factors such as micro- and macro-turbulence, which are in effect 'fudge' factors to make up for deficiencies in the modeling.

Convection is driven by photon cooling at the surface, as the atmosphere becomes less opaque and photons can escape out of the star. It is inherently a non-local and time-dependent effect. Surface inhomogeneities called 'granules' develop on the surface, analogous to the bubbles in boiling water. Consistent modeling of convection requires the relaxation of the 1D geometry and time-independence. It is a dynamic, three-dimensional process. This mounts a challenging technical difficulty, as the model should simulate the hydrodynamics of the photosphere with the radiative heating and cooling, which is computationally very expensive. This technical barrier is the main reason why classical models employ a simplified treatment of convection.

Despite their limitations, the classical model atmospheres are still the most widely used models for chemical abundance studies in late-type stars. Because of their simplifying assumptions they are computationally much faster (both in terms of computing the thermal structure and the synthetic spectra). As such they can be computed for a wide range of stellar parameters, which is not yet possible with the newer generation models. Examples of widely used classical models are the MARCS[2] models (Gustafsson et al., 2008) and the ATLAS[3] models (Kurucz, 2005a).

In the Sun there is another class of models worth mentioning here, the semi-empirical models. They share the same limitations of classical models: 1D, time-independent and LTE assumed for spectral synthesis. These models are artificially constructed so that they reproduce a set of observational constraints derived from the Sun. Assuming the physics of line formation employed to be realistic and the observations reliable, these models provide an accurate insight into the mean 1D thermal structure of the Sun. But because no such detailed observations exist for stars other than the Sun, they cannot be constructed for other stars and their usefulness is limited. Yet, they can be used to test theoretical solar models. Examples of widely used semi-empirical solar models include the model of Holweger & Müller (1974, hereafter Holweger–Müller), the VAL III C model (Vernazza et al., 1981), FAL III C (Fontenla et al., 1993) and the MACKKL model (Maltby et al., 1986). Of these, the Holweger–Müller model is the only one that

---

[2] Available at http://marcs.astro.uu.se

[3] Available at http://kurucz.harvard.edu/grids.html

does not include the chromosphere. But because it is believed to describe the solar photospheric mean thermal structure very well, it has been historically used to derive the solar chemical composition (*e.g.* Anders & Grevesse, 1989; Grevesse & Sauval, 1998).

1.3. The new generation of stellar model atmospheres

The continuous increase in computational power over the last decades has made it feasible to attack the simplifying assumptions used in the classical model atmospheres. The most important of these are LTE and the 1D static treatment of convection.

A distinction should be made between NLTE model atmospheres and line formation. Several studies use classical 1D model atmospheres (computed assuming LTE), and then do a detailed NLTE study of the line formation, typically for one element. On the other hand, full NLTE atmospheric modeling is the consistent treatment of *all* atomic and molecular species in NLTE, taking into account the effects of radiative heating/cooling without assuming LTE. The line formation approach is a valid approximation insofar as the element being studied has a negligible effect on the overall opacities and electron pressure, and consequently on the atmospheric structure. Full NLTE modeling is complex because of the mutual dependence of the source function and radiation field, for all atomic and molecular species, everywhere in the photosphere. It poses challenges in computational power and also on atomic and molecular physics, because one has to know accurately all the data about radiative and collisional processes, for all the energy levels in all the elements and molecules. Obviously, many simplifications have to be done before the problem becomes tractable. First, tot all species are usually modelled in NLTE. Another typical NLTE modeling simplification is that of statistical equilibrium: the level populations are assumed not to vary with time.

The people behind the PHOENIX project[4] have pioneered the NLTE modeling of stellar atmospheres (see Hauschildt & Baron, 1999). Their code can perform multi-level full NLTE calculations for several elements, for more than 10^4 levels and 10^5 transitions. Because these calculations are themselves very computationally intensive (requiring supercomputers), the PHOENIX code still assumes a simplified geometry (1D) and treatment of convection (mixing-length). The PHOENIX NLTE models have been computed for the Sun (Short & Hauschildt, 2005) and for a significant range of cool-stars, in preparation for ESA's Gaia mission (Brott & Hauschildt, 2005; Sordo et al., 2009). Results from the solar NLTE models indicate that the NLTE effects on the atmospheric structure are small ($<$ 200 K in the outer layers), which confirms LTE as a good approximation for the solar photosphere.

As for advances in geometry and convection, it has been known for many years that the atmospheres of stars are not static nor horizontally homogeneous. In fact, spatial inhomogeneities are a fundamental characteristic of the atmospheres of late-type stars such as the Sun. This is very obvious when observing the Sun, as can be seen in Fig. 1.2. Over the last decades, significant effort has been put into modeling convection in stellar atmospheres realistically. Numerical experiments by D. Dravins, Å. Nordlund, B. Stein, M. Asplund and others have paved the way for the first 3D hydrodynamical simulations

---

[4] http://www.hs.uni-hamburg.de/EN/For/ThA/phoenix/index.html

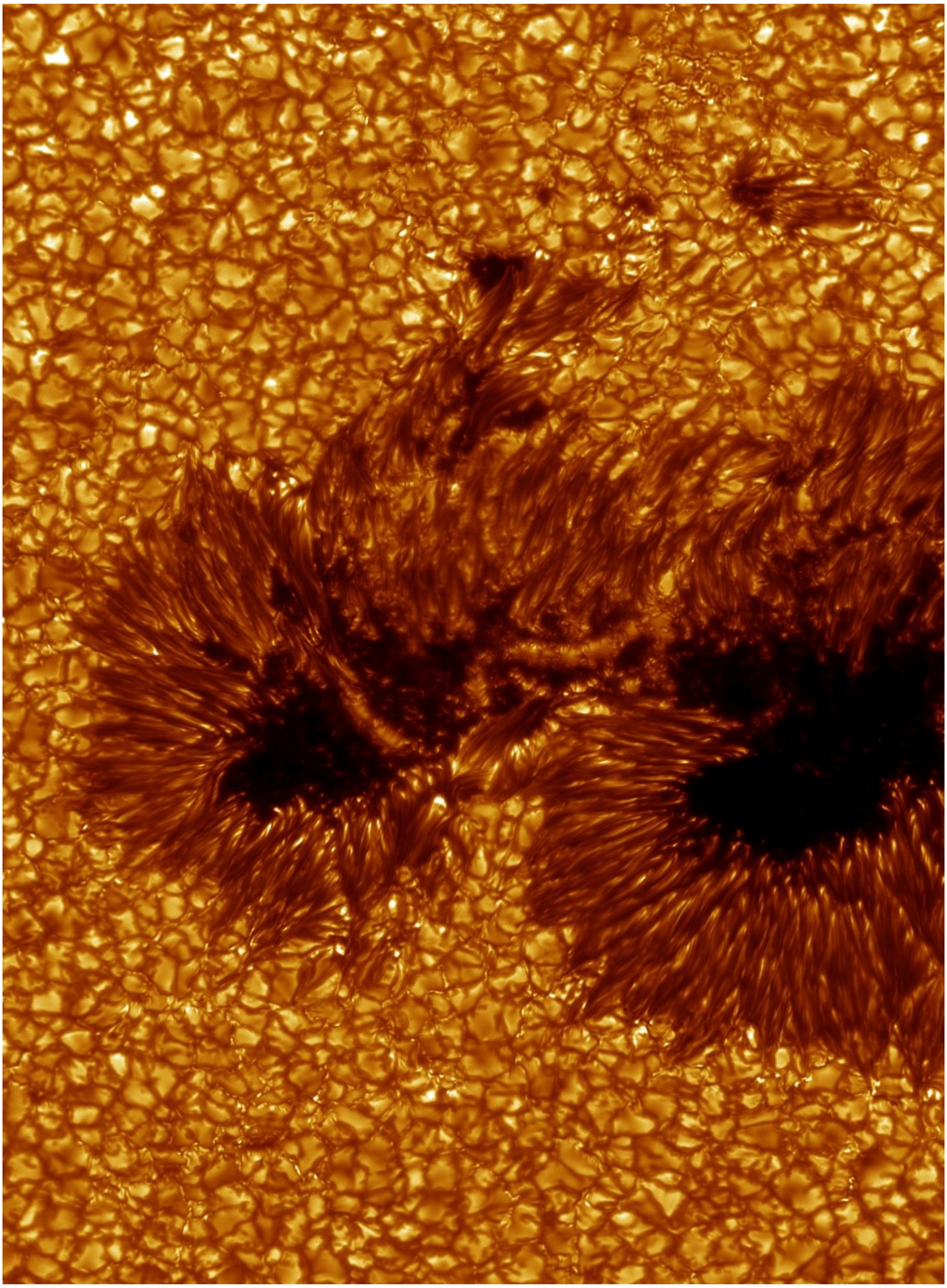

Figure 1.2 Image of the solar atmosphere in the spectral continuum around 436.4 nm. Obtained in 2003 with the Swedish 1-m Solar Telescope (SST) on the island of La Palma by Göran Scharmer, Kai Langhans and Mats Lofdahl, Royal Swedish Academy of Sciences. Structure is visible at many levels: the sunspots with their dark cores, filaments and bridges and the granulation pattern. The typical size of the granules is 1000 km. Their bright cores result from the hot upflowing material, and the dark intergranular lanes from the cool downdrafts. In some places bright regions can be seen between granules, an effect associated with the magnetic field.

of stellar photospheres. These simulations solve the standard equations for conservation of mass, momentum and energy, along with the 3D radiative transfer equation to include radiative heating and cooling. They model a small region of a photosphere (typically to cover ≈ 10 granules at any given time), believed to be representative of the whole photosphere. This is the so called 'box in star' approach. Overcoming the previous geometry limitations, these simulations treat convection self-consistently and without the need for adjustable parameters.

However, the advances in 3D model atmospheres come at a price, and that is a simplified treatment of the radiative transfer because of computational constraints. First, these models still rely on the assumption of LTE. Secondly, the simulations use a technique called 'opacity binning' (Nordlund, 1982). With opacity binning, the spectral line opacities are sorted by intensity into a few bins (typically 4, although more recent simulations use 12). The radiative heating integral is then computed for each of the opacity bins. This is opposed to what is done for classical 1D models, where the radiative transfer is solved via Opacity Distribution Functions (ODFs, see Gustafsson et al., 1975) or Opacity Sampling (OS, see Sneden et al., 1976), which can use up to tens of thousands of opacity points.

Because of the computational requirements, 3D stellar atmosphere models have not yet been constructed for as many types of stars as their 1D counterparts. Currently 3D models exist for main sequence and subgiant/giant stars of spectral types A–M, for a range of metallicities and gravities (*e.g.* Stein & Nordlund, 1998; Freytag et al., 2002; Allende Prieto et al., 2002; Collet et al., 2006; Trampedach, 2007; Kochukhov et al., 2007; Collet et al., 2008; Freytag & Höfner, 2008; Ludwig et al., 2009). Solar 3D model atmospheres provide an opportunity to test the realism of the 3D modeling in great detail, because the Sun can be extensively studied (such testing is indeed the subject of this thesis). Stein & Nordlund (1998) detail a solar 3D model and show that its granule statistics and dynamics are very accurate, in very good agreement with solar observations. Using the same model, Asplund et al. (2000a) performed a detailed comparison of theoretical Fe I line profiles against the observed solar spectrum. They found an excellent agreement in the line shapes, shifts and asymmetries without using any additional tunable parameters such as micro- and macro-turbulence, necessary for 1D models. This impressive agreement is a confirmation of how realistically the 3D models describe the convective motions in the atmosphere. The series of papers started by Asplund et al. (2000a) then goes to derive the solar abundances of several elements, using the 3D model. This resulted in the revised solar chemical composition of Asplund et al. (2005a). This revision, however, is not free from controversy (see next section).

Three-dimensional (LTE) models, along with 1D NLTE models represent a paradigm change in the way stellar atmospheres are modeled. They are the new generation, and even today they have just started to be adopted. They both require intensive calculations, often using supercomputers. Ideally, one would want 3D NLTE atmosphere models. While it is possible to build such codes today, the computational power required makes the exercise prohibitively expensive.

Figure 1.3 Effect of the different solar abundances in the squared sound speed differences $\delta c^2/c^2$ between solar interior models and observations (from helioseismic inversion). Data from Serenelli et al. (2009). *Legend:* GS98: Grevesse & Sauval (1998) abundances, AGS05: Asplund et al. (2005a) abundances, AGSS09 pht: Asplund et al. (2009) abundances. Uncertainties represented by dotted lines.

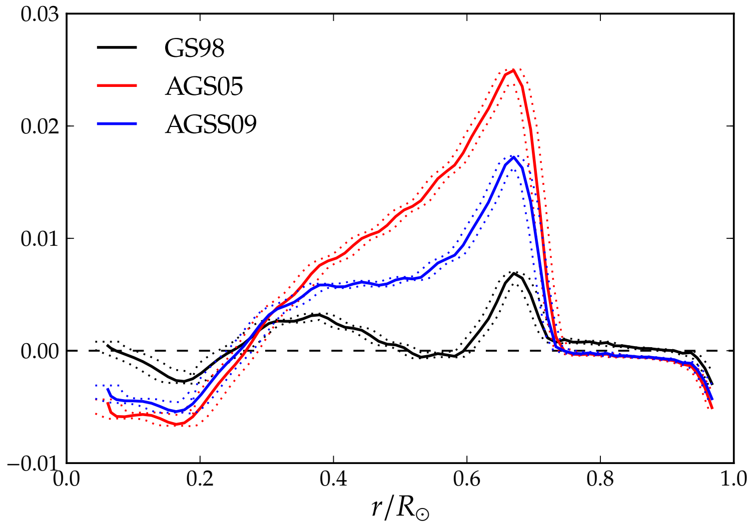

1.4. The solar interior modeling crisis

Using the 3D solar model of Stein & Nordlund (1998), M. Asplund and collaborators inferred the solar abundances of many elements, compiled in the revised solar chemical composition of Asplund et al. (2005a). Unlike previous determinations of the solar chemical composition, which used classical 1D models, this new revision was the first to employ detailed 3D line formation calculations, accounting for the surface inhomogeneities and temperature gradients of the solar photosphere consistently. Many atomic and molecular lines were used. NLTE corrections were applied where available and for some elements like oxygen and lithium full 3D NLTE line formation was used. Besides reproducing the line shapes and shifts very well, another success of the 3D analysis is a greater consistency between different abundance indicators. For example, the abundances derived from neutral and ionized species are very close and there are no significant trends in the derived abundance with the excitation potential of the lines (*e.g.* iron, Asplund et al., 2000b). Another example is the good agreement between the abundances derived from atomic and molecular lines, which in many cases was not possible with the 1D models (*e.g.* oxygen, Asplund et al., 2004). In terms of the solar metallicity, the new revision implies a lower heavy element content $Z = 0.0122$. Compared with the previous revision of Grevesse & Sauval (1998), which had $Z = 0.0169$, it represents a 26% decrease in the solar metallicity. This decrease has positive and negative consequences.

A positive consequence of the new metallicity is that the Sun now appears normal compared to its surroundings. There is a much better agreement between the photospheric and meteoritic abundances (for the non-volatile elements, which are not depleted in meteorites, see Asplund et al., 2005a). And the new C and O abundances agree better with those measured in the local interstellar medium (André et al., 2003). This solved a long-standing problem. With the previous solar metallicity the Sun appeared to be metal-rich when compared to its surroundings.

A negative consequence of the new metallicity is that it destroys the previously excellent agreement between solar interior models and helioseismology. These models simulate

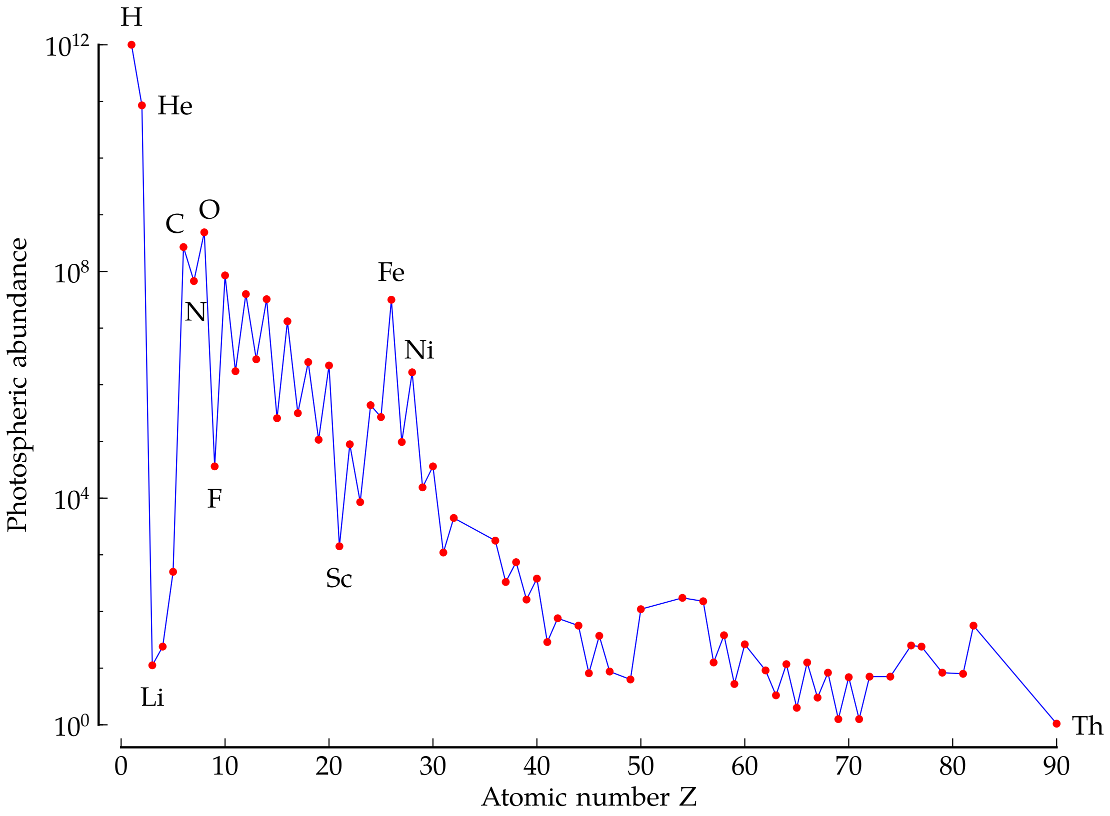

Figure 1.4 The solar chemical composition from hydrogen to thorium, latest revision from Asplund et al. (2009). Abundances derived from the photosphere using a 3D model and spectral synthesis. Exceptions made for the rare gases He, Ne, Ar, Kr and Xe, whose abundances were estimated indirectly. Element abundances plotted the customary logarithmic scale: $A(X) = \log_{10}(N_X/N_H) + 12$, where N_X is the number density of a given element, and N_H the number density of hydrogen.

the evolution of the Sun and predict its interior structure today. With the previous solar metallicity of Grevesse & Sauval (1998) these models predict a solar interior structure that is in very good agreement with the helioseismic inversion results. However, with the lower solar abundances the agreement is much worse (Bahcall et al., 2005). The reason for the change is that the lower metallicity implies a lower opacity. This affects the structure of interior models at many levels, from the depth of the convection zone to nuclear energy generation (Basu & Antia, 2008). Particularly relevant are the downward revisions of species such as C, N and O, as they are important opacity contributors. In Fig. 1.3 the effect of the new abundances on the solar interior models is shown. A significant effort has been undertaken to try and reconcile the solar interior models with the new solar abundances (see review of Basu & Antia, 2008), but at the moment there is no solution to this problem. Hence, there is some skepticism to the revised abundances from the solar interior modeling community, who perceive the problem as being with the abundances from the 3D modeling.

Recently there has been another revision of the solar chemical composition, by Asplund et al. (2009). They use an improved 3D model atmosphere (Asplund et al., in preparation; Trampedach et al., in preparation) and the inferred metallicity is slightly higher than the previous revision: $Z = 0.0135$. In Fig. 1.4 the individual abundances are shown

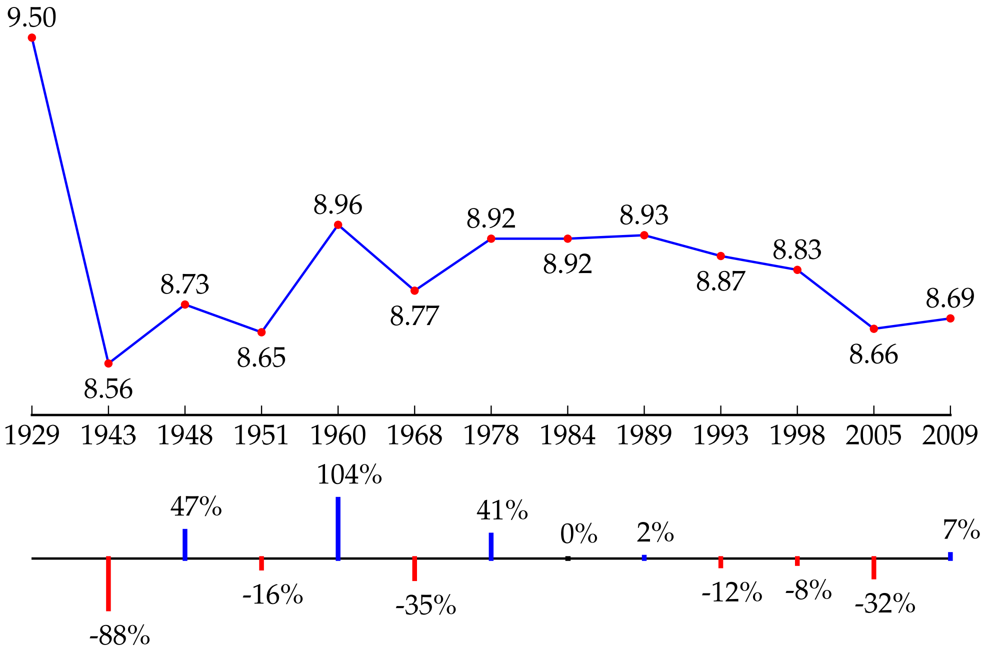

Figure 1.5 The solar oxygen abundance over the last 80 years, derived from photospheric lines. *Top:* the values for the solar oxygen abundance in the logarithmic scale by its ratio to hydrogen, defined to be at 10^{12}. References for the measurements are, chronologically: Russell (1929); Goldberg & Aller (1943); Unsöld (1948); Claas (1951); Goldberg et al. (1960); Lambert (1968, 1978); Grevesse et al. (1984); Anders & Grevesse (1989); Grevesse & Noels (1993); Grevesse & Sauval (1998); Asplund et al. (2005a, 2009).

as a function of the atomic number. This revision goes some way in minimizing the solar interior model problem (as seen in Fig. 1.3), but still leaves the question open. Of relevance in the 3D abundance analyses is the oxygen abundance. Oxygen is the most abundant element in the Sun after helium and its abundance determination is very important for the C and N abundances, since they are commonly derived from their ratios to oxygen. The 2005 revision of the solar oxygen abundance corresponded to a 32% decrease since the previous revision, in 1998. This can be seen in Fig. 1.5, where an historical view of the solar oxygen abundances is shown.

The solar interior modeling crisis raises the issue of the 3D modeling not being suitable for abundance analysis, and in particular for oxygen. It has prompted additional testing of the 3D models, before one can fully trust its abundance estimates.

1.5. More testing is needed for the new models

The Sun offers an ideal test-bench for model atmospheres. Our ability to resolve its surface means highly-detailed data can be obtained. While the solar 1D LTE models have been tested against many diagnostics, this is not the case for the new generation of models (3D LTE and 1D NLTE). The goal of this thesis is to fill in this gap and systematically test the new models against several solar observational tests. In particular for the 3D models. These tests will allow us to infer the models' suitability to derive chemical abundances in the Sun and in other stars.

Several observational tests will be detailed in the next chapters. They test many aspects of the models and line formation, in particular the temperature structure. Because oxygen is pivotal in the downward revision of the solar abundances, revisiting its line formation is one of the priorities. Some tests will use currently available solar data, while for others new data was acquired.

An important concept that will be used throughout this work is that of limb darkening or centre-to-limb variation (CLV). The CLV tests study the variations that occur in the solar disk. They are very powerful as they allow one to study different layers in the photosphere. Light from the centre of the solar disk comes from the deepest photospheric layers. As one goes further away from the disk-centre towards the solar limb, light comes from increasingly higher layers, because only light that is emitted from those higher layers can travel on a straight line towards the observer. This can be seen in terms of the Eddington–Barbier approximation, relating the surface intensity $I_\nu(\tau_\nu = 0)$ with the source function S_ν at a given optical depth τ_ν:

$$I_\nu(\tau_\nu = 0, \mu) \approx S_\nu(\tau_\nu = \mu), \tag{1.2}$$

where $\mu \equiv \cos\theta$, being θ the angle between the line of sight and the direction of the solar disk-centre. At the limit of $\mu = 0$, light comes from the highest point in the photosphere. If one assumes LTE (a good approximation for the continuum-forming layers of the solar photosphere), $S_\nu = B_\nu(T)$ and it becomes apparent that the surface intensity at different values of μ is a good temperature indicator. Indeed, semi-empirical models of the Sun use the continuum CLV to calibrate the temperature structure. In this thesis the CLV of the continuum and of lines will be one of the main testing tools for the new models.

1.6. Thesis outline

The main content of this thesis is organized into the next three chapters. Chapters 3 and 4 have been accepted for publication in the international journal A&A. Chapter 2 has been submitted to the same journal. Because of the journal format, they all have an abstract, introduction, main body and conclusions. Inevitably there will be some repeated material across the introductions. To avoid unnecessary repetition the references are all collected at the end of this thesis, and not on a chapter basis.

In Chapter 2 we test the realism of the model atmospheres primarily by confronting their temperature structure with that of the Sun. These test comprise the centre-to-limb variation of the continuum intensity, the absolute continuum flux distributions, and the continuum intensity distribution and contrast of the disk-centre granulation. The continuum centre-to-limb variation tests the temperature gradient across many depths of the photosphere. The absolute continuum fluxes, on the other hand, test the absolute temperature at the deepest photospheric layers. The continuum intensity distribution tests how realistic the description of the surface inhomogeneities is in the 3D model. Except for the continuum intensity distribution (where only the 3D model can be tested), in this chapter we have tested the 3D model, the 1D semi-empirical Holweger–Müller model, the 1D LTE MARCS model and the 1D PHOENIX NLTE and LTE models.

Chapter 3 details line formation testing at high spatial resolution. High spatial and spectral resolution observations were obtained with the Swedish 1-m Solar Telescope

(SST) and are detailed here. The aim of this observations was the spatially-resolved study of line formation, at different viewing angles. The priority of this work are the atomic oxygen lines, although several lines of other elements are also tested. The 3D model and line formation (both in LTE and NLTE) are then tested against these observations.

Making use of the our solar observations detailed in Chapter 3, we proceed to test the centre-to-limb variation of the oxygen and other lines in Chapter 4. The focus of this chapter is on the properties of the temporal and spatial mean spectra. Line formation calculations for atomic oxygen lines used to derive the oxygen abundance are carried out in great detail: accounting for departures from LTE, an accurate wavelength calibration and careful inclusion of blends. The models tested against the observations are the 3D model, and the 1D Holweger–Müller and MARCS models.

The findings of this thesis are summarized in Chapter 5. A look into the consequences of this work and future avenues of study is also presented.

Finally, Appendix A contains a repetition of most of the analysis for an older version of the 3D model. Appendix B contains extra material regarding the line quantities at high spatial resolution.

CHAPTER 2

How realistic are solar model atmospheres?

T. M. D. Pereira, M. Asplund, R. Trampedach, R. Collet, *submitted to A&A*

Abstract

Context: In the last decade the new generation of solar model atmospheres, such as the 3D time-dependent models, have been used to derive the solar abundances.

Aims: Our goal is to test various solar atmosphere models against key observational constraints, specifically to test the new 3D model of Asplund and collaborators, 1D NLTE and LTE models from the PHOENIX project, the widely used 1D MARCS model and the 1D semi-empirical model of Holweger–Müller.

Methods: We confront the models with three classical tests of the temperature profile: continuum centre-to-limb variations and absolute continuum fluxes. In addition, we also test the 3D model for the continuum intensity distribution on the solar granulation.

Results: We find an excellent agreement of the 3D model with the centre-to-limb observations. This model performs even better than the Holweger–Müller model, that was constructed largely to fulfill such observations. The agreement for the 1D theoretical models is less satisfactory. In the absolute continuum fluxes, predictions for most models agree well with the observations. Exception is made for the Holweger–Müller, which seems to show an excess of flux in the visible and infrared. For the continuum intensity fluctuations over the disk-centre granulation we find that the 3D model reproduces the observed intensity distribution and ΔI_{rms} well.

Conclusions: The agreement of the 3D model with the observables is very good. This further reinforces the view that its temperature structure is realistic. On the other hand, some weaknesses in the 1D LTE models (theoretical and semi-empirical) are exposed. The differences between the PHOENIX LTE and NLTE models are small.

2.1. Introduction

Solar model atmospheres are a cornerstone in stellar astronomy. The Sun is a natural reference when studying other stars, and realistic solar photosphere models are essential to infer solar parameters such as its chemical composition. The wealth of solar data available can be used to rigorously test and constrain photosphere models. This testing provides an invaluable insight about the model physics and its degree of realism, providing a fundamental calibration for building models of other stars.

With the significant increases in computational power of recent years, the classical approximations used when modeling stellar atmospheres have started to be challenged. Of these approximations, the most significant are the assumption of a static 1D atmosphere with a mixing length type treatment of convection, and the assumption of local thermodynamical equilibrium (LTE). Although at present no model of stellar atmosphere is able to relax these two assumptions simultaneously, efforts have been made to tackle each of these approximations individually. On the geometry/convection side, realistic 3D hydrodynamic time-dependent simulations of convection have been developed and used as models of the solar photosphere (*e.g.* Stein & Nordlund, 1998; Asplund et al., 2000a; Freytag et al., 2002; Vögler et al., 2004; Carlsson et al., 2004; Caffau et al., 2008b). On the radiative transfer side, the PHOENIX project has pioneered the non-LTE (NLTE) modeling of 1D solar models (Hauschildt & Baron, 1999; Short & Hauschildt, 2005).

The application of 3D solar models to abundance analysis (*e.g.* Asplund et al., 2004) has resulted on a revised solar metallicity of $Z = 0.0135$ (Asplund et al., 2009), substantially smaller than previous canonical values (*e.g.* $Z = 0.0201$ in Anders & Grevesse 1989 and $Z = 0.0169$ in Grevesse & Sauval 1998). The realistic treatment of convection and velocity fields in the 3D models resulted in an excellent agreement between predicted and observed line shapes and bisectors, not possible with the 1D models even with the free parameters of micro- and macro-turbulence (Asplund et al., 2000a). This agreement is a strong indicator of how realistic the model is. Additionally, when compared with observations of the solar granulation at high spatial resolution, the 3D models correctly predict the characteristic size and lifetimes of the granules (Stein & Nordlund, 1998). However, the results are still controversial because by using a lower solar metallicity the previous excellent agreement between solar interior models and helioseismology deteriorates significantly (*e.g.* Bahcall et al., 2005; Basu & Antia, 2008).

A criticism of the 3D solar models sometimes raised is that while they have been tested against many spectral lines, they lack a thorough testing of temperature structure, such as the continuum centre-to-limb variation and absolute continuum fluxes (Basu & Antia, 2008). A correct temperature structure is of the utmost importance to abundance studies. Using a 1D horizontal and temporal average of the 3D model of Asplund et al. (2000a), Ayres et al. (2006) suggest that the 3D model fails to describe the observed centre-to-limb variation and its temperature gradient is too steep. The first claim is partly dismissed by Koesterke et al. (2008), showing that the 1D average is not a valid approximation of the full 3D model for temperature profiling and that the performance of the 3D model in the continuum centre-to-limb variation is comparable to that of theoretical 1D models – a view corroborated by Pereira et al. (2008) and Trujillo Bueno & Shchukina (2009). However, Koesterke et al. (2008) agree with Ayres et al. (2006) in that the temperature gradient of the 3D model is slightly too steep in the continuum forming layers.

The aim of this work is to systematically test the temperature structure of several models of the solar photosphere, including a 3D model and a 1D NLTE model. We use the new 3D model of Trampedach et al. (2009, in preparation), an improved version of the Stein & Nordlund class of models, and recent 1D NLTE and LTE models from the PHOENIX project (Hauschildt & Baron, 1999). We also employ the widely used 1D MARCS model (Gustafsson et al., 2008) and the semi-empirical 1D model of Holweger & Müller (1974).

The models used are described in more detail in §2.2. To compare their temperature structure with the observations we use three classical tests: the continuum centre-to-limb variation in §2.3 and the absolute continuum flux distribution in §2.4. In addition, we also test the 3D model against observations of the continuum intensity distribution and $\Delta I_{\rm rms}$ in §2.5. Our conclusions are given in §2.6.

2.2. Model atmospheres

2.2.1. 3D Model

We use the new 3D model solar atmosphere by Trampedach et al. (2009, in preparation), that is the same model Asplund et al. (2009) adopted for the derivation of photospheric solar abundances. The solar surface convection simulation was performed using the 3D, radiative, hydrodynamical, conservative, STAGGER-CODE (Nordlund & Galsgaard, 1995). In the simulation, the equations for the conservation of mass, momentum, and energy are solved together with the radiative transfer equation for a representative volume of solar surface (6.0×6.0×3.8 Mm^3) on a Cartesian mesh with 240^3 numerical resolution. The horizontal grid is equidistant, while the vertical depth scale has a non-constant spacing optimized to better resolve the layers at the photospheric transition where temperature gradients are at their steepest. Open, transmitting, boundaries are assumed at the top and bottom of the simulation domain, and periodic boundary conditions are enforced horizontally. It is important for the lower boundary to be transmitting, to avoid homogenizing the otherwise highly asymmetric (between up and down) convective flows.

The simulation domain completely covers the Rosseland optical depth range $-5 \leq \log \tau_{\rm Ross} \leq 7$ (that is, the largest optical depth of the top layer is less than -5 and the smallest optical depth of the bottom layer is greater than 7). The radiative transfer equation is solved using a long characteristics Feautrier-like scheme down to $\tau_{\rm Ross} \approx 300$, and the diffusion approximation is employed in the deeper layers. The main improvement over the simulation of Asplund et al. (2000a) is the treatment of opacities and line-blocking in particular. In both the old and new simulations, continuous and line opacities are included via a statistical method, called *opacity binning* or *multi-group method* (Nordlund, 1982): wavelengths are sorted into *opacity bins* according to the strength of the opacity and the corresponding LTE source functions are added together within each bin. In the original binning scheme, Nordlund (1982) used the Rosseland average κ_0 of the opacities in the continuum bin, scaled by a constant factor for each of the other bins, $\kappa_{\rm j} = \kappa_0 10^{j\Delta x}$, in practice assuming $\Delta x = 1$ and $j = 0, \ldots, 3$. The transition to free streaming for optical depths in the continuum bin $\tau_0 \ll 1$ is ensured by an exponential bridging (in τ_0) to an intensity-weighted mean opacity. The multi-group method was further developed by Skartlien (2000), who relaxed the approximation of κ_j just being a scaled κ_0, and instead computed the actual Rosseland average for each bin. This also ensures that the Rosseland mean of the bin-wise opacities converges to the actual Rosseland mean of the monochromatic opacities. Trampedach et al. (2009, in preparation) have further improved the method by sorting opacities into bins not only according to opacity strength but also according to wavelength, and allowing arbitrary bin sizes; a similar binning criterion has been implemented by Caffau et al. (2008a) in the CO^{5}BOLD code. For the present simulation, continuous opacities are taken from Gustafsson et al. (1975, and subsequent updates) and line opacities from the latest MARCS stellar atmosphere package (Gustafsson et al., 2008). The solar chemical composition by Asplund et al. (2005a) and the equation-of-state by Mihalas et al. (1988, and subsequent updates) are adopted.

The positions of the bin borders are then optimized with respect to a monochromatic radiative transfer calculation for the simulation's average temperature and density stratification taken on surfaces of constant Rosseland optical depth. The generalization of the bins and the optimization reduce the differences between the radiative heating of the monochromatic and the binned solution by a factor of five, to within less than 1%. The effect of radiative heating and cooling on the simulation is therefore faithfully reproduced by this opacity-binning. Trampedach et al. (2009, in preparation) also performed a 3D monochromatic radiative transfer calculation on the full 3D simulation cube for a single snapshot, and found a < 5 K (0.08%) difference in $T_{\rm eff}$ between the monochromatic and the binned solution. Before being subjected to scientific tests, the simulation has been fully relaxed, and has subsequently run for the 45 solar minutes used here (90 snapshots). The relaxation process included extracting energy from radial p-modes, and ensuring that the total flux is statistically constant with depth, that no drifts are present in the thermodynamical quantities at the bottom boundary, and that the vertical grid resolves the radiative transfer in the photosphere.

Finally, a similar surface convection simulation has also been carried out starting from the same initial snapshot and relying on the same input physics, opacity binning, and radiative transfer scheme but using a different 3D hydrodynamical code (Stein & Nordlund, 1998) and a lower numerical resolution (150×150×82). The results from the two time-sequences are comparable and their statistical properties are essentially equivalent.

For the calculations presented here the original simulation was interpolated to a coarser 50×50×82 resolution (with a finer vertical depth scale) to save computing time. The effective temperature of the 90 snapshots used is $T_{\rm eff} = 5778 \pm 14\,$K.

2.2.2. 1D Models

We use two types of 1D models: theoretical and semi-empirical. The semi-empirical 1D model of Holweger & Müller (1974) was built from a range of observables to reproduce the mean physical quantities of the solar photosphere. Most importantly, it was constructed to follow the observed continuum centre-to-limb variation between 0.5–300 μm and the line depths of ≈900 spectral lines. This is an important detail to note when considering our centre-to-limb variation comparison, although the observations we employ are more recent than the ones available when the Holweger–Müller model was built. Historically, the Holweger–Müller model has been the atmosphere of choice when deriving solar abundances.

Of the 1D theoretical models we include the LTE, line-blanketed solar MARCS model, which is a reference for the MARCS grid of model atmospheres (Gustafsson et al., 2008). We also include an LTE and a NLTE model from the PHOENIX project (Hauschildt & Baron, 1999). These two models have been computed for the solar abundances of Asplund et al. (2005a) and the same input physics (as per the PHOENIX GAIA grid, Brott & Hauschildt, 2005). They differ only in their treatment of atomic level populations. The NLTE model has been computed with a NLTE treatment of H, He, C, N, O, Mg and Fe.

To ensure consistency when using our line formation code, opacities and equation of state, for the 1D models we took the $T(\tau)$ relation from their respective references and integrated $P_{\rm gas}$ in optical depth assuming hydrostatic equilibrium to obtain the pressures and densities that yield the same $T(\tau)$ when using our opacities and equation of state. We note that this is a often overlooked source of error when comparing results for supposedly the same model atmosphere since this pressure-integration is not always carried out. In fact the Holweger & Müller (1974) model is essentially only an updated version of the Holweger (1967) model with a new pressure-integration due to revised abundances.

In Fig. 2.1 the mean temperature structure of the 3D model is plotted against the 3D model of Asplund et al. (2000a), the 1D Holweger–Müller and MARCS models (left) and against the PHOENIX LTE and NLTE models (right). The effect of NLTE in the PHOENIX models seems to be a cooling of the outer layers, with minor differences at other depths. This NLTE cooling goes in the opposite direction of the NLTE effects of other PHOENIX solar NLTE models (Short & Hauschildt, 2005, 2009), where the NLTE effects cause a warming in the outer layers. This discrepancy seems to be associated with a different choice of atomic species treated in NLTE.

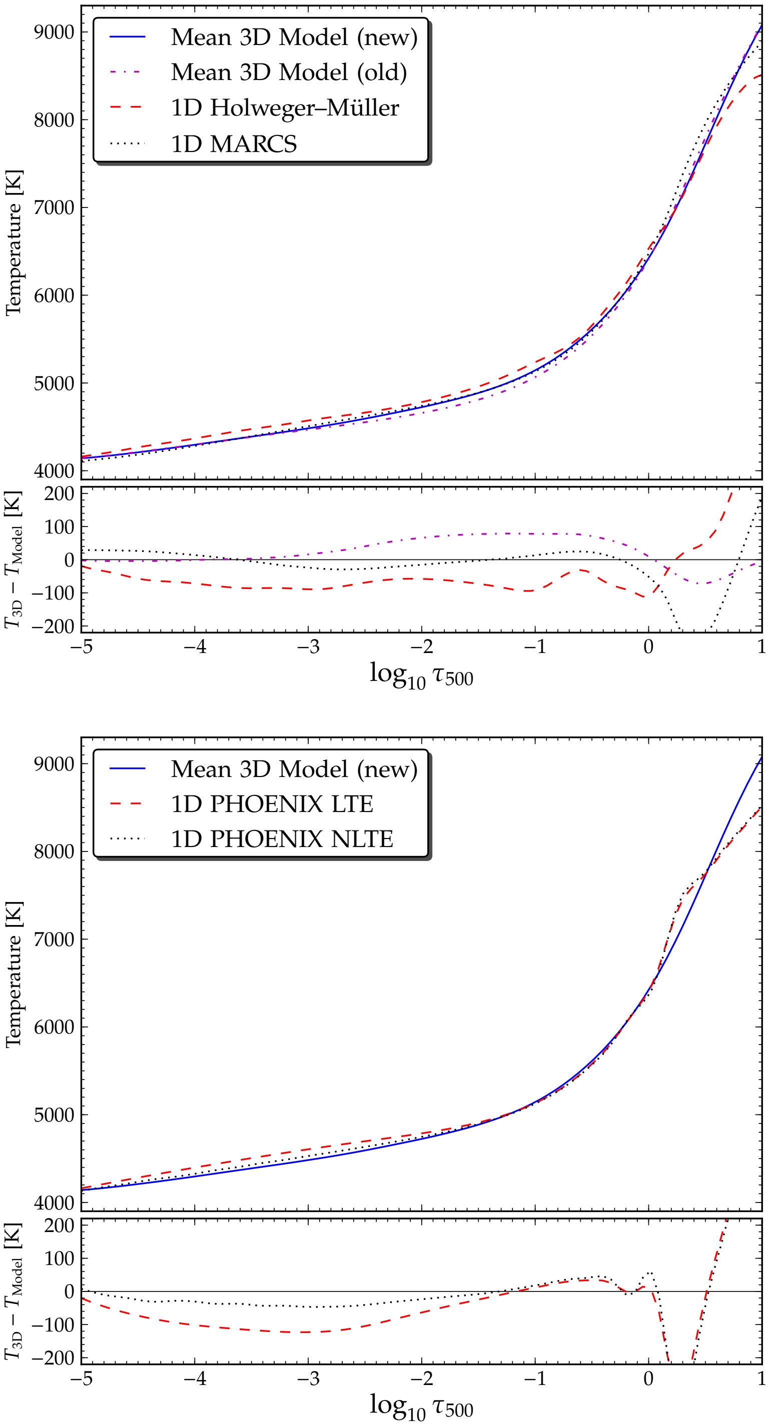

Figure 2.1 Temperature structure of the 3D and 1D models, plotted against the optical depth at 500 nm. For the 3D models structure represents the temporal and spatial mean (over τ_{500} iso-surfaces). On the top we compare the new 3D model used in this work with the 'old' 3D model of Asplund et al. (2000a). *Smaller panels:* differences between the new 3D model and a given model (legend according to the adjacent large panels).

2.3. Continuum centre-to-limb variations

2.3.1. Context

The centre-to-limb variations (CLV) of continuum intensities provide a good probe of the solar photosphere. Because the continuum intensity is proportional to the local source function of continuum forming regions, its CLV is a measure of the temperature variation with depth (the closer to the solar limb, the higher up in the atmosphere). The variation of depth can be expressed in terms of $\mu \equiv \cos\theta$, where θ is the heliocentric viewing angle. Normalizing $I(\mu)$ by the disk-centre value $I(\mu = 1)$, one has a measure of the temperature gradient of the photosphere. This provides a robust test of models.

2.3.2. Observations

We make use of the CLV observations of Neckel & Labs (1994) and Pierce et al. (1977). They cover respectively the wavelengths between 303–1099 nm and 740.4–2401.8 nm, as shown in Fig. 2.2 for $0.1 \leq \mu \leq 0.9$. We compare the models with Neckel & Labs (1994) for $\lambda \leq 1099$ nm and Pierce et al. (1977) for $\lambda > 1099$ nm. Although not used in our comparison, the observations of Pierce & Slaughter (1977), covering the range 303.3–729.7 nm, are also plotted in Fig. 2.2 and agree very well with Neckel & Labs (1994).

Other CLV observations of longer wavelengths exist, such as Spickler et al. (1996). However, as is visible in Fig. 3 of Spickler et al. (1996), there is a considerable scatter between different observations, especially for $\lambda \gtrsim 4$ μm. Because of these uncertainties we do not include them in this comparison.

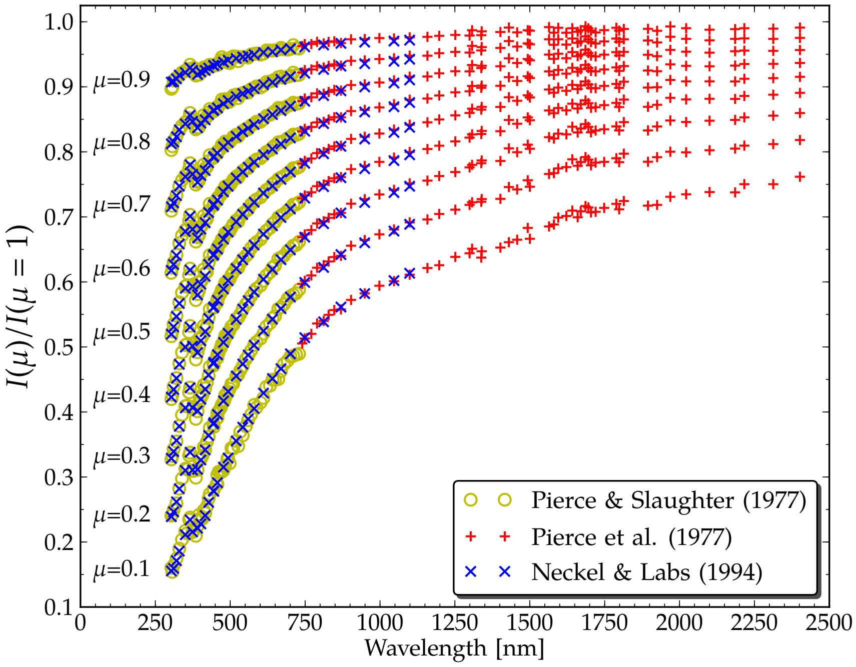

Figure 2.2 Continuum centre-to-limb observations in the visible and near-infrared, from Pierce & Slaughter (1977), Pierce et al. (1977) and Neckel & Labs (1994). In the wavelength region where the sets overlap we use only Neckel & Labs (1994) for our comparisons.

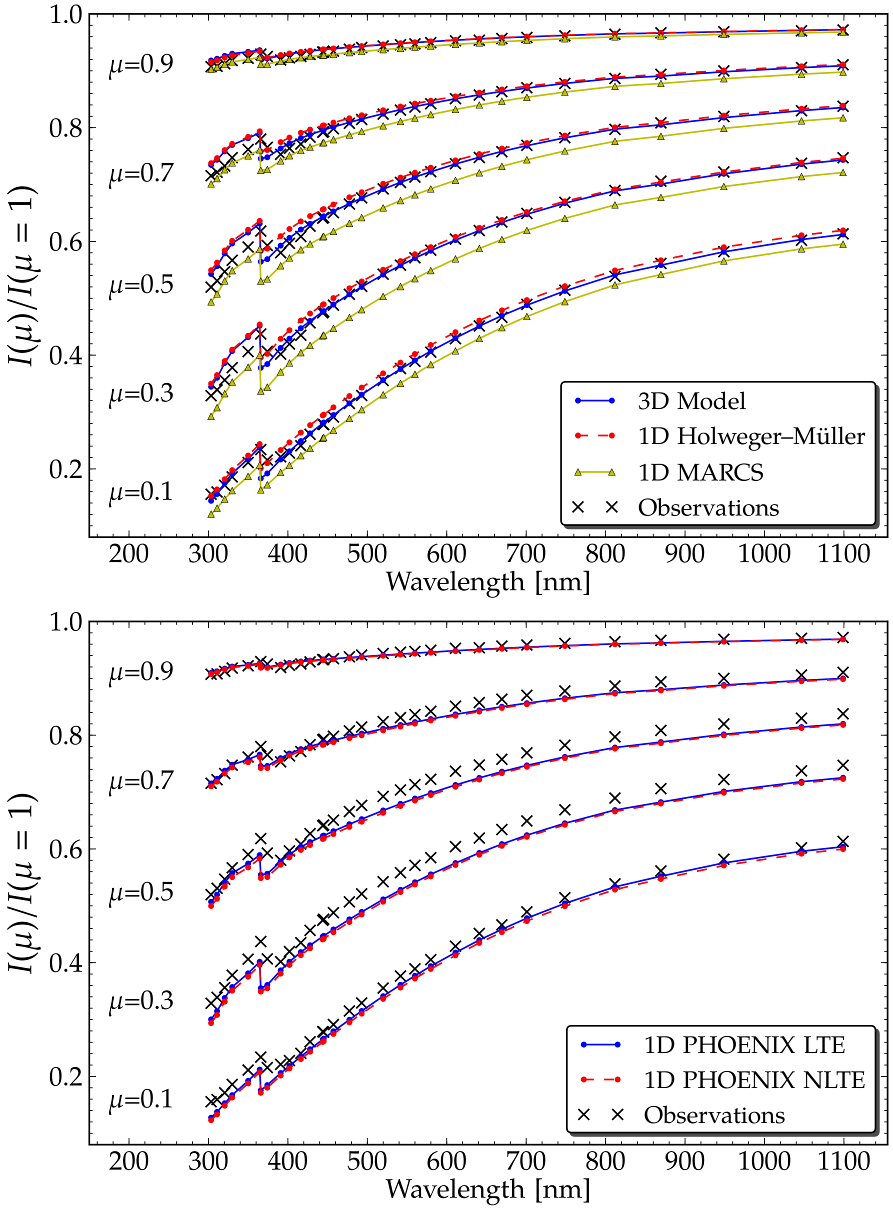

Figure 2.3 Centre-to-limb variations in the continuum intensity. Comparison with the visible/infrared observations of Neckel & Labs (1994).

2.3.3. Results and discussion

The model predictions were computed using our LTE line formation code, which was used to obtain the predicted intensity at different inclinations. The intensities were computed for nine different values of $\mu \equiv \cos\theta$ and for each inclination except the vertical they were averaged over four φ-angles in the 3D case. These intensities were interpolated in μ for the inclinations shown. For the 3D model the intensities were computed for each of the 90 snapshots, the final value being the temporal average.

Results for the visible and near-infrared continuum centre-to-limb variation are shown in Figs. 2.3 and 2.4. A more compact comparison with Neckel & Labs (1994) is made

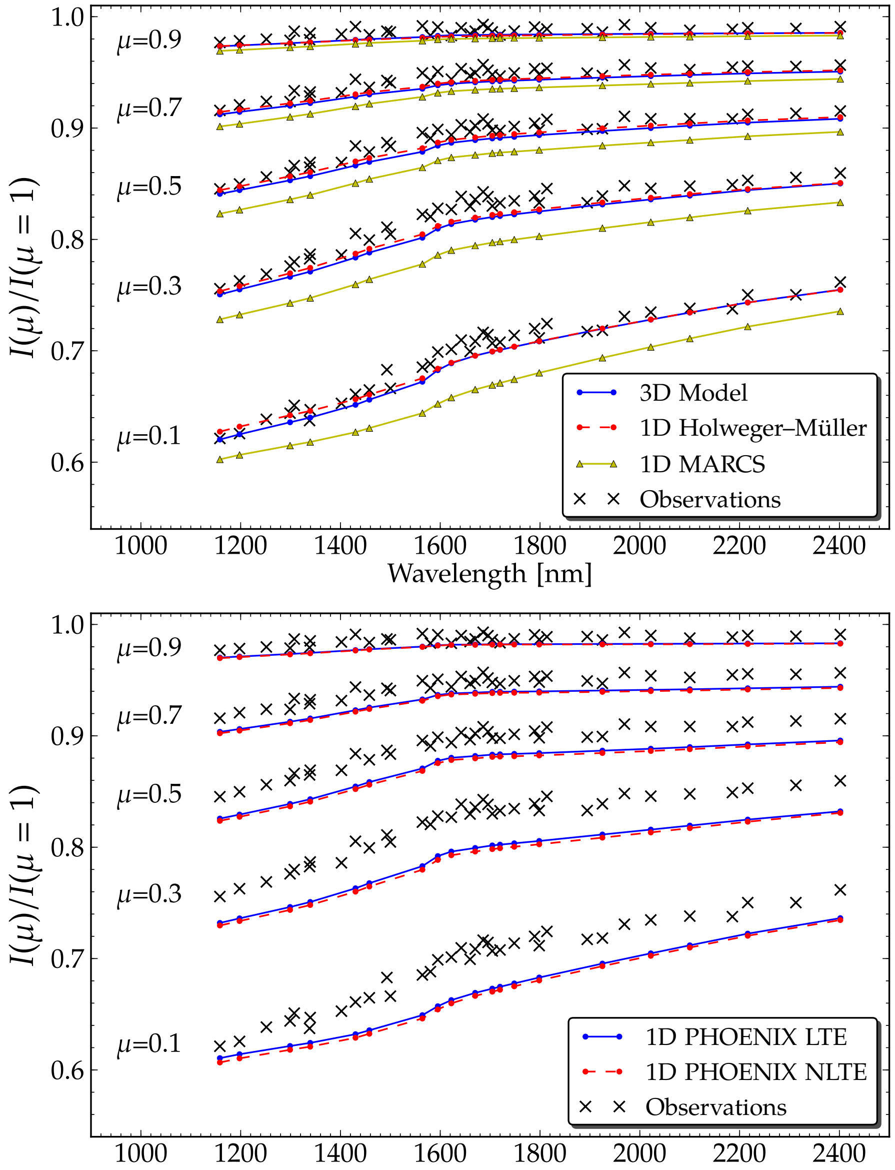

Figure 2.4 Centre-to-limb variations in the continuum intensity. Comparison with the near-infrared observations of Pierce et al. (1977), for wavelengths between 1158.35–2401.8 nm.

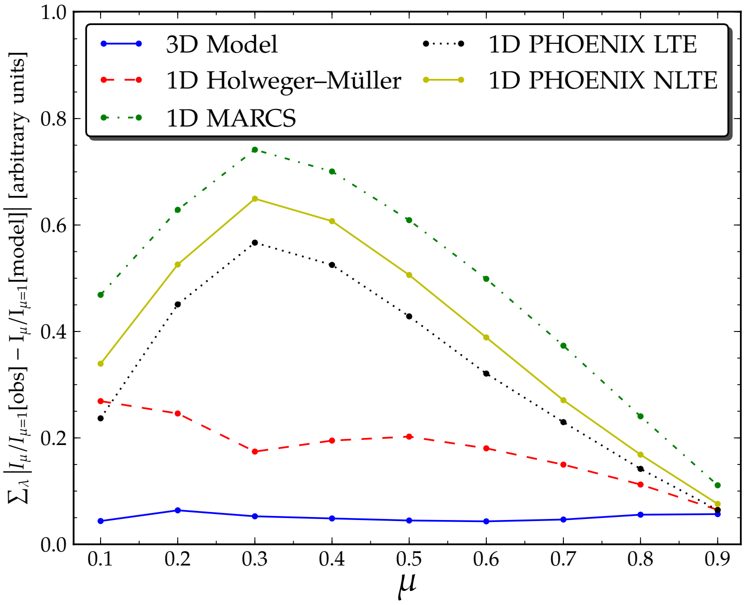

Figure 2.5 Difference between observations and models in the centre-to-limb variation, summed over wavelength as a function of μ (see text). Comparison with Neckel & Labs (1994) for $\lambda > 400$ nm.

in Fig. 2.5, where we plot the absolute value of the difference between models and observations, summed over wavelength for each μ value. Because of uncertainty in the observations (from the difficulty in finding continuum regions), this sum in wavelength is made for $\lambda > 400$ nm.

The results show an excellent agreement between the 3D model and the observations, particularly when comparing with Neckel & Labs (1994). This agreement is visibly better than that of the 1D Holweger–Müller model, which is quite remarkable given that it was empirically constructed to fit the centre-to-limb variations. It should be noted, however, that the observational and atomic data available today are better than when the Holweger–Müller model was constructed, which contribute for it not reproducing the observations perfectly. With the infrared observations the agreement with the models is slightly worse. However, observations at these wavelengths seem more uncertain, as can be seen by the increased scatter between data points. It is likely that this additional uncertainty affects the agreement with the models. Indicative of this is the region between 1500–1850 nm, where the observations show some scatter and are consistently higher than the model predictions.

The agreement with the theoretical 1D models is not as good. It is interesting to note in Fig. 2.5 that LTE models of MARCS and PHOENIX have the same trend with μ, although the PHOENIX performs slightly better. The results for the PHOENIX NLTE model depart only slightly from the LTE model results. The NLTE cooling of the outer layers seen in Fig. 2.1 causes a slightly steeper temperature gradient, which leads to a worse agreement with the observed centre-to-limb variations. But the overall structure and dependence with μ remains essentially the same for both PHOENIX models, as seen in Figs. 2.3 and 2.5, due to the similarity in $T(\tau)$ for $-2 < \log\tau < 0$ that is largely tested with continuum CLV.

2.4. Absolute flux distribution

2.4.1. Context

For our tests of the temperature stratification predicted by model solar atmospheres we are interested in the absolute continuum fluxes. They provide an absolute temperature scale for the deepest layers in the photosphere.

2.4.2. Observations

Several observations of the absolute solar flux/irradiance are available, either space-based (*e.g.* Colina et al., 1996; Thuillier et al., 2004) or Earth-based (*e.g.* Kurucz et al., 1984; Brault & Neckel, 1987; Kurucz, 2005b, obtained with the high-resolution NSO/Kitt Peak Fourier transform spectrometer). The space-based observations provide a spectrum clean of terrestrial absorption features, but at the cost of a lower spectral resolution.

Our approach to extract the observed continuum fluxes was to use an absolute flux atlas and divide it by a normalized flux atlas (for the points deemed to be near the continuum). We used the Kurucz (2005b) irradiances and normalized flux atlases, available for the interval of 300–1000 nm. They are a recent reduction of the data used to produce the atlas of Kurucz et al. (1984), and have been carefully adjusted to remove the telluric absorption features. The choice of using the Kurucz (2005b) atlases instead of space-based observations was made because of its consistency between absolute and normalized fluxes.

If a space-based irradiance atlas was used, the slight differerences in line strengths or wavelength mismatches between the irradiance and normalized flux atlases would cause some scatter in the continuum fluxes, which would have to be smoothed out (see Ayres et al., 2006, where such an approach is followed). To avoid these uncertainties we use the Kurucz (2005b) atlases that, being produced from the same data, have a consistent continuum determination and wavelength calibration between the irradiance and normalized flux atlases.

The observed continuum flux was obtained as follows. First the irradiance is converted to flux at the solar surface using the multiplicative factor of $[(1\ \mathrm{AU})/R_\odot]^2 \approx 46202.0$. Then the wavelengths of the continuum high points in the normalized flux are identified. These are defined where $F_\lambda > 0.99\ F_\lambda^{\mathrm{m}}$, where F_λ^{m} is a local maximum in 5 nm windows. Finally the absolute flux is divided by the normalized flux for the continuum high wavelengths. This ratio is linearly interpolated to a coarser resolution of 1 nm. A few spurious points were manually removed. The Kurucz (2005b) irradiance has been normalized to the total solar irradiance of Thuillier et al. (2004). Following the discussion in Ayres et al. (2006) we have readjusted the continuum fluxes by −0.4%, to account for the more accurate total solar irradiance of Kopp et al. (2005). In Fig. 2.6 we show the original observed fluxes along with our derived continuuum fluxes.

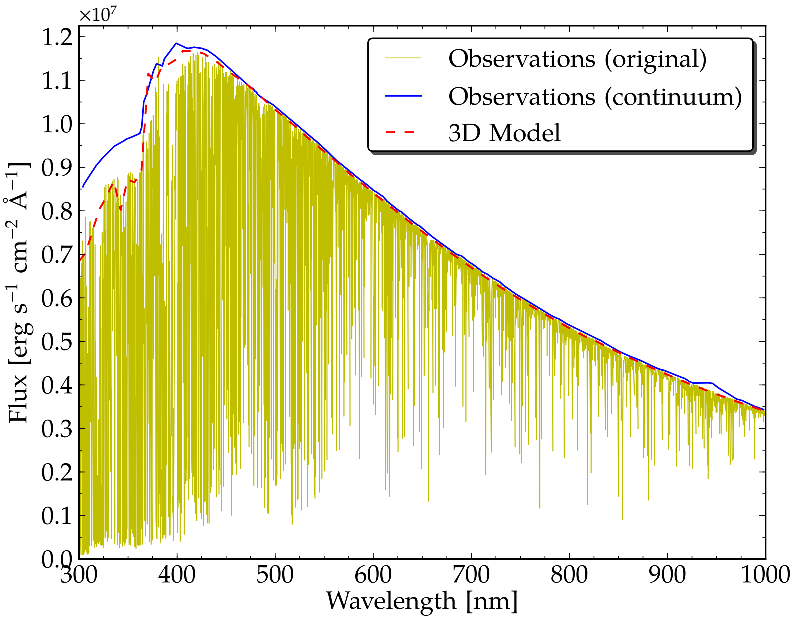

Figure 2.6 Comparison of the original fluxes of Kurucz (2005b), our derived continuum fluxes (see text), and the predicted continuum fluxes from the 3D model.

2.4.3. Results and discussion

The predicted continuum fluxes were computed with our LTE line formation code. The disk-integrated fluxes are computed using 8 μ-angles and 4 φ-angles, a total of 32 angles. The μ-angles and weights are taken from a Gaussian quadrature. For the 3D models the fluxes are computed and averaged for the 90 simulation snapshots.

The resulting fluxes for all models are shown in Fig. 2.7. A differential comparison is also shown in Fig. 2.8. There is an excess of flux for $\lambda \lesssim 370\,\mathrm{nm}$ in the observed continuum fluxes when compared with the original flux (with lines) or any of the models. This difference, also evident in Figs. 2.7 and 2.8, seems to be caused by a too high continuum placement in the normalized Kurucz (2005b) flux atlas (*e.g.*, higher than in Kurucz et al., 1984; Brault & Neckel, 1987). Being a region very crowded with lines, the discrepancy between observations and models arises from the difficulty in finding the continuum level (which is systematically overestimated), and not from a failure of the models.

Overall the 1D MARCS model seems to reproduce the observations best, although the differences between different models are small. The Holweger–Müller predictions are consistent with a correct T_{eff}, but its flux distribution has a different shape. Between 350–450 nm it has less flux, but beyond $\lambda \approx 500\,\mathrm{nm}$ it shows an excess flux when compared with the observations. The 3D model consistently predicts slightly less flux than the observations, but nevertheless has a good agreement and reproduces the flux distribution well. The PHOENIX LTE model behaves similarly to the 3D model, but with less flux at the peak of the distribution. The differences between the NLTE and LTE PHOENIX models are very small.

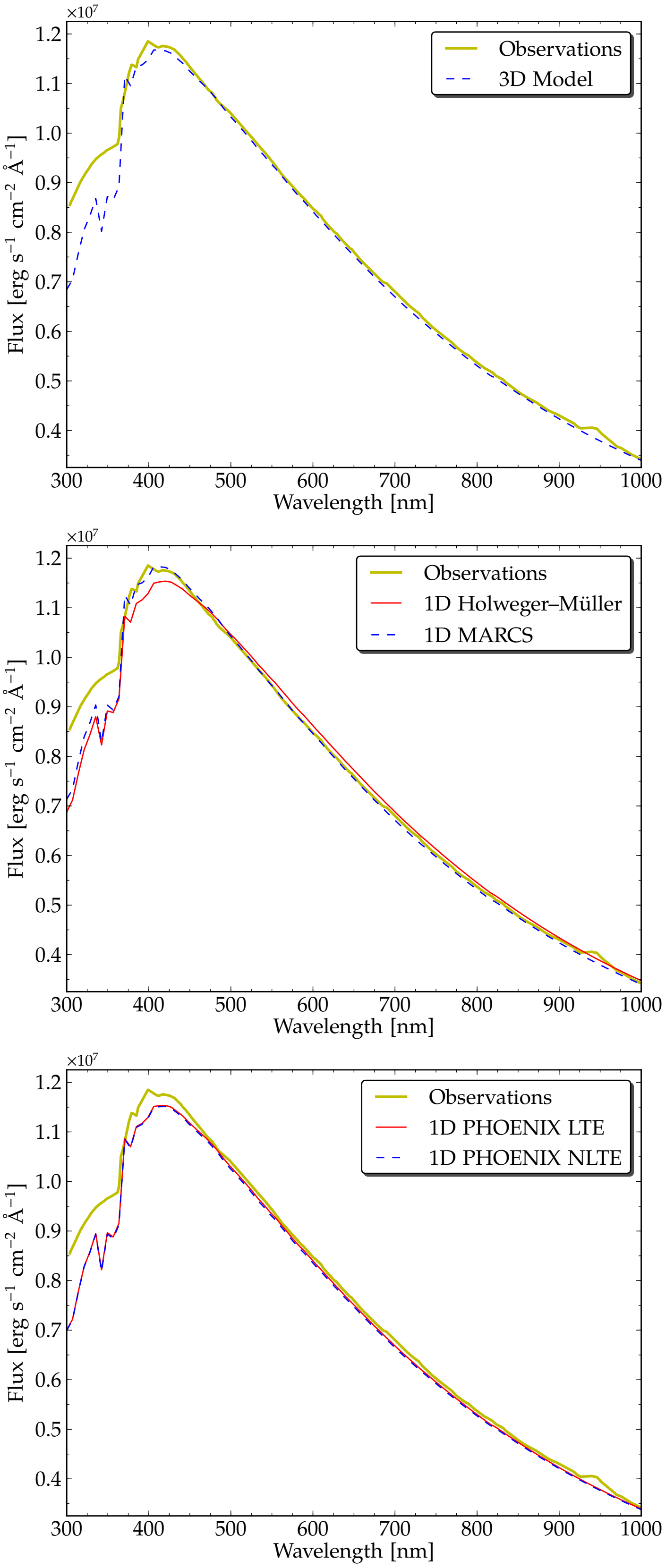

Figure 2.7 Absolute continuum fluxes for the models and observations.

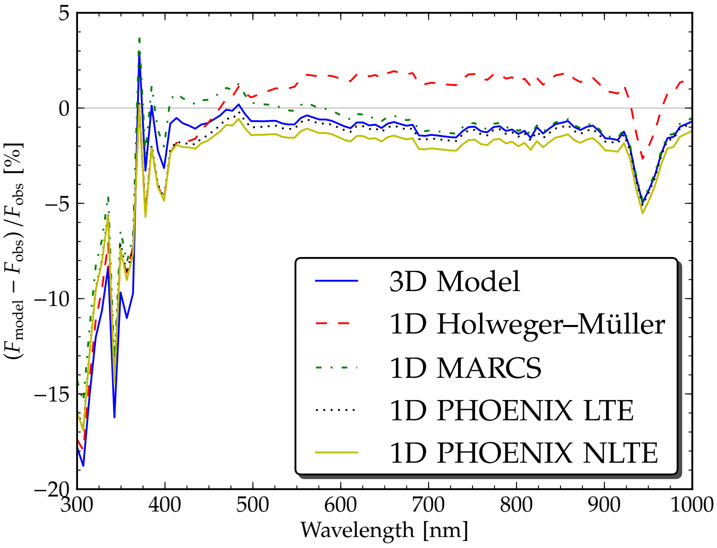

Figure 2.8 Continuum flux differences between the models and the observations. For $\lambda \lesssim 450$ nm the observations are not very reliable because of difficulties in continuum placement. The feature at $\lambda \approx 950$nm is likely to be caused by uncorrected telluric absorption in the observations.

2.5. Continuum intensity distribution

Another relevant test of the 3D model is that of the continuum intensity distribution and contrast ΔI_{rms}. It quantifies the fluctuations of the continuum intensity over the granulation. Historically, several studies have found the observed ΔI_{rms} to be lower than that of the 3D simulations even after consideration of atmospheric and instrumental seeing effects (*e.g.* Nordlund, 1984; Uitenbroek et al., 2007). However, Wedemeyer-Böhm & Rouppe van der Voort (2009, hereafter WR09) show that when the telescope's image degradation is carefully modelled, the continuum intensity distribution and ΔI_{rms} agree very well with the 3D models.

We compare our 3D model with the observations and the CO^{5}BOLD 3D model results from WR09. The comparison is made between the raw simulations (no image degradation

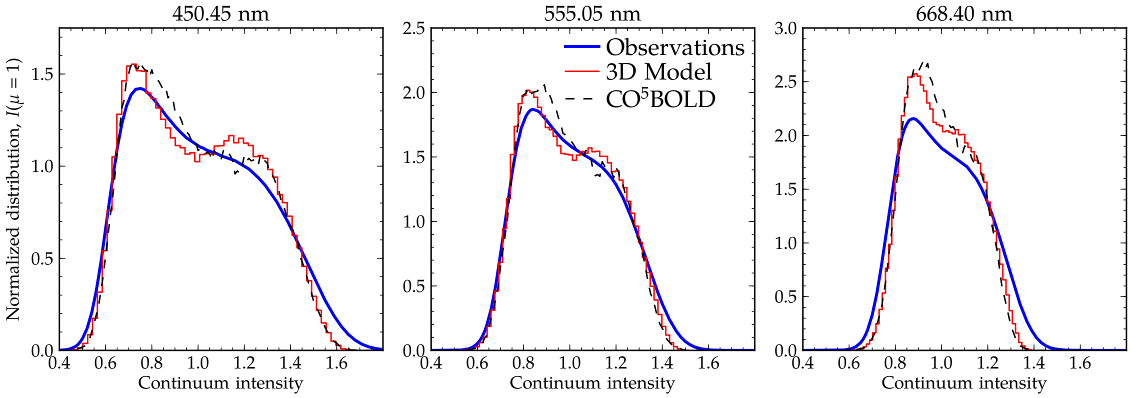

Figure 2.9 Continuum intensity distributions for the solar disk-centre for three wavelengths, as a function of the normalized continuum intensity. Observations (*thick blue line*) CO^{5}BOLD (*dashed line*) results from from Fig. 5 of WR09. The intensity distributions (*histogram*) for our 3D model were averaged over 90 simulation snapshots.

applied) and the SOT/Hinode observations deconvolved with the PSF (in an attempt to cancel out the image degradation). Results for the disk-center intensity distributions at three wavelengths are shown in Fig. 2.9. The ΔI_{rms} values for the same wavelengths are given in Table 2.1.

We find that our 3D model reproduces the observations well. Its ΔI_{rms} is slightly higher than CO^{5}BOLD, but otherwise results from the two models are very close, which is encouraging.

Table 2.1 Disk-centre ΔI_{rms} for the deconvolved observations, our 3D model and the CO^{5}BOLD 3D model. Observations and CO^{5}BOLD results from WR09.

ΔI_{rms} [%]	λ [nm]		
	450.45	555.05	668.40
Observations	26.7 ± 1.3	19.4 ± 1.4	16.6 ± 0.7
3D model	25.4 ± 0.8	18.6 ± 0.6	14.3 ± 0.5
CO^{5}BOLD	25.0 ± 0.1	18.1 ± 0.1	13.8 ± 0.1

2.6. Conclusions

Realistic solar atmospheres are of paramount importance for our understanding of not just the Sun but also of observations of other stars. The Sun provides an ideal test bench to test the physical ingredients of the models, which can then be applied to other stars. A critical requirement for a realistic model is that its thermodynamical quantities such as temperature, density and pressure match those of the real Sun. In this work we have undertaken a systematic study of the temperature structure of several solar models, using two 'classical' tests: continuum centre-to-limb variation and absolute continuum fluxes, and also the intensity fluctuations over the granulation for the 3D model.

The 1D theoretical models agree well with the observed absolute continuum fluxes, especially the MARCS model. However, both the MARCS and the PHOENIX models predictions for the centre-to-limb variations do not provide a reasonable match to the observations, neither in the visible nor in the infrared.

We find that the small difference in the temperature structure between the PHOENIX LTE and NLTE models does not translate into any significant difference in our comparison. Their results are very similar. If anything, the NLTE model performs slightly worse against the observational tests. This is likely to result from its steeper temperature gradient, due to NLTE cooling of the outer layers.

In all diagnostics we find that the 3D model reproduces the observations very well. This is especially true for the centre-to-limb variations, where its remarkable agreement surpasses even that of the semi-empirical Holweger–Müller model, which was built to fit the centre-to-limb variations. The 3D model also performs very favourably against the absolute continuum fluxes observations. In terms of the tested continuum intensity fluctuations over the solar granulation, it is reassuring to find that the 3D model reproduces the observed intensity distribution and ΔI_{rms} well.

The agreement in temperature structure between the 3D model and the observations is a good example of its degree of realism. Together with its realistic velocity fields and treatment of convection, it places the 3D modeling in an excellent position to perform chemical abundance studies.

CHAPTER 3

Oxygen lines in solar granulation at high resolution

T. M. D. Pereira, D. Kiselman, M. Asplund, *A&A in press*

Abstract

Aims: We seek to provide additional tests of the line formation of theoretical 3D solar photosphere models. In particular, we set out to test the spatially-resolved line formation at several viewing angles, from the solar disk-centre to the limb and focusing on atomic oxygen lines. The purpose of these tests is to provide additional information on whether the 3D model is suitable to derive the solar oxygen abundance. We also aim to empirically constrain the NLTE recipes for neutral hydrogen collisions, using the spatially-resolved observations of the O I 777 nm lines.

Methods: Using the Swedish 1-m Solar Telescope we obtained high-spatial-resolution observations of five atomic oxygen lines (as well as several lines for other species, mainly Fe I) for five positions on the solar disk. These observations have a high spatial (sub-arcsecond) and spectral resolution, and a continuum intensity contrast up to 9% at 615 nm. The theoretical line profiles were computed using the 3D model, with a full 3D NLTE treatment for oxygen and LTE for the other lines.

Results: At disk-centre we find an excellent agreement between predicted and observed line shifts, strengths, FWHM and asymmetries. At other viewing angles the agreement is also good, but the smaller continuum intensity contrast makes a quantitative comparison harder. We use the disk-centre observations we constrain S_H, the scaling factor for the efficiency of collisions with neutral hydrogen. We find that $S_\mathrm{H} = 1$ provides the best match to the observations, although this method is not as robust as the centre-to-limb line variations to constrain S_H.

Conclusions: Overall there is a very good agreement between predicted and observed line properties over the solar granulation. This further reinforces the view that the 3D model is realistic and a reliable tool to derive the solar oxygen abundance.

3.1. Introduction

One of the significant problems in modeling photospheres is how to accurately treat convection. Three-dimensional time-dependent hydrodynamical simulations of convection in solar and stellar photospheres are a major leap forward in the treatment of convection and realistic physics. They challenge the classical approximations: plane-parallel photospheres, static hydrostatic equilibrium and the mixing-length theory of convection.

Employing the family of convection simulations of Stein & Nordlund (1998), the series of papers started by Asplund et al. (2000a) has undertaken a systematic study of solar line formation and elemental abundances. The solar abundances derived from these models (Asplund et al., 2005a, 2009) represent a downward revision of the solar metalicity by almost a factor of two. The significance of this revision echoes over many fields of astrophysics, because the Sun is a reference in abundance studies. In solar physics it has sparked much debate, mostly because the excellent agreement between the solar interior models and measurements from helioseismology is lost when using the revised solar abundances (Bahcall et al., 2005). Despite numerous tries (see review of Basu & Antia, 2008), no work has successfully reconciled this excellent agreement with the new solar abundances.

Realistic physics, absence of free-parameters governing turbulence and the excellent observational agreement of predicted spectral line shapes (Asplund et al., 2000a) are some of the strong points in favour of the 3D models. Yet the disagreement with solar interior models and helioseismology has driven the question: are the 3D models suitable to abundance analysis?

This work is part of an effort to addresses several observational tests in order to answer this question. In particular, we use high-spatial-resolution observations to test the 3D model and line formation over the solar granulation, and at different viewing angles. A robust test of the models can be established by comparing the observed and predicted properties of spectral lines over the range of temperatures and velocities found in the solar granulation. Looking at different angles (or positions on the solar disk) one can also probe higher photospheric layers and non-vertical velocity components. Such testing has been briefly discussed by Asplund (2005). The series of papers started by Asplund et al. (2000a) shows that the 3D models reproduce the observed mean spatial line profiles very well. In this work we aim at resolving those mean line profiles and test the 3D models for a few lines.

We take a special interest in oxygen lines. Oxygen is pivotal in the solar abundance revision. Not only because it is abundant but also because abundances of several other elements are determined by their ratios to oxygen. After the work of Asplund et al. (2004) several new determinations of the solar photospheric abundance have been made: either using a different family of 3D models (Caffau et al., 2008a; Ayres, 2008) or different methods (Socas-Navarro & Norton, 2007a; Centeno & Socas-Navarro, 2008). The discussion provided by these studies prompts us to revisit the spectral indicators of oxygen. We propose to study some of the oxygen lines used in the abundance analysis. High-spatial-resolution observations of five atomic oxygen lines were obtained for this purpose. Observations were also obtained for other lines close to the target oxygen lines, and we have included some of them in our analysis (mainly Fe I lines, see Table 3.2).

This work is closely related to Chapter 4, which focuses on the centre-to-limb variation of oxygen lines. We make use of the same observations, but here we focus on high-spatial-resolution, whereas Chapter 4 studies the spatially and temporally averaged spectra as a function of viewing angle. The discussion here is primarily focused on the disk-centre granulation, because at disk-centre the contrast in intensity between granules and intergranular regions is highest. This greater contrast gives more information about the variation of spectral lines than at other viewing angles.

To study the line parameters we employ a similar methodology as Kiselman (1994). We study the variation of line strengths, shapes and shifts over the observed granulation and compare it with the 3D model. For the O I 777 nm triplet lines, known to suffer departures from LTE (*e.g.* Eriksson & Toft, 1979; Asplund, 2005; Fabbian et al., 2009), we seek to find whether the spatially-resolved disk-centre observations can constrain the NLTE line formation, as has previously been done using the centre-to-limb variations (Allende Prieto et al. 2004; Chapter 4).

The outline of this paper is as follows. In §3.2 we detail the observations. In §3.3 we describe the data reduction procedure. Next, in §3.4, we provide details of the 3D model used, the line formation, atomic data and how the model results were degraded to the observed conditions. In §3.5 we present the results and discuss their significance. Finally, we establish some conclusions in §3.6.

3.2. Observations

3.2.1. Telescope, instruments and programme

The observations were acquired using the Swedish 1-m Solar Telescope (SST) (Scharmer et al., 2003a) on Roque de Los Muchachos, La Palma. The observations took place from the 14th till the 29th of May, 2007.

Our aim was to obtain high-quality spatially-resolved spectra across the solar disk: from the disk-centre to the solar limb, with a high spatial and spectral resolution. We made use of TRIPPEL: the TRI-Port Polarimetric Echelle-Littrow spectrograph[1]. The slit width is 25 μm, which translates to 0.11 arcsec. The spectral resolution ($\lambda/\Delta\lambda$) is $\approx$200 000. TRIPPEL allows the simultaneous observation of three wavelength regions (spectrograph ports). To obtain spatially-resolved spectra along the slit, there is no predisperser. All spectral orders are overlapped and order selection is done by using filters.

The spectrograph cameras used were two MegaPlus 1.6 cameras (615 and 777 nm windows) and one MegaPlus II es1603 camera (630 nm window). In addition to the spectrograph and its three cameras, we operated four imaging cameras: three slit-jaw image cameras (at the wavelengths of 630, 694 and 773 nm, synchronized with the spectrograph's cameras) and one 'blue' camera with a Ca II H filter, using a dichroic beam splitter for $\lambda \lesssim 500$ nm. The slit-jaw cameras allowed for structure identification; the Ca H camera was used as a monitor of magnetic activity. The exposure times used were in the range of 30 - 265 ms, depending on the filters and the position on the solar

---

[1] See http://dubshen.astro.su.se/wiki/index.php/TRIPPEL_spectrograph.

disk. With neutral density filters to ensure identical exposure times, the slit-jaw cameras were synchronized with the spectrograph's cameras.

Our main target being oxygen lines, the filters for the three wavelength regions of the spectrograph were the following: 615.40, 630.08 and 777.52 nm (filter transmission windows are between 5.1-6.8 nm, centered on the filter wavelength). Hereafter referred as 615, 630 and 777 regions, they correspond respectively to the spectrograph orders 37, 36 and 29. These wavelength regions allowed us to observe the O I 615.81 nm line, the [O I] 630.03 nm line and the three O I triplet lines around 777 nm. A summary of the lines of studied in these three regions is given in Table 3.2.

High-spatial and spectral resolution observations of these lines were obtained for several positions on the solar disk, from the centre to the limb. The positions in the disk are defined by $\mu \equiv \cos\theta$, where θ is the heliocentric viewing angle. Because the 3D models used do not include magnetic fields, our aim in this work is to study the quiet Sun. While observing, efforts have been made to avoid regions with obvious magnetic fields (*e.g.* by using the Ca H camera). However, magnetic fields in the Sun can never be completely avoided.

In total more than 890 000 images were taken. The data were taken in a variety of seeing conditions, hence the same quality was not possible for all observing runs. Extensive use was made of the SST's Adaptive Optics system (Scharmer et al., 2003b). Some difficulties of acquiring AO lock were experienced close to the limb where the contrast of solar features is usually low. In some cases (notably $\mu = 0.4$) targets with higher contrast, like facular points, were chosen to facilitate locking. These structures were presumably magnetic features and the procedure thus somewhat compromised the effort to observe as quiet sun as possible. Another systematic difference between datasets results from the fact that the disk-centre observations had higher priority. Thus more time was spent on them and they happened to catch the moments of best seeing.

Details about the data and the coordinates in the Stonyhurst system (Cortie, 1897) can be found in Table 3.1, and the observed locations on the solar disk are shown in Fig. 3.1. For the 777 nm camera at $\mu \approx 0.8$ the dataset from the 25th of May was used. This was due to problems with a misaligned 777 nm filter for the 27th May set (the adopted set for the other cameras).

Table 3.1 Observing runs selected for analysis. Coordinates are given in the Heliographic Stonyhurst system. The spread in μ is given by the approximate spatial coverage of the slit. The ΔI_{rms} is given as the maximum continuum contrast of a single frame in the 615 nm wavelength region.

UT Date	μ	Coordinates	ΔI_{rms} [%]
20/5/2007 08:00	0.999 ± 0.001	0.2S, 0.5E	9.2
25/5/2007 08:30	0.816 ± 0.010	26.7N, 22.1E	5.4
27/5/2007 15:30	0.793 ± 0.012	1.3N, 37.5W	6.0
25/5/2007 09:56	0.608 ± 0.020	51.1S, 3.7E	4.7
20/5/2007 09:27	0.424 ± 0.024	29.9S, 61.4W	5.2
25/5/2007 07:40	0.197 ± 0.003	18.0S, 82.4E	3.4

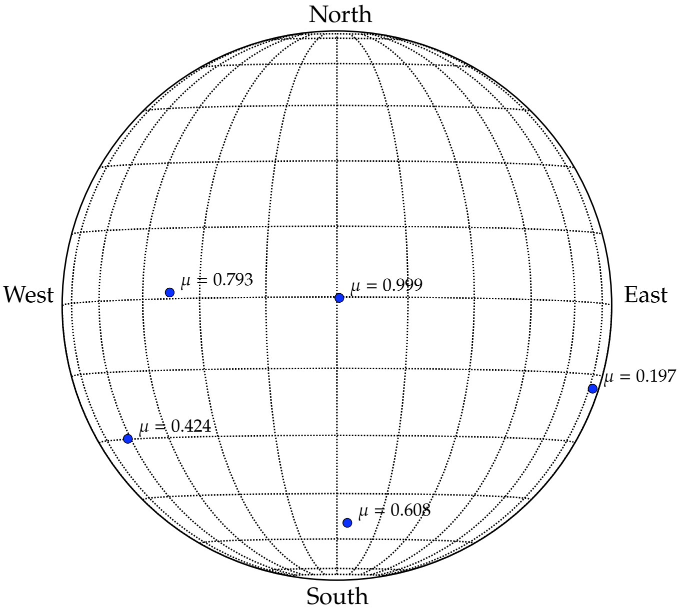

Figure 3.1 Position of the observations on the solar disk, in heliographic Stonyhurst coordinates. The figure has been centered in the heliographic latitude of the observer (≈ −1.8°for our dates).

3.2.2. Pointing accuracy

To minimise the spread in μ for each data set, a position on the disk was chosen so that the slit was parallel to the closest part of the limb. The field of view is rotating in the laboratory frame and thus the position angle of the selected locations changed during the day. This explains the scattered appearance of the points in Fig. 3.1.

The SST's blind pointing is not precise enough for μ to be determined with the required precision close to the limb. We took advantage of the Dutch Open Telescope (DOT) to help with the coordinates. With the kind assistance of P. Sütterlin, the DOT was pointed at the same solar region as the SST by comparing the Ca II H filtergram view of the two telescopes. The heliographic coordinates were thus read from the DOT. The spread in μ in Table 3.1 is due to the range of μ covered by the slit.

Note that the outermost images around $\mu = 0.2$ have a very well-defined μ because the limb was in the field of view of the slit-jaw images, which allowed precise measurements. This explains the small spread in μ for that position.

3.3. Data reduction

3.3.1. Dark currents, flat fields and spectrograph distortions

The first step in the reduction was the subtraction of the dark currents and division by a normalized flat field image. Darks were obtained by blocking the sunlight. Because of the features on the solar surface and the presence of the spectral lines, the task of obtaining a uniformly exposed flat field needs a more elaborate approach. The telescope is operated in a special mode where it scans randomly quiet areas at the disk-centre. A reference disk-centre spectrogram is obtained by averaging these images. The spectral lines are removed by dividing this spatially uniform spectrogram by its mean spectrum (spatial average), and a flat field image is obtained[2]. This disk-centre mean spectrum is also used for wavelength, intensity and scattered light calibrations, as detailed below.

Once corrected for dark currents and flat fielded, the images need to be corrected for the spectrograph's distortions: smile and keystone. The aim is to rectify the spectrogram, to have the dispersion exactly perpendicular to the pixel rows. Smile curves the spectral lines across the spatial axis, whereas keystone curves them across the spectral axis. The distortion is computed by fitting a fourth order polynomial to the line centres of a few lines along the slit (in a spatially uniform image). This information is used to compute the transformation to invert the distortion and interpolate the spectrogram into a rectified version. The images are then cropped in the spatial and spectral directions, to remove the areas of the CCD not covered by the spectrograph image. After the cropping the images obtained have about 900 pixels in the spatial direction and 1400 pixels in the spectral direction.

3.3.2. Wavelength and intensity calibrations

Wavelength calibration is made by comparison with the reference FTS atlas of Brault & Neckel (1987). Using the disk-centre mean spectrum obtained from the flat fielding procedure, for each wavelength region a few lines are identified in the mean spectrum and in the FTS atlas. Their line centres are computed and a polynomial is fitted to the dispersion relation (wavelength/pixel number) – yielding a wavelength scale for our images. The precision of this wavelength calibration has proven to be more than enough for our purposes. When computing the line shifts across the solar granulation, velocity measurements are made relative to the reference mean spectrum (the spatial and temporal mean of the images at a given μ) – thus a very precise absolute wavelength calibration is not required.

In the 630 nm wavelength region there are a few telluric lines. They provide a much more robust wavelength reference for computing line shifts. We have compared the results in line shifts using a reference from our standard wavelength calibration and using telluric lines as a reference. The difference in these approaches is found to be less than 40 $\mathrm{m\,s^{-1}}$, which gives us confidence in our wavelength calibration.

All spectral intensity measurements are made relative to the observed disk-centre intensity. In the flat fielding method described above, a spatially and temporally averaged reference disk-centre spectrum (hereafter referred as 'mean spectrum') is obtained. The intensity of each spectrogram observed at a given position on the solar disk is then divided by the (continuum) intensity of the mean spectrum.

For the same exposure times, the exposure level varies with time-dependent factors, most importantly airmass. Because the flat fields are also used to calibrate the intensity, it is important to have the exposure levels of flat fields and observations as close as possible. To minimize for the time-dependent factors the observations and the mean spectrum are obtained in close intervals (20-30 min). These intervals are usually enough to keep the same exposure level between observations and flat-fields (for the mean spectrum). However, in the early morning and late afternoon when the airmass varies

---

[2] For the spectrograph's cameras. For the imaging cameras the flat-field is simply the normalized averaged of the many disk-centre images.

quickly with time it is necessary to correct for the different airmasses. Our approach is empirical: using several thousand slit-jaw images for the given airmass interval, we fit the terrestrial atmospheric absorption coefficient $\tau_{\oplus}$ from the logarithmic intensity *vs.* airmass relation.

We assume the terrestrial atmospheric extinction to be given by:

$$I = I_0 \exp(-a\tau_{\oplus}), \tag{3.1}$$

where a is the airmass. The airmass correction factor is then the ratio of flat fields/observations intensity:

$$I_{\text{factor}} = \exp(-\tau_{\oplus}[a_{\text{ff}} - a_i]), \tag{3.2}$$

where a_{ff} is the mean airmass when the flat fields were taken and a_i the airmass when each image was taken. The slit-jaw images are then used to derive $\tau_{\oplus}$ empirically. After flat-fielding and correcting for dark currents, its mean intensity is obtained by averaging a big area. Using the mean intensities and the airmasses of each slit-jaw image, we perform a linear fit to the $\log(I)$ vs. airmass relation, obtaining τ and $\log(I_0)$. The $\tau_{\oplus}$ coefficient is computed using the slit-jaw images for the 630 nm and 777 nm wavelengths. Since a similar camera was not available for the 615 nm region, its value of $\tau_{\oplus}$ was extrapolated from the other two. This airmass correction was only applied for the observations taken in the early morning and late afternoon – in other cases the slow variation in airmass makes the empirical determination of $\tau_{\oplus}$ very uncertain.

Another necessary intensity correction is related to the shutter mechanism in the MegaPlus cameras. The mechanical curtains of the shutter control the exposure time. In some circumstances we find that they are not perfectly synchronized: odd and even images have different exposure levels – possibly because some part of the shutter curtains is very briefly in front of the CCD during exposure. These differences depend on the exposure time (the shorter, the bigger the difference), but are usually less than 1% of the mean intensity of each frame. This effect is corrected by scaling the exposure level of each odd/even frame by the ratio of the mean intensity to odd/even intensity. Unfortunately this effect also introduces a slope in the spectra, that is corrected for in our normalization procedure detailed in the next subsection.

3.3.3. Correction for straylight in the spectrograph

Light scattered off the grating of the TRIPPEL spectrograph as well as from other internal sources introduces straylight in the spectra. In our treatment for straylight, we have assumed that it is constant along the slit and is proportional to the mean intensity of light entering the spectrograph. Our treatment was based on routines used in Allende Prieto et al. (2004), that were kindly provided by C. Allende Prieto. The relative level of straylight, given as a fraction of the continuum intensity, is computed using the FTS atlas and the calibration disk-centre mean spectrum. First the mean spectrum is normalized. Assuming that the spectrograph's instrumental profile is Gaussian, we derive the straylight level and the resolution relative to the FTS atlas by comparing our mean spectrum with the atlas (convolved with a Gaussian for an arbitrary resolution). The approach searches for the best fitting values of the straylight and the FWHM of the convolving Gaussian. Using an iterative χ^2 minimization, the best fitting pair is found.

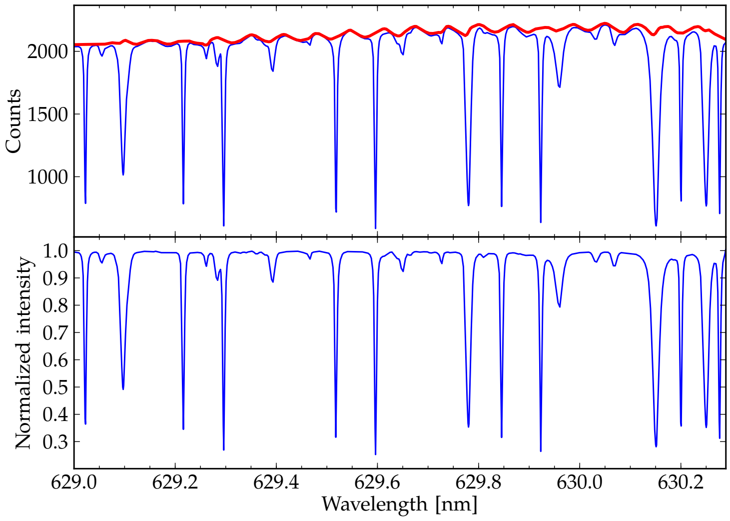

Figure 3.2 Normalization of the mean spectrum, for a frame in the 630 nm region affected by fringing. Top: mean spectrum before normalization (blue line), continuum map from our algorithm (red line). Bottom: mean spectrum after normalization.

This straylight and resolution represent the parameters that best 'map' the FTS atlas into our mean spectrum. This procedure is repeated for each wavelength region and each data subset. We find a straylight level of ≈6%, which is in agreement with other observations with this instrument (*e.g.* Langangen et al., 2007). This relative straylight level is then subtracted from each spectrogram.

3.3.4. Normalization

Normalization of the spectrogram is one of the most important steps of the reduction. There are several factors that determine the overall shape of the spectra: filter transmission function, grating blaze function, vignetting, fringing, etc.. Flat fielding removes most of the fringing, however our procedure will leave traces of fringe components parallel to the spectral lines. Our approach to normalization is a 'one-fits-all', in which we correct for all these effects in one step. Once again, the FTS atlas is used. It is assumed that it perfectly reproduces the mean spectrum at disk-centre. Our procedure is to find the transformation that maps the continuum of our mean spectrum into the continuum of the FTS atlas. This is done by first convolving the atlas with a Gaussian instrumental profile. Our mean spectrum is then divided by the atlas and a 'continuum map' is obtained by smoothing this ratio. We find that this procedure is extremely efficient at removing fringing and other artifacts. Due to the filter position the wavelength region around 630 nm happened to be the most affected by fringing. Figure 3.2 gives an example of how the continuum finding procedure works in this region.

Because there is no absolute intensity calibration, normalization of the calibration mean spectrum defines the disk-centre intensity. All spectrograms are divided by the corresponding continuum map, which traces the continuum level in the mean spectrum. This ensures that all the distortions in the spectra are corrected. The next step is to find the continuum level, and for each spatial point, as it varies along the granulation pattern. This is done by identifying the continuum regions in the spectrum (defined as points where $I \gtrsim 0.995$ in the FTS atlas). The continuum level is taken as the mean intensity in such regions.

In the course of our data reduction we noticed a spectral distortion that was not canceled out by using the reference continuum map. This was a slope in the spectrum for every odd image, and is related to the MegaPlus shutter problem described in the previous subsection. Because the mean spectrum is obtained by averaging 1000 exposures, the odd-even effect is averaged in the continuum map. Removal of the spectral slope associated with this effect needs to be done individually for each image. Therefore, a procedure was implemented to remove this slope in each spectrogram, by fitting (and subtracting) a straight line. This was done just before finding the continuum level.

3.3.5. Frame selection and sampling

In our observations more than 392 000 spectrograms were obtained. From these, only about 500 were actually used in the analysis. The most important criterion for data selection was the continuum intensity contrast. The maximum values for the continuum contrast for the 615 nm are shown in Table 3.1. The disk-centre value of 9.2% demonstrates the excellent quality of the data. It can be compared with other values obtained with slit spectrographs, like the ≈ 7% at 615 nm of Kiselman (1994) with the SVST and the 7% at 630 nm[3] obtained by Danilovic et al. (2008) with the SOT/SP of the Hinode space telescope.

Continuum contrast is a good measure of quality for quiet Sun regions, but cannot be used blindly. Some magnetic features are difficult to identify just by visual inspection of the slit-jaw images, and can artificially increase the continuum contrast. Because the present work is concerned with quiet regions, some subsets had to be removed from the analysis because they were suspect of having magnetic effects (*e.g.*, excessively bright spatial points). Other sets displayed an excessive amount of fringing that could not be completely corrected, and therefore were discarded. The best subset for each μ value was used. From each subset selected for analysis the best 25 images were used, except for disk-centre where the best 50 images were used.

In Figure 3.3 an example spectrogram is displayed, showing the effects of reduction in the image.

An important aspect of the selected frames is the temporal and spatial sampling. With the simulations we have a very good time and spatial sampling of the solar granulation. However this is not always possible with the observations if we want to select the best continuum contrast. The observations with higher contrast will tend to be clustered in the instants with better seeing, which do not provide the best sampling. There is a trade-off between getting the highest quality images and getting the best sampling. In this work we have sought the higher quality images, at the expense of sampling.

A spatial sampling as good as the simulations will always be difficult to achieve because the models have a two dimensional sampling of the solar surface, while the spectrograph's slit is only one dimensional. Our slit covers ≈ 40 arcsec, while the models cover a box of $\approx 8 \times 8\,\mathrm{arcsec}^2$. In the time domain the simulations have a better coverage (20 snapshots uniformly sampled from 45 minutes of solar time). Our observations at disk-centre cover slightly more than 10 minutes, while at other viewing angles the time coverage

---

[3] The continuum contrast is inversely proportional to wavelength (approximately). Our value of 9.2% at 615 nm corresponds to ≈9.0% at 630 nm.

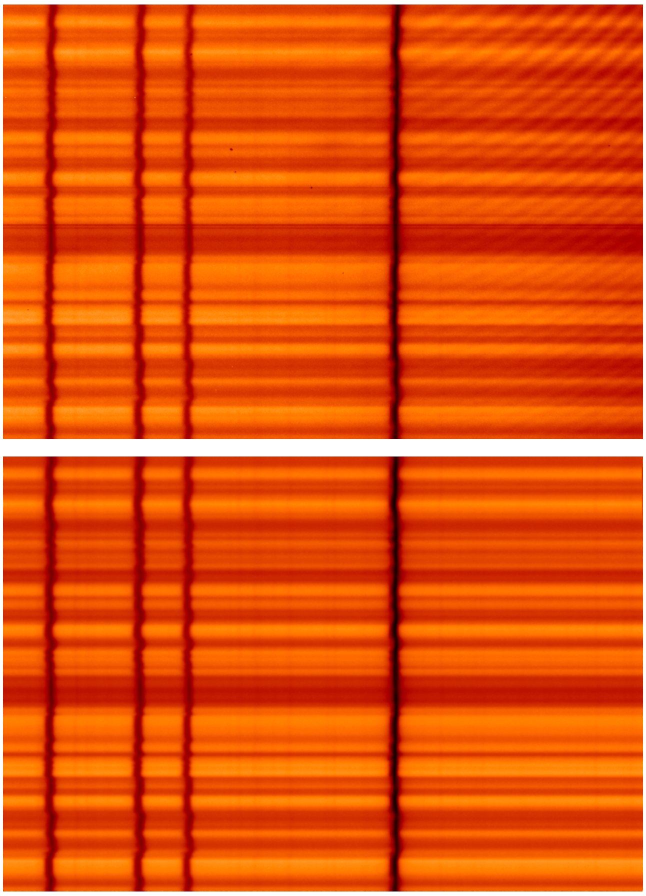

Figure 3.3 Example spectrogram for the 777 nm region before (top) and after (bottom) the reduction. In the final reduced image distortions and inhomogeneities such as the fringing pattern in the top right; vignetting; continuum function and dust specs in the CCD have been corrected. The vertical axis represents spatial position and the horizontal axis wavelength. The three vertical lines on the left are the O I 777 nm lines, and the darker line on the right is the strong Fe I 778.05 nm line.

is typically of a few minutes. The solar 5-minute oscillations will influence the line properties (mainly velocities), so a good temporal sampling is important to average the oscillations, which are also present in the simulation. For our disk-centre data the coverage is adequate for this purpose, but for other viewing angles it is not so good. The problem of systematics in the line shifts for $\mu \neq 1$ due to solar oscillations has been minimized by measuring the line shifts relative to the spatially and temporally averaged spectrum for the given μ, and not from the mean disk-centre spectrum.

3.3.6. Fourier filtering

The signal-to-noise ratio of each individual spatially-resolved spectrum is on the order of 25-50, depending on the camera used and the exposure level. To minimize this noise a Fourier filter was implemented. Because the spectrograms are oversampled[4] in the spatial and wavelength directions a Fourier filter is very effective at minimizing the noise with little loss of signal. Given that on the spectrograms noise has a much higher spatial frequency than the spectral lines, a low-pass filter eliminates the noise while preserving the spectral information. Working on the Fourier space the high frequencies are filtered out by multiplying the two dimensional Fourier transform of the spectrogram by a low-pass filter function, and taking the inverse Fourier transform to obtain the

---

[4] There are at least 5 pixels per resolution element in the spatial axis and 3 in the wavelength axis.

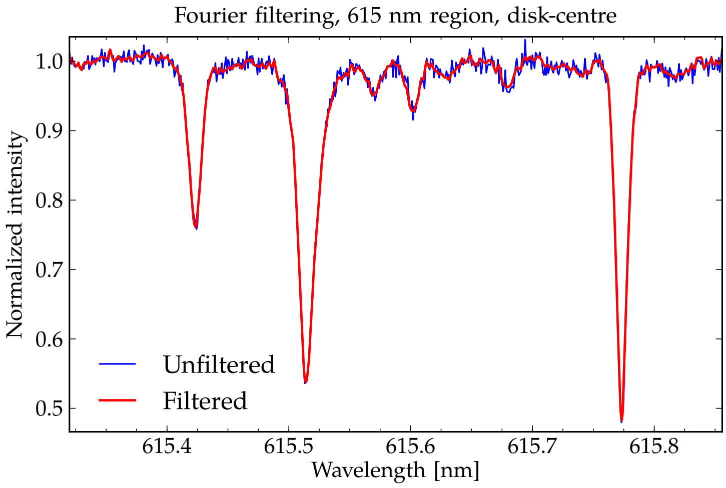

Figure 3.4 Effect of the Fourier filter in a spectral region around 615 nm. The high-frequency noise components are eliminated in the filtered spectrum.

filtered data. For the filter function we use a two dimensional Butterworth filter with an elliptic shape, defined as:

$$D = \left(\frac{f_x}{c_x}\right)^2 + \left(\frac{f_y}{c_y}\right)^2 \tag{3.3}$$

$$F = \frac{1}{1 + D^n}, \tag{3.4}$$

where n is the order of the filter, D is the distance in the two dimensional frequency space (f_x, f_y), c_x and c_y are the cutoff frequencies in x and y. An order of $n = 20$ was used, and the chosen cutoff frequencies were $c_x = c_y = 0.1\ \mathrm{pix}^{-1}$. These values ensured that a significant part of the noise was eliminated while retaining the spectral information. The smooth dip in the function ensures that Fourier artifacts such as the Gibbs phenomenon are minimized. Being a two dimensional problem, noise in both axes of the spectrogram (wavelength and spatial coordinate) can be treated differently by setting different values for c_x and c_y.

Even with the conservatively chosen cutoff frequencies, Fourier filtering significantly increases the signal-to-noise ratio. Its effects are very helpful for a precise continuum determination and for very weak lines. Fig. 3.4 shows an example of the effects of the filtering.

3.3.7. Extracting line quantities

Five line properties are extracted from the spectra: line-centre position, line-centre intensity, full width at half maximum (FWHM), a measure of line asymmetry, equivalent width. These are computed automatically (i.e., no human input in the fitting procedures) using algorithms designed for the effect.

We define ‘line centre’ as the velocity difference in km s^{-1} between the line centre of the mean spectrum (spatial and temporal average the spectra at the given μ value) and the line centre for the spectrum of a given spatial point. The line centre wavelength and intensity are obtained by fitting a parabola to a few points around the line minimum.

The velocity shift is then computed using the mean spectrum and converting wavelength to velocity units. The line centre intensity is given in relative intensity units.

The line FWHM is computed by fitting the line wings and measuring the width at half maximum. Two 5th order polynomials are fitted to the red and blue wings of the line being analyzed. The fitted functions are then evaluated at the half maximum of the line, and the wavelength distance between red and blue wings is measured. This distance corresponds to the FWHM, and is converted to velocity units. The quantity 'line asymmetry' is computed in a similar way. The line asymmetry is defined as difference (in velocity units) between the line centre and the bisector at half maximum. The wavelength position of the line bisector at half maximum is obtained as the FWHM: from the fitted polynomials to the line wings. It is then subtracted from the line centre wavelength and converted to velocity units. Due to the fitting procedure, the FWHM and 'line asymmetry' are the quantities with the highest uncertainties.

The equivalent widths were computed by direct integration. For consistency both the observations and the (convolved) simulations were run through the same analysis procedure.

The uncertainties for all the line quantities reflect the photon noise and continuum placement errors. The effects of the photon noise, were estimated using artificial lines. To generate an artificial line with similar properties, a Gaussian was fitted to the mean spectrum of each line. This artificial line was then placed in a continuum region in a few spectrograms. Its quantities were computed in the usual fashion and the comparison between the Gaussian exact quantities with the extracted quantities yields the errors due to photon noise. The final errors were the quadratic sum of the photon noise and continuum placement errors. The continuum placement error was assumed to be 0.25% for all lines, for each spatially-resolved spectrum.

3.4. Simulations

3.4.1. Atmospheric model

The 3D line formation calculations presented herein have been performed with a 3D, time-dependent, radiative-hydrodynamical simulation of the solar photosphere (Trampedach et al., in preparation; Asplund et al., in preparation). This new 3D model differs in a number of ways from the 3D solar atmosphere of Asplund et al. (2000a) that has been extensively used for solar abundance purposes over the past decade (*e.g.* Allende Prieto et al., 2004; Asplund et al., 2004, 2005b). It has been computed with the STAGGER MHD code (Nordlund & Galsgaard, 1995; Gudiksen & Nordlund, 2005), although no magnetic field has been imposed for the present simulation. The code solves the hydrodynamical equations of mass, momentum and energy coupled with a solution of the 3D radiative transfer equation using nine directions (vertical direction plus 2 inclined with 4 azimuthal rays). The code makes use of periodic horizontal and open vertical boundaries. The Eulerian mesh consist of 240^3 cells, which corresponds to a physical dimension of $6{\times}6{\times}4$ Mm; the solar simulation extends about 900 km above the optical depth unity. For the subsequent line formation calculations the original simulation was interpolated to a finer vertical depth scale while sampling the horizontal directions to produce a 3D model of dimensions 50×50×82; test calculations confirmed that this procedure did not introduce any differences in the final results.

Compared to our previous 3D solar model, an extensive overhaul of the input microphysics and radiative transfer treatment has been carried out. The continuum and line opacities are based on the MARCS code (Gustafsson et al., 2008) supplemented by additional photo-ionization cross-sections from the Opacity and Iron Projects (Cunto et al., 1993; Hummer et al., 1993). The adopted equation-of-state is that of Mihalas et al. (1988). The Asplund et al. (2005a) solar chemical composition has been used both for the opacities and equation-of-state. The wavelength-dependence of the opacities have been accounted for using the concept of opacity binning (Nordlund, 1982). The division in opacity and wavelength for the 12 opacity bins was based on the full monochromatic (10^5 wavelength points) solution for the mean 3D stratification. Continuum scattering was included as a pure absorption (i.e. $S_\lambda = B_\lambda(T)$, which is fully justified for the solar photosphere (Hayek et al., in preparation).

The time-sequence of the 3D solar simulation utilized for the line formation calculations corresponds to 1.2 hr of solar time. The resulting effective temperature of the 90 snapshots is $T_{\rm eff} = 5778 \pm 14\,$K.

3.4.2. Line formation and departures from LTE

Using the 3D model described above we computed the synthetic line profiles using our LTE line formation code. From the full simulation a series of 20 snapshots covering ≈40 min of solar time has been used. The adopted snapshots were chosen so that the temporally averaged effective temperature of the atmosphere (not a free parameter in the simulation) was $T_{\rm eff} = 5777 \pm 14\,$K, very close to the observed nominal value of $5777 \pm 3\,$K (Willson & Hudson, 1988). While the full simulation has a numerical resolution of $150 \times 150 \times 82$, for the purposes of spectral line formation we have used an interpolated lower resolution of $50 \times 50 \times 82$. As outlined in Asplund et al. (2000a) this procedure is meant to save computing time and does not introduce any differences in the line profile shapes. Assuming LTE, the line formation code used a Planckian source function ($S_\nu = B_\nu$), and the Saha and Boltzmann equations to determine respectively the ionization fraction and atomic level populations for each species. For realistic equation-of-state and continuum opacities the Uppsala opacity package was employed. The radiative transfer equation has been solved for several directions: for each of the five μ positions of our observations the line profiles were computed over for four φ angles. For each line the profiles were computed using three abundance values, allowing for interpolation of other abundance values. No additional line broadening through micro or macroturbulence was applied.

The synthetic line profiles were computed assuming the LTE approximation. For oxygen lines it was possible to perform 3D NLTE line formation calculations. This was accomplished using the MULTI3D code (Botnen, 1997; Botnen & Carlsson, 1999; Asplund et al., 2003), which solves the rate equations iteratively using a local lambda operator and assuming statistical equilibrium. For the purposes of calculating the level populations, the radiative transfer in MULTI3D was solved for 40 outgoing inclined rays using a short characteristic technique. Once the level populations had converged and the iteration is finished, we made use of the resulting source function and opacities to compute the radiative transfer using a long characteristic Feautrier solver. Similarly to the LTE code, we compute the NLTE line profiles for the μ values of our observations, with 4 φ angles each. The Uppsala opacity package was used to compute the continuum opacities and equation-of-state for MULTI3D. For increased numerical accuracy, the 3D model fed into MULTI3D had a resolution of 100 points in the vertical scale, interpolated from the 82 points of the original 3D simulation.

Due to the computational expense, full 3D NLTE line formation was carried only for 10 snapshots of the simulation. The snapshots were selected to provide a good statistical coverage, both in time (evolution of granulation) and effective temperature. The final NLTE line profiles were obtained by multiplying the LTE line profiles (computed with our LTE code) by the NLTE/LTE ratio (computed with MULTI3D). The wavelength-dependent NLTE/LTE ratio was obtained for each snapshot, viewing angle and spatial point. Multiplication of the ratio by the line profiles is made individually for all spatially-resolved spectra and for each viewing angle and snapshot.

Because one has NLTE profiles directly from MULTI3D, it may seem counterproductive to obtain the final values by multiplying the LTE profiles by the NLTE/LTE ratio. However, this approach was followed for two reasons. First, to allow interpolation of the line profiles in abundance. Line profiles from MULTI3D are computed only for one abundance value, whereas for our LTE code they are computed for three values of $\log(\epsilon_{\mathrm{O}} \cdot gf)$. Interpolating between these three line profiles allowed us to calculate the line profile for an arbitrary oxygen abundance. The second reason this approach was taken was to ensure consistency between different lines by using the same line formation code. In any case, for the oxygen lines studied we find very little difference in the LTE line profiles between MULTI3D and our LTE code.

3.4.3. Atomic data

The two main sources of atomic data for our spectral calculations were the NIST database (Ralchenko et al., 2009) and the VALD database (Piskunov et al., 1995; Kupka et al., 2000). A summary of the lines properties and the sources used can be found in Table 3.2. Collisional (van der Waals) broadening was computed using the quantum mechanical theory of Anstee & O'Mara (1995); Barklem & O'Mara (1997); Barklem et al. (1998), eliminating the need for conventional Unsöld (1955) enhancement factors. The collisional broadening coefficients were computed for the oxygen lines and, when available, to other lines used in our analysis.

Aside from the lines listed in Table 3.2 we have included nearby blends in some line profiles. For the [O I] 630.03 nm we included the Ni I blend and for O I 615.81 nm we have included some weak molecular and atomic blends (for more details about the blends in these lines, see §4.4.3). In the line profiles of Si I 615.57 nm and Ca I 616.60 nm we have included both lines and also a nearby strong Si I line at 615.51 nm. In the case of Ca I 616.60 nm we have also included the very weak O I triplet at 615.60 nm. Data for all these lines were extracted from the VALD database. For the Ni I 630.03 nm line we use $\log gf = -2.11$ from Johansson et al. (2003).

Table 3.2 Lines studied in the present work and their parameters. Equivalent widths at disk-centre measured from our observations. Data sources: a) VALD database; b) NIST database; c) Nave et al. (1994); d) Storey & Zeippen (2000).

Atomic Species	λ [nm]	$\log gf$	E_{low} [eV]	$W_{\mu=1}$ [pm]
Fe I	615.1618^{c}	-3.299^{b}	2.18^{b}	4.95
Si I	615.5693^{a}	-2.252^{a}	5.62^{a}	0.61
Ca I	615.6023^{a}	-2.497^{a}	2.52^{a}	0.92
Fe I	615.7728^{c}	-1.260^{a}	4.08^{b}	6.45
O I	615.8186^{b}	-1.841^{b}	10.74^{b}	0.63
Fe I	615.9378^{c}	-1.970^{a}	4.61^{a}	1.21
Fe I	629.0965^{a}	-0.774^{a}	4.73^{a}	7.06
Fe I	629.7792^{b}	-2.740^{b}	2.22^{b}	7.54
[O I]	630.0304^{b}	-9.717^{d}	0.00^{b}	0.45
Sc II	630.0698^{a}	-1.887^{a}	1.51^{a}	0.59
O I	777.1944^{b}	0.369^{b}	9.15^{b}	8.48
O I	777.4166^{b}	0.223^{b}	9.15^{b}	7.44
O I	777.5390^{b}	0.002^{b}	9.15^{b}	5.90
Fe I	778.0557^{a}	0.029^{a}	4.47^{a}	14.81

For the NLTE calculations we employ a 23 level O atom (22 O I levels and the ground state of O II), including in total 43 bound-bound and 22 bound-free transitions. This atom is based on the atom of Kiselman (1993), but has undergone updates (Fabbian et al., 2009) as new data for electron-impact excitation has recently become available (Barklem, 2007).

3.4.4. Image degradation and instrumental profiles

To compare the simulations with Earth-based observations one needs to degrade them in a similar manner as the Earth's atmosphere and the telescope degrade the images from the Sun. Additionally, the spectra will also have to be convolved to account for the spectrograph's instrumental profile. We employ a three step convolution process that mimics the path of light from the solar surface to the spectrograph: atmosphere → telescope → spectrograph. The first step is the point-spread function (PSF) caused by the Earth's atmosphere. Following Nordlund (1984) and Collados & Vazquez (1987) we describe the atmospheric PSF as a sum of two Lorentzians:

$$p_{\mathrm{atm}}(r,a,b) = \frac{a}{r^2+a^2} + \frac{b}{r^2+b^2}, \tag{3.5}$$

where r is angular distance and we define $a > b$ so that the first Lorentzian determines the overall contrast ('extended wings' of the PSF) and the second Lorentzian determines the size of the smallest detail observable ('narrow core' of the PSF). Tests using different functions for the PSF show that the effect on the results is negligible.

Following the path of light, the next step is to mimic the finite resolution of the telescope. We employ an Airy disk function for a circular aperture telescope as the 'diffraction'

PSF:

$$x = \pi \frac{D}{\lambda} r \tag{3.6}$$

$$p_{\mathrm{diff}}(x) = \left[2 \frac{J_1(x)}{x} \right]^2 , \tag{3.7}$$

where D is the telescope's diameter, λ the wavelength of the observations, r the angular distance and J_1 a Bessel function of the first kind.

The combined PSF is then the convolution of p_{atm} with p_{diff}:

$$p(r,a,b) = \left[p_{\mathrm{atm}} * p_{\mathrm{diff}} \right] (r,a,b). \tag{3.8}$$

The PSF is normalized, so that the convolution with the images conserves the intensity. The a and b parameters depend on the local conditions and are empirically obtained. Two properties of the observations are used to constrain them: the continuum intensity contrast and the continuum intensity distribution. These two properties are not completely independent of each other: a change of the distribution will change the contrast and vice-versa. Nevertheless it is possible, for a fixed contrast, to change the shape of the distribution using different pairs of (a,b), and that is the approach taken. For the disk-centre data we adjust a and b in order to get the best agreement with the observed continuum intensity distribution and continuum contrast. Fig. 3.5 shows an example of how 777 nm data is convolved so that it agrees with the observations. By fitting the observed intensity distributions, the adopted PSF formulation also corrects for the non-ideal components of the telescope and instrument PSFs.

There is some degree of degeneracy in the intensity distribution for different values of a and b. The adopted PSF is not necessarily the most physically correct. It is rather an empirical transformation that best reproduces the observations, given the coarse spatial resolution of the simulations and the time-average of different seeing conditions that the observed intensity distribution represents. Several tests were made to study the effect of different PSFs in the results. In Fig. 3.6 we plot some results for two sets of parameters giving different PSFs: one with stronger wings (left column), and the other with weaker wings (right column). The difference in the intensity distributions given by these two PSFs is very small, as is the effect on the results (in this case, plotted for the line shifts, but the results are similar for other parameters). We conclude that the adopted PSF describes the observations reasonably, and the error introduced in the results by a different shape of PSF is small.

Stein & Nordlund (1998) hint at a good agreement between the 3D model intensity distibutions and the observations. Recent work has indeed shown that the intensity distribution of these and other simulations are consistent with observations once careful PSF modelling is performed (Wedemeyer-Böhm & Rouppe van der Voort, 2009; Danilovic et al., 2008). Wedemeyer-Böhm & Rouppe van der Voort (2009) also show that the observed centre-to-limb variation of the continuum contrast is well described by a 3D model of the Stein & Nordlund family.. Nevertheless, and for a fair comparison, we chose not to assume too much about the predicted intensity distributions at $\mu \neq 1$. Unlike at disk-centre, we do not force the model intensity distribution to match the observations. The parameter a is related to the PSF wings. Its sources are several: straylight in the

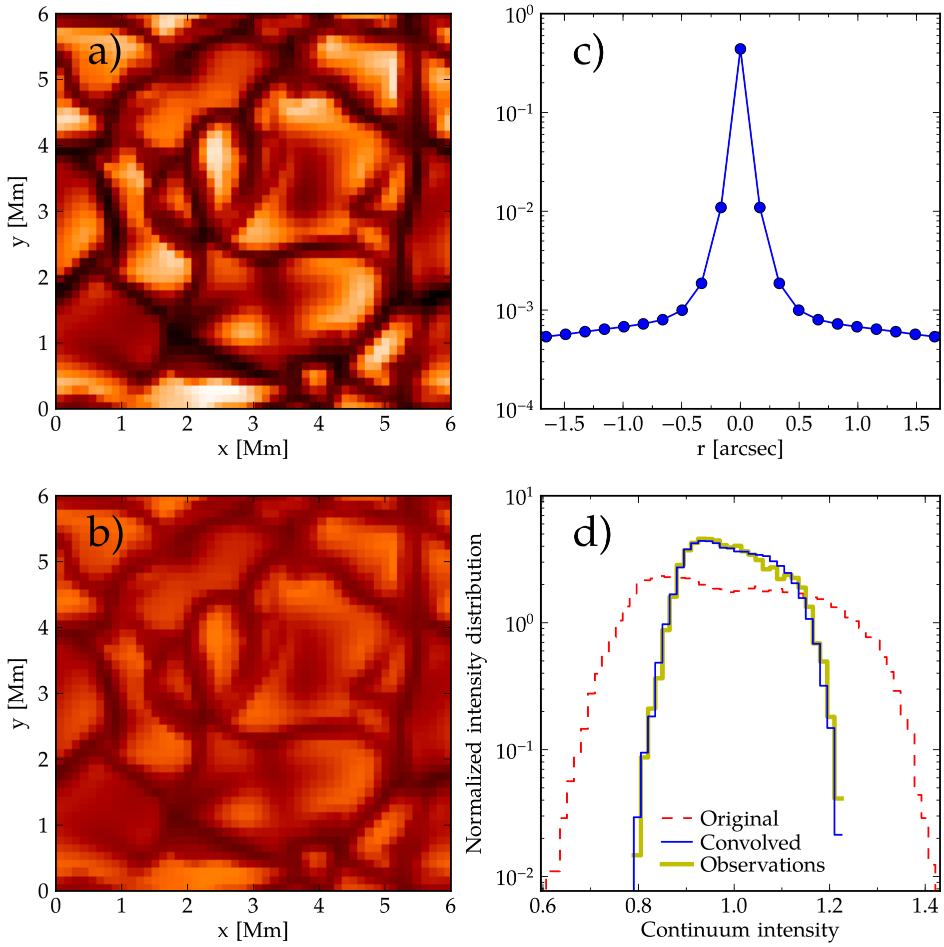

Figure 3.5 Convolution of the simulations with the telescope's and the Earth's atmospheric PSF at the solar disk-centre: a) Continuum intensity at 615 nm for the original simulation; b) Continuum intensity at 615 nm for the convolved simulation; c) The middle row of the 2D PSF used for the convolution (converted from simulation pixels to arcsec and in log scale); d) normalized continuum intensity distribution at 615 nm for the simulations and observations. The convolution parameters *a* and *b* (see text) are chosen so that the continuum intensity distribution and continuum contrast of the simulations match the observations.

telescope, atmospheric scattering, etc. It is reasonable to assume that it will not change significantly between observing sets. The parameter *b*, on the other hand, defines the seeing-induced resolution, which is expected to vary between sets. Hence for the $\mu \neq 1$ sets we use the same *a* value as obtained for disk-centre, and adjust only *b* to obtain the observed continuum contrast.

The simulation used has a horizontal resolution of 50×50. For disk-centre this corresponds to a spatial scale of 6×6 Mm. Because the pixel size of the box is kept constant, when one computes line profiles at $\mu \neq 1$ the spatial resolution will increase with decreasing μ. Different φ angles at off-centre positions will also cause different spatial resolutions along different axes of the simulation box. The two-dimensional PSF is adjusted so that the angular coordinate *r* matches the spatial coordinate in pixels, meaning it has an ellipsoidal profile to account for μ, rotated according to the φ angle.

After convolving the synthetic spectrograms with the PSF, each individual spectrum is

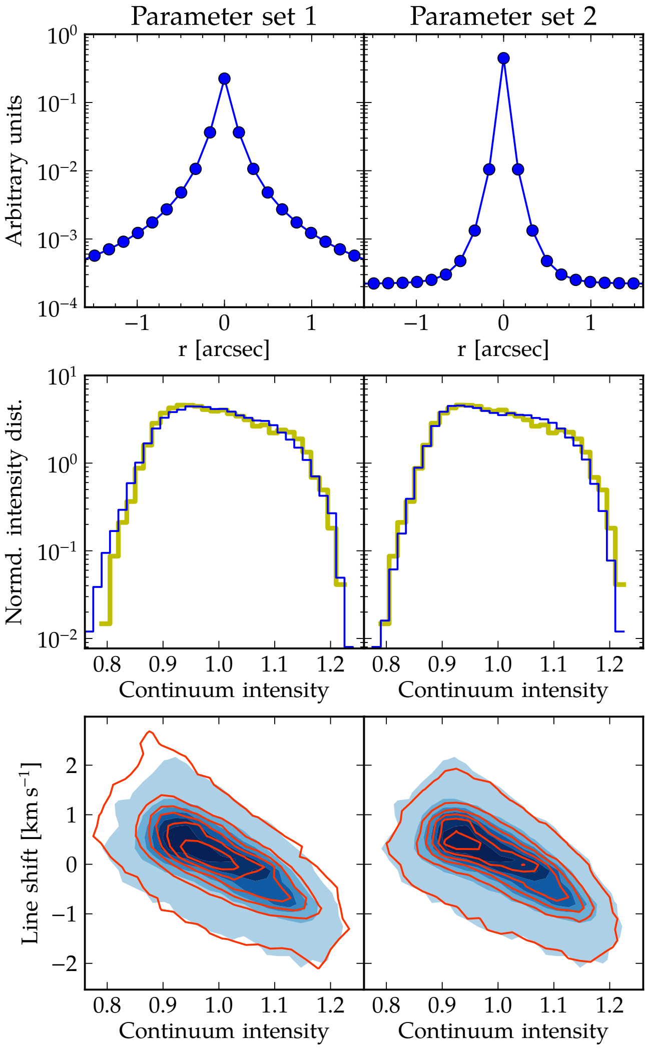

Figure 3.6 Effects of different PSF shapes at 615 nm, $\mu = 1$, using two sets of a and b parameters (left and right columns). *Top panels*: middle row of the 2D PSF. *Middle panels*: continuum intensity distribution for the convolved simulations (thin line) and the observations (thick line). *Bottom panels*: effects of the different convolutions in the line shifts of the strong Fe I 615.77 nm line. Contours represent the point density (see §3.5.1). Solid colour contours are for the convolution with the PSF adopted for our analysis (see Fig. 3.5), line contours for the convolution with the PSF of the corresponding parameter set.

also convolved with the instrumental profile of the spectrograph. A Gaussian equivalent to a resolving power of 200 000 was used. This value of the resolution was obtained by investigating the data and comparing with the FTS intensity atlas.

3.5. Results and discussion

3.5.1. Line shifts

The line shifts are a diagnostic of the velocity fields on the solar surface. Observations at disk-centre probe the vertical motions, while observations closer to the limb can also provide some information about horizontal motions. It should be noted, however, that because line formation takes place at a range of depths it is not possible to associate the observed line shifts with a specific geometric height. The lower contrast of the off-centre data (especially at the limb) means that a precise comparison of the line-of-sight velocities between the different positions on the solar disk is very difficult.

Some results are plotted in Fig. 3.7. The different lines have different formation ranges,

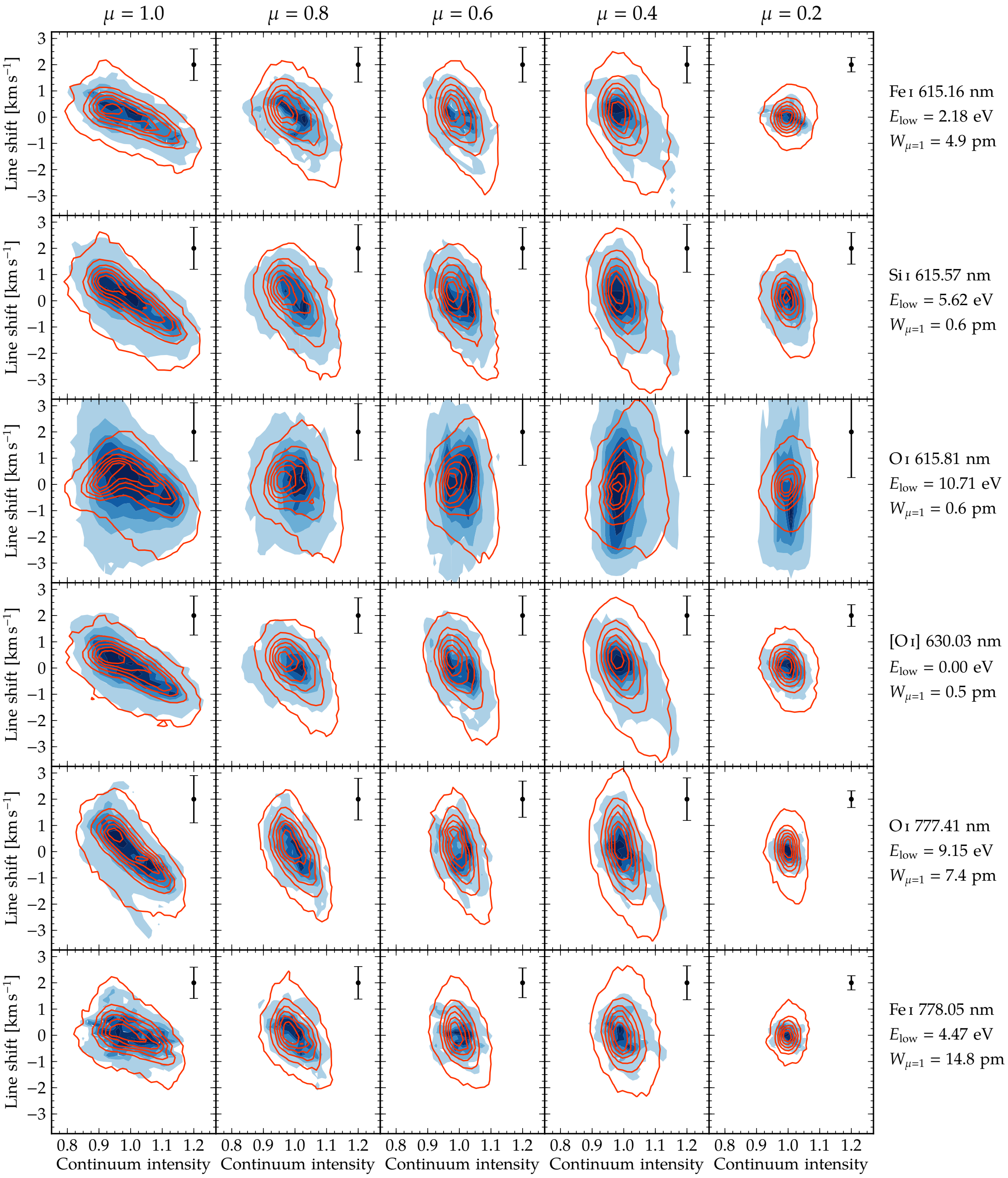

Figure 3.7 Line shifts for selected lines and several μ values. Data shown as contour levels of the two dimensional histogram of the density of points. Observations are depicted as solid colour contours, while the 3D model as line contours. The continuum intensity is normalized to the mean intensity for each μ value. The lower continuum contrast towards the limb is evident, with less structure information at $\mu = 0.2$. The energy of the lower level is shown, along with the disk-centre equivalent width. The chosen lines cover a representative range of lower level energies and equivalent widths. The results for O I 615.81 nm are uncertain due to the line being particularly weak, especially at intergranular regions and at the limb. Results for the other two O I 777 nm triplet lines are similar those shown for O I 7774.1 nm.

and the line shifts give us information about the velocity fields where these lines were formed. For the line shifts as well as most of the other line information, the disk-centre data provide the most detail in the structure as a function of continuum intensity. One can see very clearly the trend with the continuum intensity: the dark (intergranular) regions representing downflows and the bright (granules) regions representing upflows. The agreement with the 3D model is very good, confirming its realistic velocity fields.

The results for other lines are very similar to Fig. 3.7, with generally an excellent agreement between the 3D model and the observations. For some very weak lines with close stronger lines (*e.g.* O I 615.81 nm) our algorithm for determining the line centre can fail more often. This is due to the low S/N ratio and difficulty in finding a very weak line, and results in an increased scatter in the line shifts.

3.5.2. Line strengths

The distribution of the line equivalent widths over the solar granulation is one of the most interesting diagnostics. It provides a wealth of information on how lines are formed over a depth range. From an observational point of view it can be used to 'fingerprint' particular types of species (Kiselman & Asplund, 2003). But more interestingly, it can be used to probe the structure of 3D models and the microphysics of line formation. The early work of Kiselman (1998) is an example of how similar observations can be used to probe for departures from LTE in the 671 nm Li I line. Indeed in §3.5.5 we detail a similar analysis of the NLTE effects of the O I lines using the spatially resolved variation of equivalent widths.

In Fig. 3.8 we show the distribution of equivalent widths for all the lines considered in the present study. The contours reflect the density of points in the plot. Statistically observations and 3D model are comparable, the contours comprising ≈50 000 spatial points, exception made for the O I 777 nm lines, where the contours from the NLTE profiles comprise 25 000 points (only 10 snapshots were used for NLTE calculations).

With a relatively low signal-to-noise ratio for each spatial point, it is not surprising that the observations of weak lines show a bigger scatter than the 3D model. Photon noise influences the equivalent widths directly and also the determination of the continuum level for each spatial point, effects that become more pronounced in weaker lines.

Overall the agreement between the 3D model and the observations is very good. The Si I 615.57 nm line shows a slight mismatch, with the model predicting a weaker line at the bright end. This may be due to blend contamination. In the line profile we have included blends with a nearby strong Si I line and also the Ca I 615.60 nm (because their wings overlap), but the problem persists. In this region the VALD database lists only a very weak Fe I which is unlikely to alleviate the problem either. We note that the Ca I 615.60 nm would display a similar behaviour if we had not included the blend with the O I 615.6 nm line (E_{low} = 10.74 eV). For the Si I it is possible that a similar high-excitation blend might be at play.

For the other lines it is interesting to note the effect of the excitation energy: the O I 777 and 615.82 nm having a high excitation energy and a very pronounced equivalent width variation, while other lines have a more 'C' shaped pattern, becoming increasingly flat

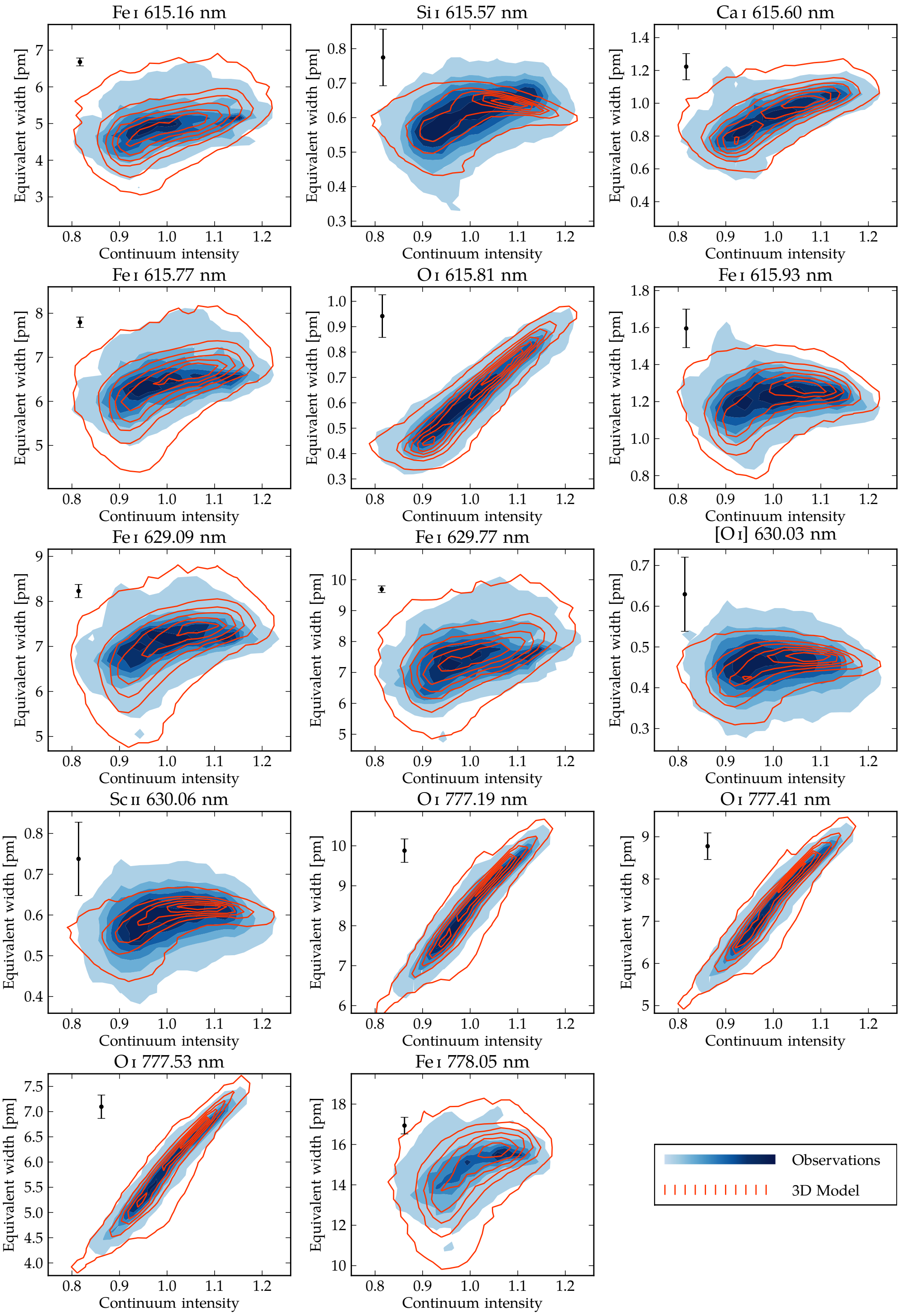

Figure 3.8 Distribution of equivalent widths over the solar granulation at disk-centre. For each spatially-resolved spectrum the equivalent width has been computed and the resulting histogram of points is represented by the contours, as a function of the normalized local continuum intensity. The line profiles of Si I 615.57 nm, Ca I 615.60 nm, O I 615.82 nm and [O I] 630.03 nm include nearby blends (see §3.4.3). All line profiles were computed assuming LTE, except the O I 777 nm lines, showing the NLTE results for $S_\mathrm{H} = 1$.

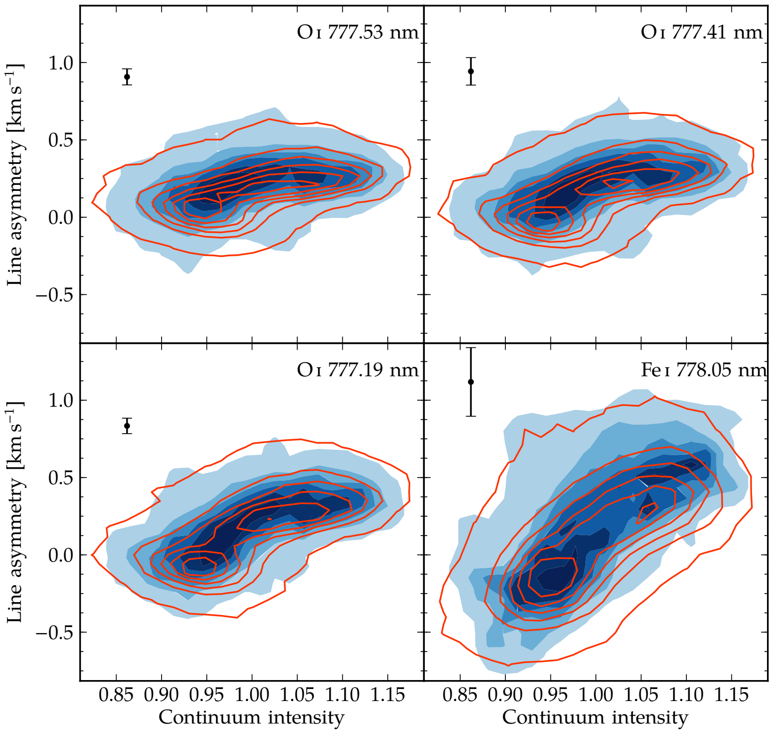

Figure 3.9 Line asymmetries at disk-centre for four of the strongest lines studied: the O I 777 nm triplet and Fe I 778.05 nm. Comparing observations (solid colour contours) with 3D model (line contours). For O I 777 nm showing results from LTE profiles due to higher number of snapshots computed (the asymmetry results are not very sensitive to departures from LTE).

as the excitation energy decreases (*e.g.* [O I]). The variation of the equivalent width distribution with excitation energy is discussed in §3.5.6. For the strong Fe I lines the 3D model seems to predict a slightly steeper variation of equivalent width with continuum intensity at the bright end. This is visible for the Fe I 615.77 nm, 629.09 nm, 629.77 nm and, to a lesser extent, 778.05 nm. The origin of this effect is unclear.

The line profiles were adjusted in abundance so that they match the observed W_{mspec}. This adjustment essentially moves the distribution vertically in Fig. 3.8. Again, it is very reassuring to see how well the 3D model and LTE line formation (except O I 777 nm) describe the observed distributions.

3.5.3. Line asymmetries

The line-asymmetry measure is defined here as the wavelength difference (in velocity units) between the line core and the bisector at half maximum. It is a two-point sampling of the line bisector and, along with the line shift, another probe of the velocity fields. For a given point in the solar granulation, the line asymmetry reflects the velocity distribution over its formation depth and optical path.

In Fig. 3.9 we show the variation of line asymmetry at disk-centre for four medium to strong lines. For weak lines the asymmetry distribution is essentially flat, meaning that the velocity differences along the formation region are small. The O I 777 nm lines provide a great probe for the line asymmetries, because they have essentially the same line parameters except the $\log gf$ value. In Fig. 3.9 we can see how the asymmetry distribution changes from the the weakest line (777.53 nm) to the strongest (777.19 nm). For the weakest line there is almost no variation with continuum intensity, and an

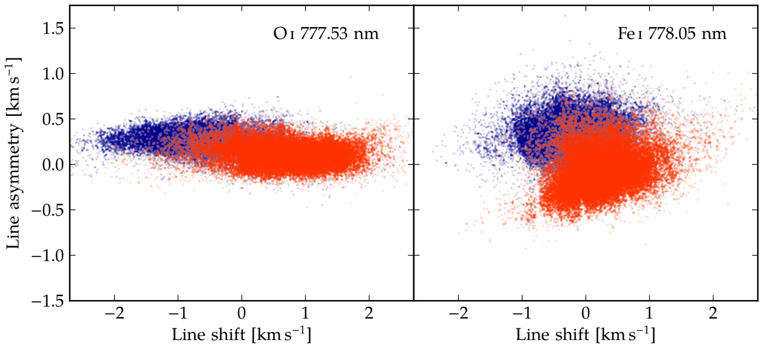

Figure 3.10 Line asymmetries vs. line shifts for the 3D model, LTE, disk-centre and convolved to match the observations. For clarity plotted with points instead of contours. Dark points represent $I_c > \langle I_c \rangle$, light points $I_c < \langle I_c \rangle$.

overall positive asymmetry. This means that the 'bulk' of the line profile is blueshifted in regards to the line core, a result of the vertical velocities in its formation region being mostly positive (outgoing material). As the lines get stronger their formation range will extend outwards. The vertical velocities in higher layers of the photosphere tend to get progressively smaller (with an increase of the horizontal motions as the gas outflows cool down). Formed at higher depths, the stronger lines will cover a larger velocity gradient in the photosphere, and a trend of asymmetry with continuum intensity becomes noticeable. The dark intergranular regions will have a negative asymmetry (the line profile is redshifted in relation to the core) and the brighter regions will have a positive asymmetry (the line profile is blueshifted in relation to the core). These effects are a result of the downflows and upflows of gas at these regions. They become even more apparent in the much stronger Fe I 778.05 nm line, covering a significant velocity gradient and displaying the most extreme values of asymmetry from all lines.

For these four lines as well as most of the other lines (not shown) the 3D model predictions regarding line asymmetry are very good. This is not surprising, given the excellent results reported earlier about the line bisectors (Asplund et al., 2000a). Our results for line asymmetries are consistent with the findings of Kiselman (1994).

In Fig. 3.10 a different perspective is shown. Here the asymmetries of the weakest of the O I 777 nm lines and the strong Fe I line are plotted against the line shifts (measured from the line core in relation to the mean spectrum). The points are colour-coded between dark and bright continuum intensity regions. For the weaker line the average line shift for the bright granules is negative, and positive for intergranular regions. For the strong line granules and intergranular lane regions occupy roughly the same space in line shift, and the overall dispersion in line shifts is smaller. One explanation for this could be that the core of this line is formed above the convective overshoot region. But while the core is formed higher, the asymmetry of the line profiles reflects the motions below, and it becomes very clear that the negative asymmetry is associated with dark regions and positive asymmetry with bright regions. This distinction is hardly visible in the weaker line, formed deeper in the photosphere.

3.5.4. Line FWHM

The distribution of the FWHM with continuum intensity for disk-centre is shown in Fig. 3.11, for four lines. For most of the lines the FWHM decreases with increasing

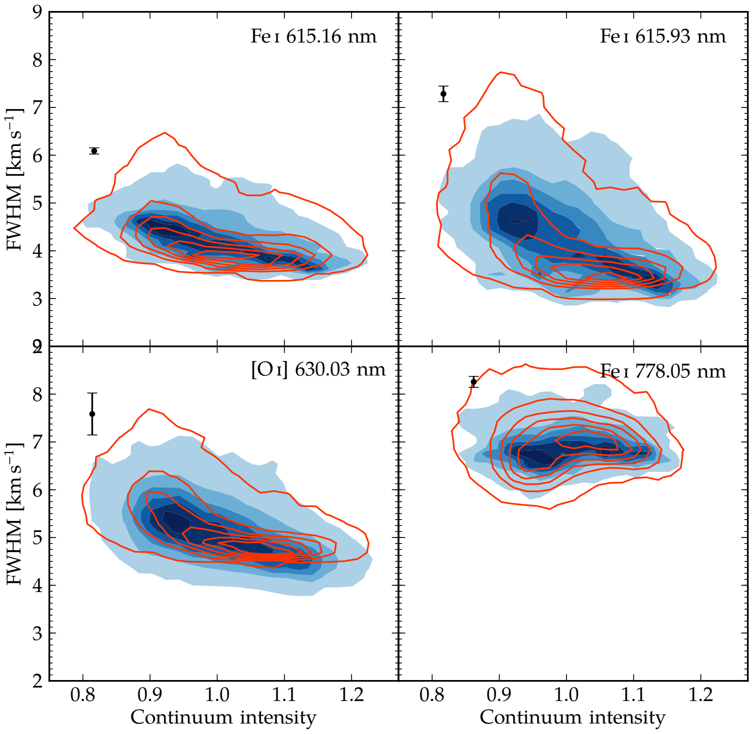

Figure 3.11 Full widths at half maximum (FWHM) at disk-centre for four lines of different strengths and excitation energies. Comparing observations (solid colour contours) with 3D model (line contours).

continuum intensity, with a larger scatter at low continuum intensity. This decreasing behaviour of FWHM with continuum intensity has been observed by others (*e.g.* Hanslmeier et al., 1993; Kiselman, 1994; Puschmann et al., 2003) and is caused by increased line broadening due to turbulence in the intergranular regions. For example, tests with the [O I] 630 nm line show that if the velocity fields are switched off when computing the theoretical profiles, then the predicted FWHM distribution is flat. Very strong lines like Fe I 778.05 nm are formed higher in the atmosphere and above the convective overshoot region, leading to a smaller turbulent broadening and a flatter FWHM distribution, as seen in Fig. 3.11.

The O I 777 nm lines are a special case in the FWHM distribution. Unlike all the other lines considered here, their net variation of FWHM is an increase with the continuum intensity. It can be seen in the bottom panel of Fig. 3.12 for O I 777.41 nm. This effect is related to thermal broadening and results from a peculiar combination of strong lines with a high excitation potential and the relatively light atom of oxygen. With E_{low} = 9.15 eV the O I 777 nm lines are formed very deep where the temperature is higher. A high temperature together with the relatively small atomic weight of oxygen causes the large thermal broadening seen in these lines, which dominates over turbulent broadening. With a steeper temperature gradient in the granules the thermal broadening is larger in the bright regions, driving the FWHM increase with continuum intensity. Tests with fake lines show that the negative slope of the FWHM with continuum intensity can be recovered if the atomic weight is assumed to be much higher than that of oxygen (thereby minimizing thermal broadening), confirming that the FWHM trend is dominated by thermal broadening.

Another candidate for this kind of behaviour is the O I 615.81 nm (E_{low} = 10.74 eV).

However, because this line is much weaker, in absolute terms its thermal broadening will be much smaller, and turbulent broadening dominates. The model predictions (not shown) confirm a decrease of FWHM with the continuum intensity. The inclusion of the molecular blends around this line (see discussion in Chapter 4) will reinforce even more the negative variation of FWHM with continuum intensity. In the observations the uncertainty in its FWHM is very large because the line is very weak, preventing a confrontation with the model predictions.

Overall the 3D model reproduces the observed distributions of FWHMs very well, for both strong and weak lines and including the special case of the O I 777 nm lines.

3.5.5. Departures from LTE in oxygen lines

Of the O I lines the 777 nm triplet lines are known to suffer significant departures from LTE. This was first shown by Altrock (1968) and later explained by Eriksson & Toft (1979). Subsequent studies (*e.g.* Kiselman, 1991) also found NLTE effects for the O I 615.81 nm line, albeit on a much smaller scale – usually $\lesssim 0.03$ dex (Asplund et al. 2004; Caffau et al. 2008a; Chapter 4).

A proper NLTE treatment of these lines poses several challenges. As noted in previous studies, one of the main problems is to account for the effect of collisions with neutral hydrogen. No laboratory data or quantum mechanical calculations are available to date. The best estimate to account for the efficiency of hydrogen collisions has been to use the recipe of Steenbock & Holweger (1984), a generalization of the classical Drawin formula (Drawin, 1968). This recipe is often scaled by an empirical factor S_{H}. In the work of Allende Prieto et al. (2004) and Chapter 4 the centre-to-limb variations of the O I 777 nm lines have been used to derive the best-fitting S_{H} value.

We propose to use the line variations across the solar granulation at disk-centre to test the LTE and NLTE line formation and derive the best fitting empirical S_{H} value. The inherent scatter of the spatially-resolved line quantities makes this method less sensitive or constraining than the centre-to-limb variations. Nevertheless, it provides an independent test of the possible S_{H} values.

We have used the same LTE and NLTE calculations as in Chapter 4, detailed in §3.4.2. Due to computational constraints the full 3D NLTE line formation was only performed for 10 snapshots of the 3D simulation. The NLTE effects in O I 615.81 nm are so small that the distributions of line quantities in NLTE are essentially indistinguishable from LTE. Hence we limit our NLTE analysis to the 777 nm triplet only. The line profiles for different values of S_{H} have all been interpolated in abundance so that the equivalent width of the spatially and temporally averaged spectrum matches the observed.

In Fig. 3.12 we show how the line equivalent widths and the FWHM vary across the solar granulation at disk-centre, for the observations and the 3D model with different S_{H} values for hydrogen collisions. The results shown are for the O I 777.41 nm line, but they are very similar for the other two lines.

The equivalent width plot is perhaps the most interesting. The model results can be divided in two regions: granules and intergranular regions, with a smaller point density in the middle, where $I_{\mathrm{c}} = \langle I_{\mathrm{c}} \rangle$. The hydrogen collisions have different effects

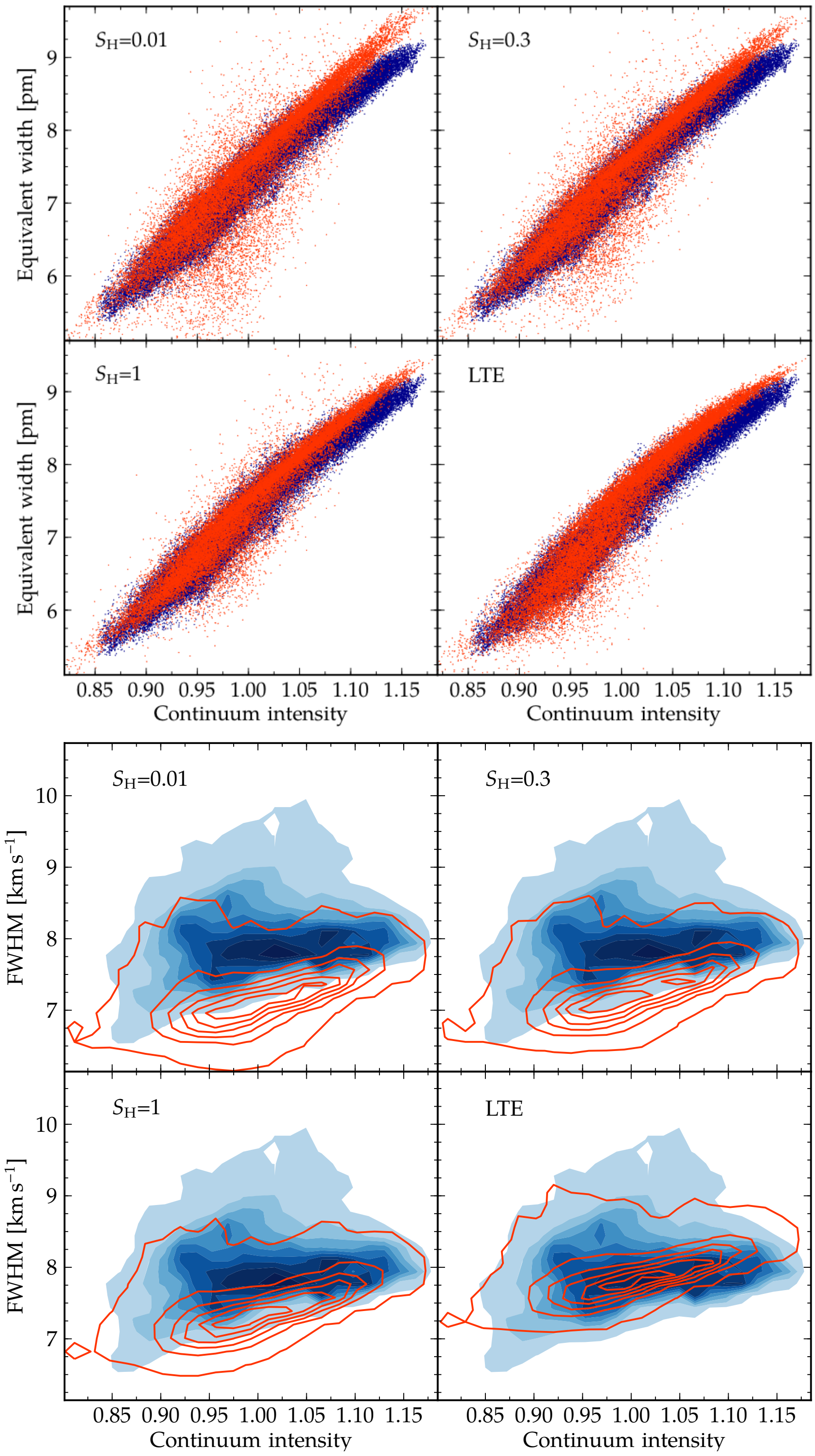

Figure 3.12 *Top:* equivalent widths of the O I 777.41 nm line as a function of continuum intensity. For clarity the values are shown as points, instead of contours. *Bottom:* FWHM for the same line as a function of continuum intensity. Comparing the disk-centre observations (dark points in equivalent width; solid color contours in FWHM) with the 3D model (light points in equivalent width, line contours in FWHM), for LTE and NLTE, for different values of S_H. The oxygen abundance has been adjusted in each case to fit the observed mean disk-centre equivalent width.

on each region. An increase in S_{H} makes the equivalent width slope less steep in the intergranular regions, but steeper in the granular regions. In the LTE case it can be seen that in the intergranular regions the equivalent width slope is steeper than in the observations. In such regions the agreement with the observations improves for the NLTE models. On the other hand, as S_{H} decreases the equivalent width slope in the bright regions gets steeper, departing from the observed values. No single value of S_{H} can be in perfect agreement with the observations in both high and low intensity regions.

Another aspect worth noting is the scatter, especially in the dark regions. For $S_{\mathrm{H}} = 0.01$ one can see that the 3D model displays a significant amount of scatter at low continuum intensity. This does not seem to be consistent with the observations. As S_{H} increases the amount of scatter decreases. This increase of scatter in NLTE is the opposite behaviour of the Li I 671 nm line: for this line there is a much bigger scatter for the LTE profiles (Kiselman, 1998; Asplund, 2005). Because the temperature dependence of the O I 777 nm lines is the opposite of Li I 671 nm, the opposite scatter results are perhaps not surprising. The increased scatter for low S_{H} is likely a reflection of the high temperature sensitivity of the lines. The NLTE effects make the lines stronger, and the lower S_{H}, the stronger the lines. This strengthening will increase the temperature sensitivity of the lines, which may explain the larger scatter for lower S_{H}. If one makes the reasonable assumption that the 3D model realistically describes dark and bright granulation regions, then the scatter in equivalent width is enough to rule out the $S_{\mathrm{H}} \lesssim 0.3$ profiles, when comparing with the observations. Overall, accounting for the scatter and equivalent width slopes in dark and bright regions, $S_{\mathrm{H}} = 1$ seems to be the value that best reproduces the observations. However, it should be noted that for $1 \leq S_{\mathrm{H}} \leq 3$ there is not much difference in the results.

In the lower panel of Fig. 3.12 we show a similar figure but for the FWHM. The area occupied by the observations's contours is larger probably due to a better statistical sample. Disregarding the line strength, the lower the S_{H}, the narrower and deeper the NLTE line profile shapes will be when compared with LTE. Thus a decreasing S_{H} will drive down the FWHM. This is visible in Fig. 3.12. The LTE FWHM's provide the best match for the observations. The NLTE profiles, even for $S_{\mathrm{H}} = 1$ are narrower. This effect is also seen in the disk-centre profile fits of Chapter 4, and its cause is unclear. As in the equivalent width figure, lower S_{H} show a larger scatter in FWHM. However in this case the scatter cannot be used to exclude a particular S_{H} because the FWHM is always lower than the observations.

3.5.6. Summary quantities of line variations

Definitions

In this section we look at the variation of the line quantities at high spatial resolution and at several μ values. It is not easy to quantify with a few numbers the quantity distributions like in Figs. 3.7 and 3.8, but it must be done for achieving insight. There are many possible correlations between the different line quantities that can be established.

We follow the approach of Kiselman (1994) and define the two quantities:

$$\alpha = \frac{\mathrm{d}I_{\text{line core}}}{\mathrm{d}I_{\mathrm{c}}}, \tag{3.9}$$

$$\gamma = \frac{\langle I_{\mathrm{c}} \rangle}{\langle W \rangle} \cdot \frac{\mathrm{d}W}{\mathrm{d}I_{\mathrm{c}}}, \tag{3.10}$$

where $I_{\text{line core}}$ is the absolute intensity of the line core, W the equivalent width and I_{c} the continuum intensity. Both parameters are obtained by least-squares polynomial fits to the data. In the case of α a line is fitted, while for γ a parabola is fitted. Exceptions to this are the O I 777 nm lines at $\mu = 1$ and $\mu = 0.8$. Because their equivalent width variations at these positions are not easily described by a parabola, 5th order polynomials are fitted instead.

The α parameter is a measure of the variation of the absolute line core intensity with the local continuum intensity. If $\alpha = 1$ then the line cores follow the continuum variations (expected for weak lines). Lower values of α are expected as the lines get stronger. This parameter is plotted vs. the equivalent width of each line (measured from the spatial mean spectrum at each μ).

The γ parameter describes the variation of equivalent width with the local continuum intensity. It is divided by the mean equivalent width to put all lines in the same scale. To better describe the equivalent width distribution, the derivative $\mathrm{d}W/\mathrm{d}I_{\mathrm{c}}$ is evaluated at two points: in the dark (intergranular) regions and in the bright (granular) regions. These points are defined as the mean continuum intensity of all points where $I < \langle I_{\mathrm{c}} \rangle$ and $I > \langle I_{\mathrm{c}} \rangle$, respectively. Hence two values of γ are defined: γ_{dark} and γ_{bright}.

Results

The results for α are plotted in Fig. 3.13 and for γ in Fig. 3.14. It should be noted that these quantities are subject to several uncertainties (particularly γ). The most important source of uncertainty is the scatter in the quantities and the approximation of using a line or parabola to fit these quantities. For the 3D models the particulars of the image degradation (see §3.4.4) also influence these quantities, albeit to a lesser extent. The elemental abundances have been adjusted so that the model $W_{\mu=1}$ match the observations. The $\mu = 1$ abundances are used for all the other μ positions. For the O I 777 nm lines the NLTE profiles with $S_{\mathrm{H}} = 1$ were used.

The α results at $\mu = 1$ are consistent with the findings of Kiselman (1994). The lack of lines with W in the 1-5 pm region prevents a clear picture in the variation of α with equivalent width, but from the weaker lines a downward linear trend is visible. This goes on to a plateau for the stronger lines, where α is close to zero or negative. A negative correlation of the line core intensity with I_{c} for strong lines has been documented in the literature (*e.g.* Balthasar et al., 1990; Hanslmeier et al., 1990; Kučera et al., 1995; Puschmann et al., 2003). It is believed to be associated with convective overshooting: in higher layers the gas is cooler above granules than above the integranular lanes. This translates into an inverse granulation pattern, and causes the negative correlation between core intensity and I_{c}. The model results indicate a slightly lower α for some of the stronger lines, which may indicate an higher convective overshooting than observed.

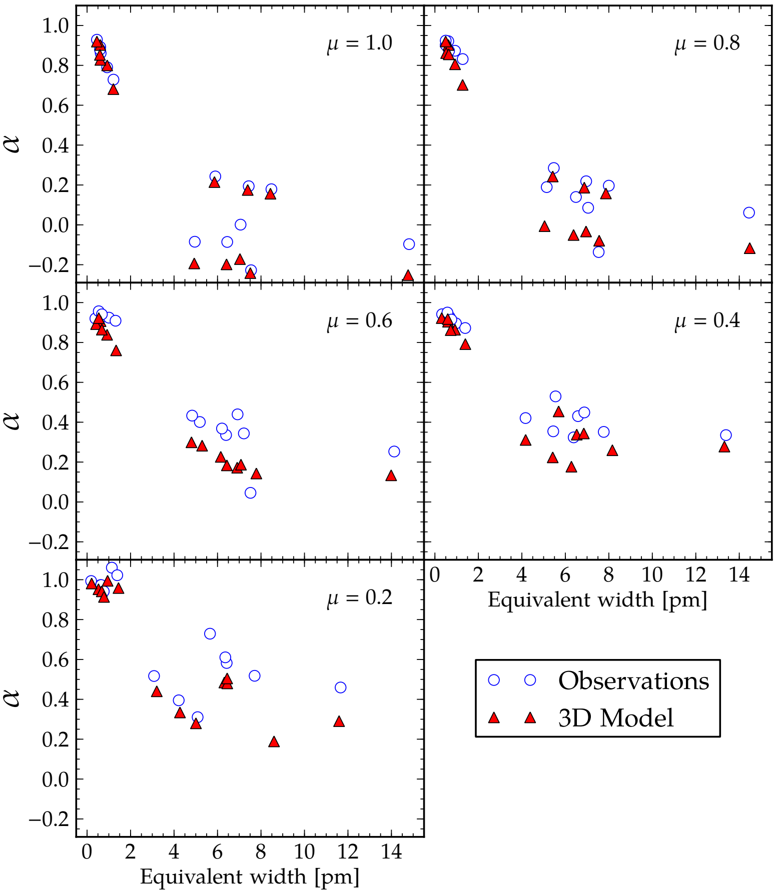

Figure 3.13 Variation of the α parameter (describing variation of line core intensity, see text) with the mean equivalent width at each μ, for all lines. The elemental abundances are adjusted so the model equivalent widths at $\mu = 1$ match the observed. For $\mu \neq 1$ the disk-centre abundances are used, meaning that the model equivalent widths depart from the observed in some cases.

For $\mu \neq 1$, α of the strong lines increases. Tests with the 3D model at $\mu = 1$ and varying degrees of atmospheric degradation show that this effect (and also a less steep dependence of α with W) is mostly due to a reduction in continuum contrast. Overall the model agrees reasonably well with the observations. The stronger lines are more problematic, especially at the limb where the predicted equivalent widths differ from the observations.

The parameter γ measures how the line strength varies with the continuum intensity. At $\mu = 1$ we find both γ_{dark} and γ_{bright} to have a monotonic increase with the excitation potential of the lines. This is in agreement with Kiselman (1994), although he finds a more clear relation by employing a filter to remove the effects of solar oscillations. As discussed by Kiselman (1994) this trend is an indication of the higher temperature sensitivity of lines with higher excitation potentials. A positive γ at $\mu = 1$ is in agreement with the positive correlation between W and I_{c} found in other studies (Hanslmeier et al., 1990; Puschmann et al., 2003).

The variation of γ between dark and bright regions is small but measurable. For most lines $\gamma_{\mathrm{dark}} > \gamma_{\mathrm{bright}}$, indicating a steeper variation of W with I_{c}. The decrease in intensity

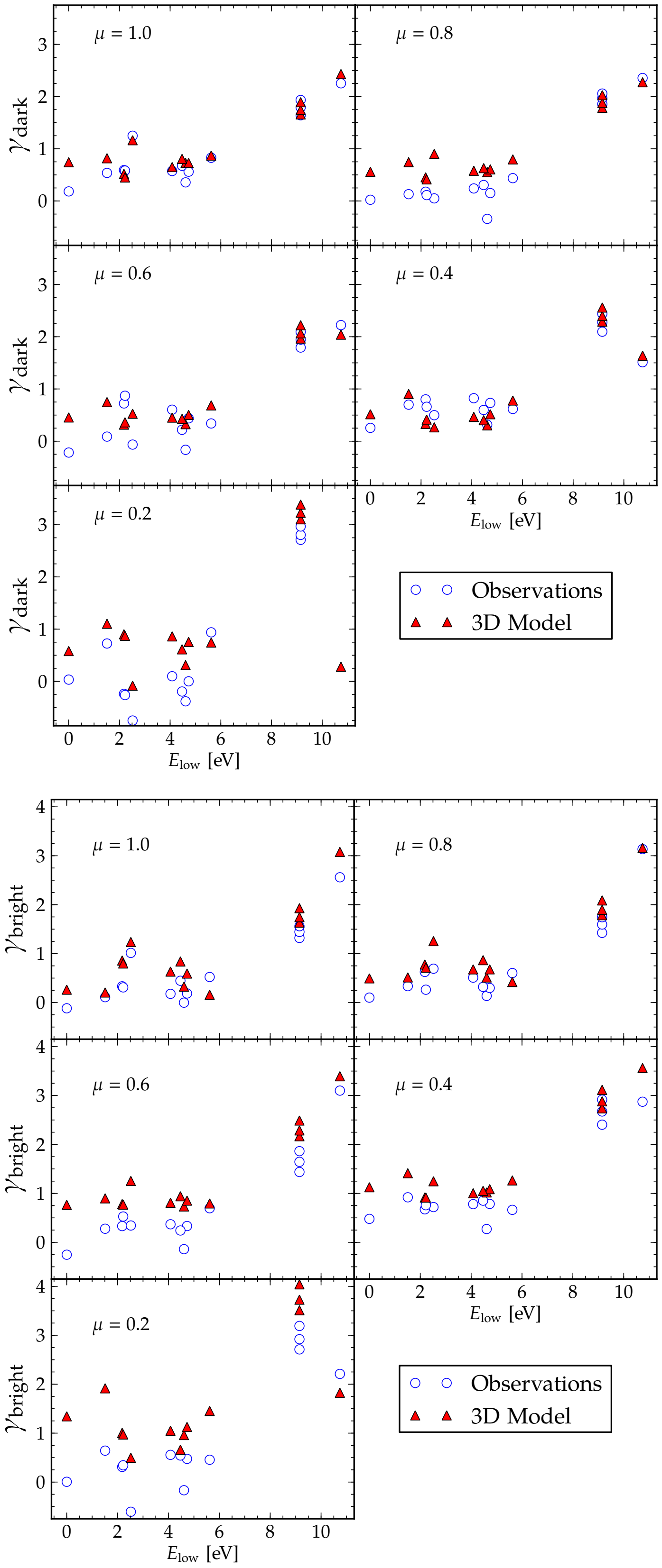

Figure 3.14 Variation of the γ parameter (describing the variation of equivalent width, see text) with the excitation potential for all lines, at the different μ. The parameter is evaluated for dark (*top panel*) and bright regions (*bottom panel*).

contrast towards the limb (*e.g.*, Fig. 3.7) makes the determination of γ more problematic – the uncertainty from fitting polynomials increases. Yet the agreement with the model is good for most lines and μ positions. It is interesting to note the agreement between model and observations is better for $\gamma_{\rm dark}$ than $\gamma_{\rm bright}$. The model predicts a steeper variation of W with $I_{\rm c}$ when $I_{\rm c} < \langle I_{\rm c} \rangle$. For the O I 777 nm lines this is visible in Fig. 3.12, where for LTE and different NLTE recipes, the model variation of W in bright regions is always steeper than the observations. A higher $\gamma_{\rm bright}$ in the models when compared with the observations is more apparent for $\mu \lesssim 0.6$.

3.6. Conclusions

We have obtained high-spatial-resolution observations of lines of neutral oxygen and other species in quiet solar granulation at different positions on the solar disk. These have been used to test the 3D photosphere models and line formation. At the solar disk-centre the predicted distributions of line strengths, shifts and shapes are for most lines in excellent agreement with the observed. Both for the oxygen lines and most of the other lines. At different viewing angles a quantitative study of the line properties is more difficult because of a smaller contrast between granules and intergranular regions. Nevertheless, fits to the variation of line strengths and other quantities over the granulation show an encouraging good agreement with the observations.

For the O I 777 nm lines we employ the high-spatial-resolution observations at disk-centre to constrain the NLTE physics. Although not as robust as the centre-to-limb variation (Allende Prieto et al. 2004; Chapter 4), this test provides another approach to empirically constrain the efficiency of collisions with neutral hydrogen, $S_{\rm H}$. We find that $S_{\rm H} = 1$ describes most observables well, in agreement with the results of Chapter 4. Also in agreement with Chapter 4 we find that NLTE profiles for $\mu = 1$ are narrower than the observations, which agree better with the higher $S_{\rm H}$ profiles. Furthermore, it is difficult for any $S_{\rm H}$ to describe the variation in equivalent width with continuum intensity in the intergranular regions and granules at the same time. These discrepancies may be linked to the crude approximation of using scaled classical formulæ to estimate the collisions with hydrogen. The discrepancies may indicate a more complex dependence of these collisions with temperature and/or pressure. Moreover, $S_{\rm H}$ will also likely vary between transitions.

Regarding the weak O I 615.81 nm line, its NLTE effects are very small and not noticeable in the variation of the line properties over the granulation.

For the spectral lines investigated here, the agreement between the 3D model and the observations for the line velocities, shapes and strengths is excellent, both for disk-centre and different viewing angles. It places the 3D model on a solid footing regarding oxygen and provides compelling evidence on its suitability for abundance analysis.

CHAPTER 4

Centre-to-limb variation of solar oxygen lines

T. M. D. Pereira, M. Asplund, D. Kiselman, *A&A in press*

Abstract

Context: There is a lively debate about the solar oxygen abundance and the role of 3D models in its recent downward revision. These models have been tested using high-resolution solar atlases of flux and disk-centre intensity. Further testing can be done using centre-to-limb variations.

Aims: Using high-resolution and high S/N observations of neutral oxygen lines across the solar surface, we seek to test that the 3D and 1D models reproduce their observed centre-to-limb variation. In particular we seek to assess whether the latest generation of 3D hydrodynamical solar model atmospheres and NLTE line formation calculations are appropriate to derive the solar oxygen abundance.

Methods: We use our recent observations of O I 777 nm, O I 615.81 nm, [O I] 630.03 nm, and nine lines of other elements for five viewing angles $0.2 \leq \mu \leq 1$ of the quiet solar disk. We compared them with the predicted line profiles from the 3D and 1D models computed with the most up-to-date line formation codes and line data and allowing for departures of LTE. The centre-to-limb variation of the O I 777 nm lines is also used to obtain an empirical correction for the poorly known efficiency of the inelastic collisions with H I.

Results: The 3D model generally reproduces the centre-to-limb observations of the lines very well, particularly the oxygen lines. From the O I 777 nm lines we find that the classical Drawin recipe slightly overestimates H I collisions ($S_{\mathrm{H}} \approx 0.85$ agrees best with the observations). The limb observations of the O I 615.82 nm line allow us to identify a previously unknown contribution of molecules for this line, prevalent at the solar limb. A detailed treatment of the [O I] 630.03 nm line that includes the recent nickel abundance shows that the 3D modelling closely agrees with the observations. The derived oxygen

abundances with the 3D model are 8.68 (777 nm lines), 8.66 (630.03 nm line), and 8.62 (615.82 nm line).

Conclusions: These additional tests have reinforced the trustworthiness of the 3D model and line formation for abundance analyses.

4.1. Introduction

Oxygen is arguably one of the most important elements in the Universe. After hydrogen and helium it is the most common element, projecting its importance to many fields in astrophysics: from stellar abundances to the interstellar medium and galactic evolution. The solar oxygen abundance is often used as a reference in many studies. As a volatile element, its meteoritic abundance is not representative, so the most reliable probe for the reference oxygen abundance is the solar photosphere.

With high-quality data readily available, a longstanding expertise in solar observations and much improved knowledge of stellar atmospheres in the past decades would lead one to expect that a measurement as fundamental as the solar photospheric abundance of oxygen would be firmly established; on the contrary, the solar oxygen abundance has been hotly debated in recent times. From the high (and widely used) value of $\log \epsilon_{\mathrm{O}} = 8.93 \pm 0.04$ (Anders & Grevesse, 1989), the proposed oxygen abundance has been revised downward to the low value of $\log \epsilon_{\mathrm{O}} = 8.66 \pm 0.05$ (Asplund et al., 2004). The pivotal causes for this change have been proper treatment of the statistical inhomogeneities caused by the solar granulation (making use of a 3D photosphere model), the proper treatment of departures from local thermodynamical equilibrium (LTE), and improved line data (including better blend identification). A low oxygen abundance has caused significant grievances among the solar/stellar interior modelling community by undoing the almost perfect agreement between the solar interior models and helioseismology, which has sparked much debate. In past years the downward revision of the solar oxygen has been supported by some studies (*e.g.* Socas-Navarro & Norton, 2007b; Meléndez & Asplund, 2008) but contested by others (*e.g.* Centeno & Socas-Navarro, 2008; Ayres, 2008). Some recent studies find intermediate oxygen abundances (*e.g.* Caffau et al., 2008a). Centeno & Socas-Navarro (2008) claim a model-independent determination of the oxygen abundance, which is dismissed by Scott et al. (2009).

A measure of the photospheric oxygen abundance is made difficult for several reasons. Of the few atomic oxygen lines available in the solar spectrum, some are very weak, others significantly blended. An example is the popular [O I] 630.03 nm line, which is weak and has a non-negligible blend with a nickel line. On the other hand, departures from LTE are also important for some O I lines – the O I 777 nm triplet lines being the typical example. These lines are known to show significant departures from LTE, requiring the use of detailed NLTE line formation that requires detailed atomic input data that may not exist.

For the NLTE modelling the collisions with neutral hydrogen are particularly relevant. There is disagreement in the literature regarding the importance of inelastic collisions with H I. At this point, the lack of experimental data or quantum mechanical calculations makes its estimation complicated. A customary approach is to adopt a generalization of the classical Drawin formula (Drawin, 1968), using the recipe of Steenbock & Holweger (1984), often scaled by an empirical factor S_{H}, and Lambert (1993) corrected a mistake in these original formulæ. However, there are different views regarding which scaling factor to use for oxygen. Nissen et al. (2002) and Asplund et al. (2004) chose $S_{\mathrm{H}} = 0$, based on evidence that the Drawin formula overestimates the H I collision efficiency with some atoms for which experimental or detailed quantum mechanical data exists (*e.g.* Barklem et al., 2003). Caffau et al. (2008a), on the other hand, have adopted a seemingly *ad-hoc* value of $S_{\mathrm{H}} = 1/3$.

For the solar O I 777 nm lines, the adopted recipe for H I collisions has a significant effect on the line shape and strength and consequently, on the derived oxygen abundance. Using the same 3D model of Asplund et al. (2004), Allende Prieto et al. (2004) empirically found that $S_{\mathrm{H}} = 1$ agree somewhat better than $S_{\mathrm{H}} = 0$, while the LTE case can be ruled out.

In addition to the line formation physics, the centre-to-limb variation of the lines provides a robust test of the model atmospheres by probing the depth variation of the source functions, as seen from the Eddington-Barbier approximation. In this work we study atomic oxygen lines using observations of their centre-to-limb variation. We study the effects of using different atmospheric models, allow departures from LTE in the line formation, and properly account for blends. Our aim is to provide additional observational tests of some of the models used to infer the oxygen abundance, using new solar observations.

We obtained high spatial and spectral resolution observations of oxygen and other lines across the solar surface. Similar observations of oxygen lines have been obtained in the past (notably Müller et al., 1968; Altrock, 1968; Allende Prieto et al., 2004). However, available data from early works is limited to equivalent widths, and the more recent work of Allende Prieto et al. (2004) covers only the O I 777 nm triplet lines. Furthermore, the long slit used by Allende Prieto et al. (2004) increases the uncertainty of the μ value for their limb data. The observations outlined in the present work include five neutral oxygen lines: the O I 615.81 nm, [O I] 630.03 nm, and the three O I 777 nm over five positions in the solar disk. In addition, lines from other elements are also included in the observed spectral regions.

Our observations are briefly outlined in the next section. In §4.3 we outline the model atmospheres and the line formation codes used, which are compared with the observations in §4.4. Conclusions are made in §4.5.

4.2. Observations

4.2.1. Overview

We make use of the observations of Chapter 3, which we refer to for a detailed description of the programme, instruments, and reduction. Chapter 3 focused on high spatial resolution, and here we study the centre-to-limb variations of the spatial and temporaly mean spectra. Thus, in terms of the observations, the main difference is that we average the spectrograms in space and time to obtain a mean spectrum for each position in the solar disk.

Using 25 spectrograms for each $\mu \neq 1$ position and 50 spectrograms for $\mu = 1$ means that our mean spectra comprise an average of more than 20 000 spectra (> 40 000 for disk-centre). The S/N for the spectrum of one spatially averaged spectrogram is about 700. The total S/N would be $\sqrt{25}$ times that value, if the images were all independent, which is not the case because the time separation does not always guarantee that they sample a different granulation pattern. In any case, a conservative estimate of the S/N should be at least 1500 – more than enough for the present analysis. Unlike in Chapter 3, no Fourier filtering is applied, since most of the photon noise is eliminated by the averaging of many spectra.

It is worth noting that, for the $\mu \approx 0.4$ set, some facular features were visible on the slit-jaw images, though the slit did not cross them. Because we want to study quiet regions and to avoid any possible interference due to magnetic fields, we have removed the middle third of the spectral images for the $\mu \approx 0.4$ set, so that the final spectrum was averaged only from quiet regions. This procedure reduces the S/N for this set by about 20%.

After obtaining the spatial and temporally averaged spectra for each μ, the continuum levels are found manually. In some cases such as the O I 615.81 nm line, a local continuum is used to compensate for blends not included in the line synthesis. The wavelength calibration, explained in Chapter 3, is linked to the Fourier transform spectrograph (FTS) disk-centre intensity atlas of Brault & Neckel (1987). It consists in identifying the same spectral lines in the FTS atlas and our observations, and then obtaining the dispersion relation by a polynomial fit to the line cores. It lacks precision, and a more precise wavelength calibration is necessary for analysing some lines. In the analysis section we outline a correction to the wavelength calibration using the atmosphere models and Fe I lines. The reduced spectra for disk-centre and the limb can be found in Fig. 4.1.

4.2.2. Comparison with previous studies

The oxygen lines we observed have been the object of several studies in the past. Most notably, the centre-to-limb variation of these lines has been studied in Müller et al. (1968), Altrock (1968), and Allende Prieto et al. (2004). The last work only covers the 777 nm triplet lines. These works use different instrumentation and techniques, which makes them fairly independent of our observations. We compare the equivalent widths of the present work with the ones from these studies in Fig. 4.2. Equivalent width measurements have a somewhat subjective component due to different normalizations and different wavelength ranges where it is computed. However, it is the only comparison that can be made at least with Müller et al. (1968) and Altrock (1968). With Allende Prieto et al. (2004), we used the available online spectra and computed the equivalent widths in the same way as for our data (direct integration, same wavelength range). It should be noted that their normalization around the 777.41 and 777.53 nm lines is slightly different from ours, leading to a higher continuum level. This in turn makes the lines stronger when computing the equivalent widths by direct integration. The equivalent widths as a function of μ for all the lines included in this work are listed

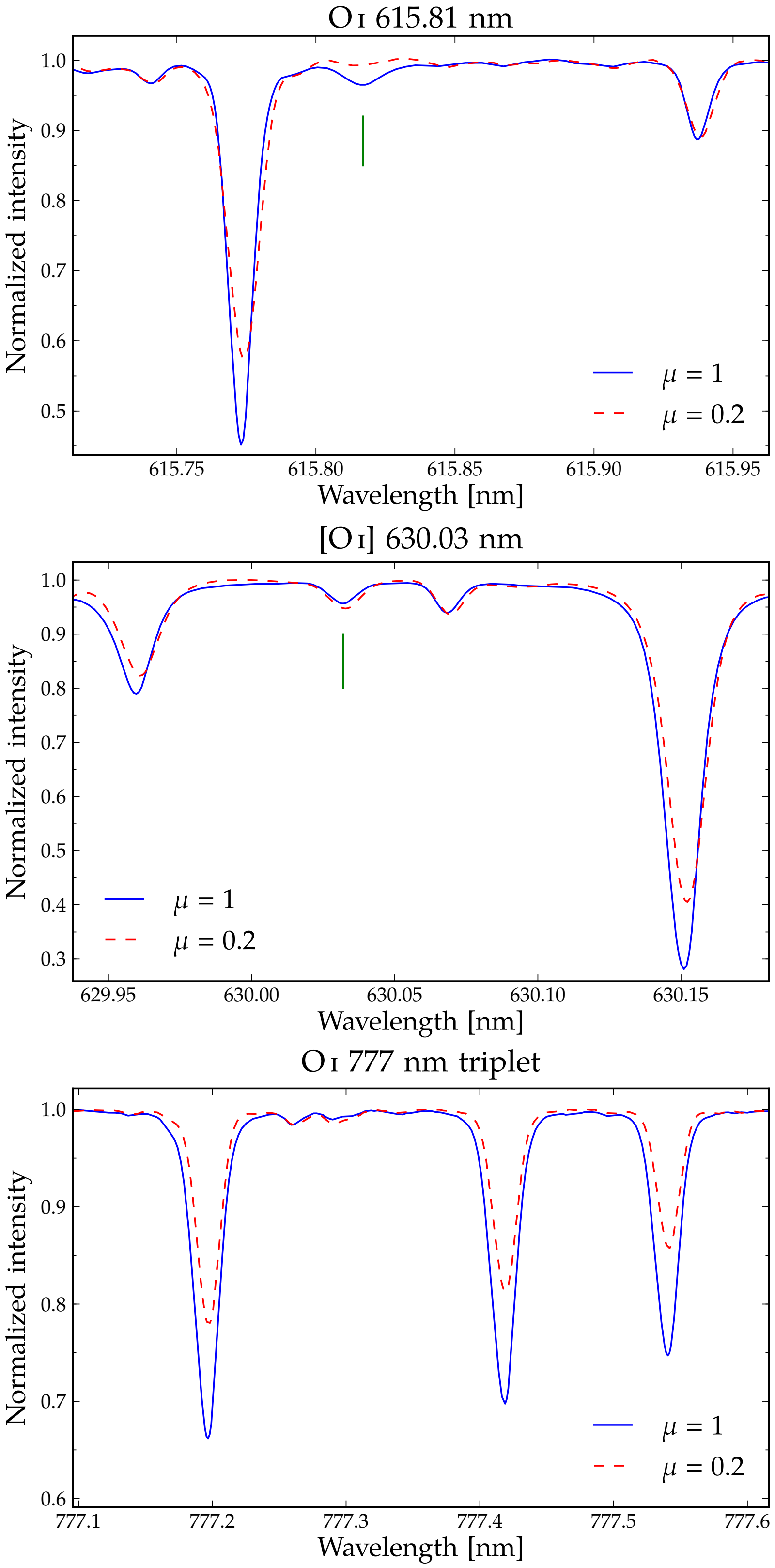

Figure 4.1 Observed profiles at disk-centre and limb. For the weak 615.81 and 630.03 nm lines the location is indicated. In this figure the wavelengths for the limb spectra have been adjusted to compensate for solar rotation and other systematics.

in Table 4.1. The uncertainties arise mostly from the continuum placement. For the lines in the 777 nm region, the errors are larger because a larger integration region was used. The smooth variation of the equivalent widths with μ in our data indicates a low statistical error and highlights its high quality.

Table 4.1 Equivalent widths for the lines included in this analysis, as a function of μ.

Line		W [pm]				
Species	λ [nm]	$\mu = 0.999$ ± 0.001	$\mu = 0.793$ ± 0.012	$\mu = 0.608$ ± 0.018	$\mu = 0.424$ ± 0.024	$\mu = 0.197$ ± 0.003
Fe I	615.1618	4.95 ± 0.04	5.14 ± 0.04	5.19 ± 0.04	5.55 ± 0.04	5.65 ± 0.04
Si I	615.5693	0.61 ± 0.03	0.62 ± 0.03	0.68 ± 0.03	0.67 ± 0.03	0.62 ± 0.03
Ca I	615.6023	0.92 ± 0.03	0.92 ± 0.03	1.01 ± 0.08	0.97 ± 0.08	1.14 ± 0.03
Fe I	615.7728	6.45 ± 0.04	6.49 ± 0.04	6.39 ± 0.05	6.58 ± 0.16	6.42 ± 0.04
O I	615.8186	0.63 ± 0.03	0.50 ± 0.03	0.38 ± 0.06	0.33 ± 0.03	0.19 ± 0.03
Fe I	615.9378	1.21 ± 0.04	1.28 ± 0.07	1.31 ± 0.06	1.39 ± 0.11	1.39 ± 0.04
Fe I	629.0965	7.06 ± 0.05	7.05 ± 0.05	6.92 ± 0.05	6.87 ± 0.15	6.36 ± 0.05
Fe I	629.7793	7.54 ± 0.04	7.53 ± 0.04	7.52 ± 0.15	7.77 ± 0.04	7.71 ± 0.04
[O I]	630.0304	0.45 ± 0.04	0.50 ± 0.04	0.54 ± 0.04	0.58 ± 0.04	0.65 ± 0.04
Sc II	630.0698	0.59 ± 0.03	0.65 ± 0.03	0.68 ± 0.03	0.76 ± 0.03	0.77 ± 0.03
O I	777.1941	8.48 ± 0.09	8.00 ± 0.14	7.21 ± 0.09	6.38 ± 0.10	5.09 ± 0.10
O I	777.4166	7.44 ± 0.09	6.96 ± 0.15	6.21 ± 0.09	5.44 ± 0.10	4.22 ± 0.33
O I	777.5390	5.90 ± 0.09	5.47 ± 0.11	4.83 ± 0.09	4.17 ± 0.10	3.08 ± 0.28
Fe I	778.0557	14.81 ± 0.14	14.45 ± 0.14	14.13 ± 0.14	13.39 ± 0.14	11.66 ± 0.14

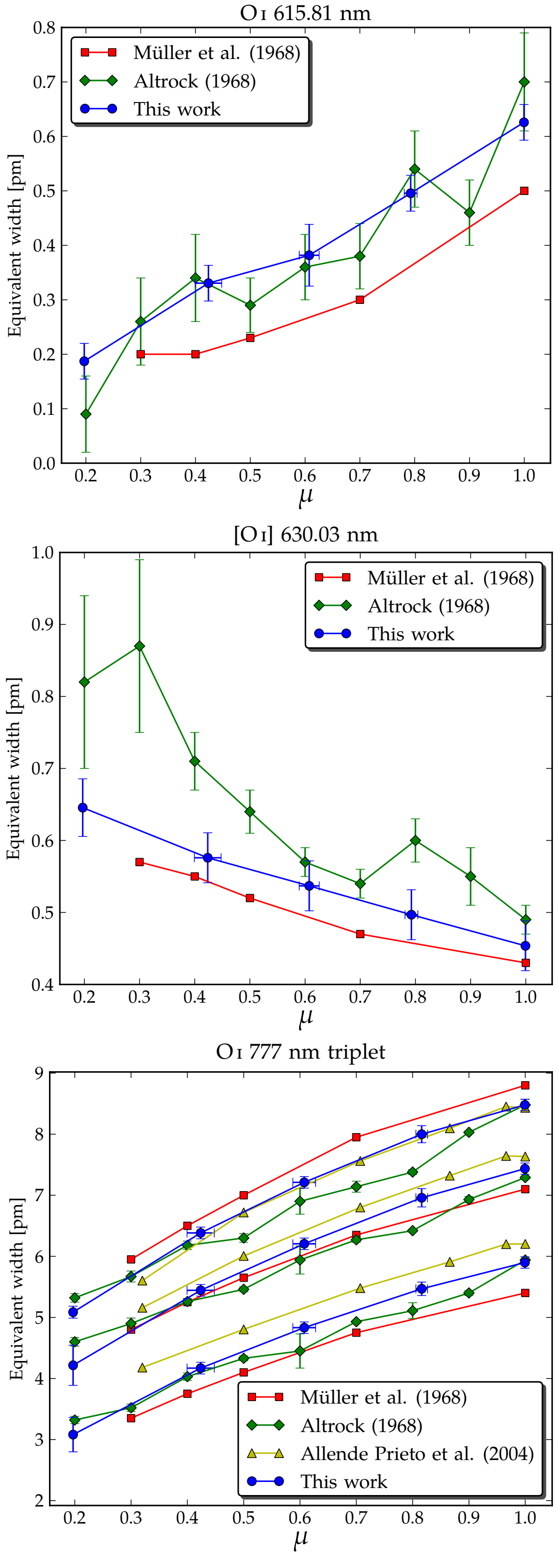

Figure 4.2 Equivalent width vs. μ for the oxygen lines, for different observations. Last panel shows the three 777 nm O I triplet lines (from strongest to weakest: 777.19 nm, 777.41 nm, 777.53 nm).

4.3. Theoretical line profiles

We employ the 3D time-dependent hydrodynamical simulation of the solar photosphere used in Chapter 3 (Trampedach et al., in preparation; Asplund et al., in preparation). This model was computed using a more recent version of the Stein & Nordlund codes. When compared with the 3D model of Asplund et al. (2000a), it includes more detailed radiative transfer: 12 opacity bins, additional sources of continuum opacities such as photo-ionization cross-sections from the Opacity and Iron Projects (Cunto et al., 1993; Hummer et al., 1993), etc. In Fig. 2.1 we show the differences in the mean temperature structure (averaged over surfaces of constant optical depth) between both 3D models. A comparison is also made with one-dimensional, hydrostatic, time-independent solar model atmospheres, including the semi-empirical model of Holweger & Müller (1974) and the MARCS model (Gustafsson et al., 2008).

We computed the synthetic LTE and NLTE (oxygen only) line profiles, making use of our LTE line formation code and the MULTI3D code (Botnen, 1997; Asplund et al., 2003). For a more detailed description of the 3D model, line formation, and atomic data used, we refer to Chapter 3; however, a few things are done differently from Chapter 3. We made use of 90 snapshots of the 3D simulation (in Chapter 3 we used 20 snapshots). These cover ≈ 45 min of solar time and have $\langle T_{\mathrm{eff}} \rangle = 5778 \pm 14$ K. To save computational time, 3D NLTE line formation was only carried out on four snapshots (chosen to have a representative range of effective temperature and time coverage). Using MULTI3D, we computed NLTE and LTE line profiles, which were used to obtain the wavelength-dependent NLTE/LTE ratio for each μ value. In contrast with Chapter 3, the NLTE/LTE ratio was averaged over all the spatial points and the four snapshots. For each μ value, we then multiplied the NLTE/LTE ratio by the spatially and temporally averaged LTE line profiles (computed with our LTE code for all the 90 snapshots). The NLTE line

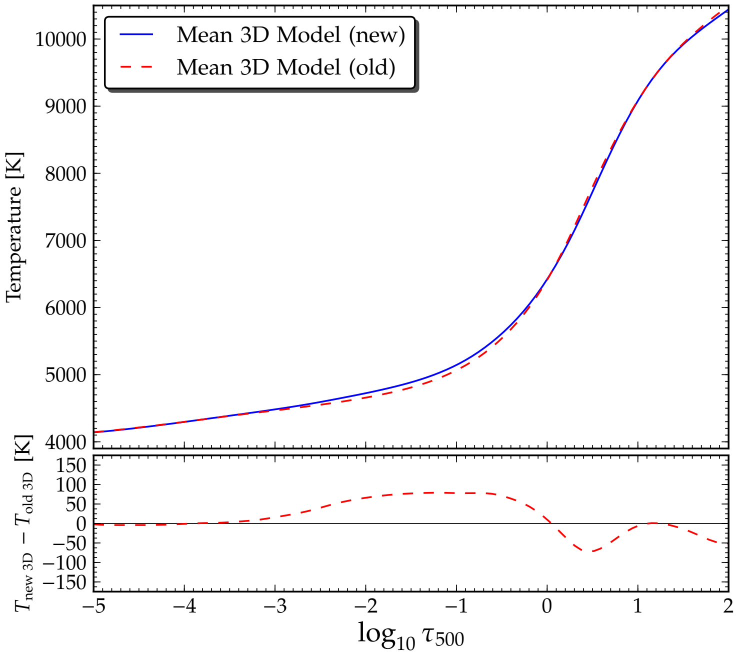

Figure 4.3 Comparison of the mean temperature structure of the new 3D model used in this work and the 'old' 3D model of Asplund et al. (2000a), plotted against the optical depth at 500 nm.

profiles were computed for eight different values of S_H: 0.01, 0.1, 0.3, 0.5, 1, 1.5, 3, 10.

With the 1D MARCS and Holweger–Müller model atmospheres, line profiles were computed using the same procedures, opacities, and radiative transfer. The exception is that a microturbulence of $\xi_\mathrm{turb} = 1.0$ km s^{-1} was used when computing these line profiles. In addition, 1D line profiles were convolved with a Gaussian to account for macroturbulence. The adopted macroturbulences vary from line to line (see §4.4). For consistency, 1D NLTE line formation was computed in a similar manner to the 3D model, obtaining the NLTE to LTE ratio from MULTI3D and multiplying it by the profiles obtained with the LTE code (even though there is only one snapshot for the 1D models).

Our main focus are oxygen lines. However, a few lines from other elements are also present in our observations. These lines and their properties, along with the oxygen lines, are listed in Table 3.2. In §4.4.4 we briefly discuss the results for the centre-to-limb variation of these lines. For the oxygen lines and, when available, for lines of other elements the collisional (van der Waals) broadening was computed using the quantum mechanical theory of Anstee & O'Mara (1995); Barklem & O'Mara (1997); Barklem et al. (1998), avoiding the need for conventional Unsöld (1955) enhancement factors.

4.4. Results

The synthetic line profiles are compared with the observations by means of fitting and equivalent width. Before a comparison was made with our observations, the synthetic line profiles were convolved with a Gaussian (equivalent to $\lambda/\Delta\lambda$=200 000) to account for the instrumental profile of the spectrograph. When comparing line profiles with the FTS intensity atlas, no convolution took place, because of the very high resolution of the atlas. The line-profile fitting was performed using the L-BFGS-B optimization algorithm (Byrd et al., 1995).

4.4.1. O I infrared triplet

Context

The three O I lines around 777 nm are strong and lie in a part of the solar spectrum that is relatively free of blends and telluric lines. These two characteristics alone make them a good abundance indicator. However, these lines show significant departures from LTE in the Sun (Altrock, 1968), because of a radiation field weaker than Planckian in the line formation region (*e.g.* Eriksson & Toft, 1979; Kiselman, 1993).

Aside from the increased computational expense of computing the 3D NLTE radiative transfer for these lines, departures from LTE introduce additional uncertainties stemming from the input physics, in particular photo-ionization rates and collisional cross-sections with electrons and H I. The latter, as noted in §4.1, are often taken from the classical estimates and scaled by an S_H factor. For the O I 777 nm lines, a scaling factor for the H I collisions was tried by Kiselman (1993) to reconcile different 1D models with observed centre-to-limb variation of the equivalent widths. Further investigation of the 3D and NLTE effects on these lines is provided by Kiselman & Nordlund (1995), using an early

3D model and showing the feasibility of the line centre-to-limb variations to probe for the atomic parameters (i.e., S_{H}). This suggestion was followed by Allende Prieto et al. (2004, hereafter AAF04), who used the centre-to-limb variation of the O I 777 nm lines and a 3D model to empirically deduce that $S_{\mathrm{H}} = 1$ was preferable to $S_{\mathrm{H}} = 0$.

Our work differs from AAF04 in that we use a different set of observations and 3D model, a greater range of S_{H} values, a more up-to-date atom, and more detailed radiative transfer for the NLTE calculations (more simulation snapshots included in the full 3D NLTE, more angles used in MULTI3D).

Comparison with observations

Our goal is to find the S_{H} that best describes the centre-to-limb variation of the line strength. For this purpose we have two diagnostics: equivalent widths and line-profile fitting.

Measuring the variation of line strengths by profile fitting has the advantage of being less sensitive to systematics (*e.g.* blends, noise) than the equivalent widths. But when the shape of the line profiles does not match the observations, the line profiles adjusted in abundance will have a slightly different equivalent width than the observations. We present the results using both diagnostics, and they both suggest a very similar result.

To fit the line profiles, we vary two parameters: oxygen abundance and wavelength shift (of the observations). The latter is necessary because of the uncertainty in the wavelength calibration. For the 1D models, another free parameter was allowed in the fit: macroturbulence. Ideally it should not be allowed to vary freely, but instead extracted from nearby lines. The scarcity of lines in our observed window around 777 nm makes this task difficult; in our observed window, there is only one other line, a strong Fe I line. Deriving the macroturbulence from only one line would probably introduce a similar or larger error as allowing it to be a free parameter in the fit for the O I 777 nm lines.

The results for profile fitting and equivalent width for the 3D model are given in Fig. 4.4. For the equivalent widths, the oxygen abundance was adjusted for each line so that it matched the observations at disk-centre. The same abundance was then used for all the other values of μ. Both diagnostics indicate that $S_{\mathrm{H}} = 1$ agrees most closely with the observations, with a small variation from line to line. It is shown with a high confidence level that LTE line formation is not a valid approximation for these lines. In Table 4.2 we list the derived abundances from fitting the disk-centre line profiles, using 3D NLTE radiative transfer for different values of S_{H} both for our observations and the FTS atlas of Brault & Neckel (1987). Line profiles were fitted in the following wavelength ranges: 777.175–777.24 nm, 777.36–777.46 nm and 777.50–777.565 nm.

Corresponding results for the 1D models are given in Fig. 4.5, but only for the O I 777.41 nm line; the other lines behave similarly. They indicate a mixed scenario. On one hand, the Holweger–Müller model gives a similar result to the 3D model: the best agreement is with $S_{\mathrm{H}} = 1$. But for the MARCS model, no value of S_{H} can agree reasonably with the observations, both in equivalent width and line profile fitting.

In Fig. 4.6 the 3D model predicted line profiles for disk-centre (adjusted in abundance) and the limb (using the disk-centre abundance) are shown for LTE and $S_{\mathrm{H}} = 0.01$, 0.3, and 1.

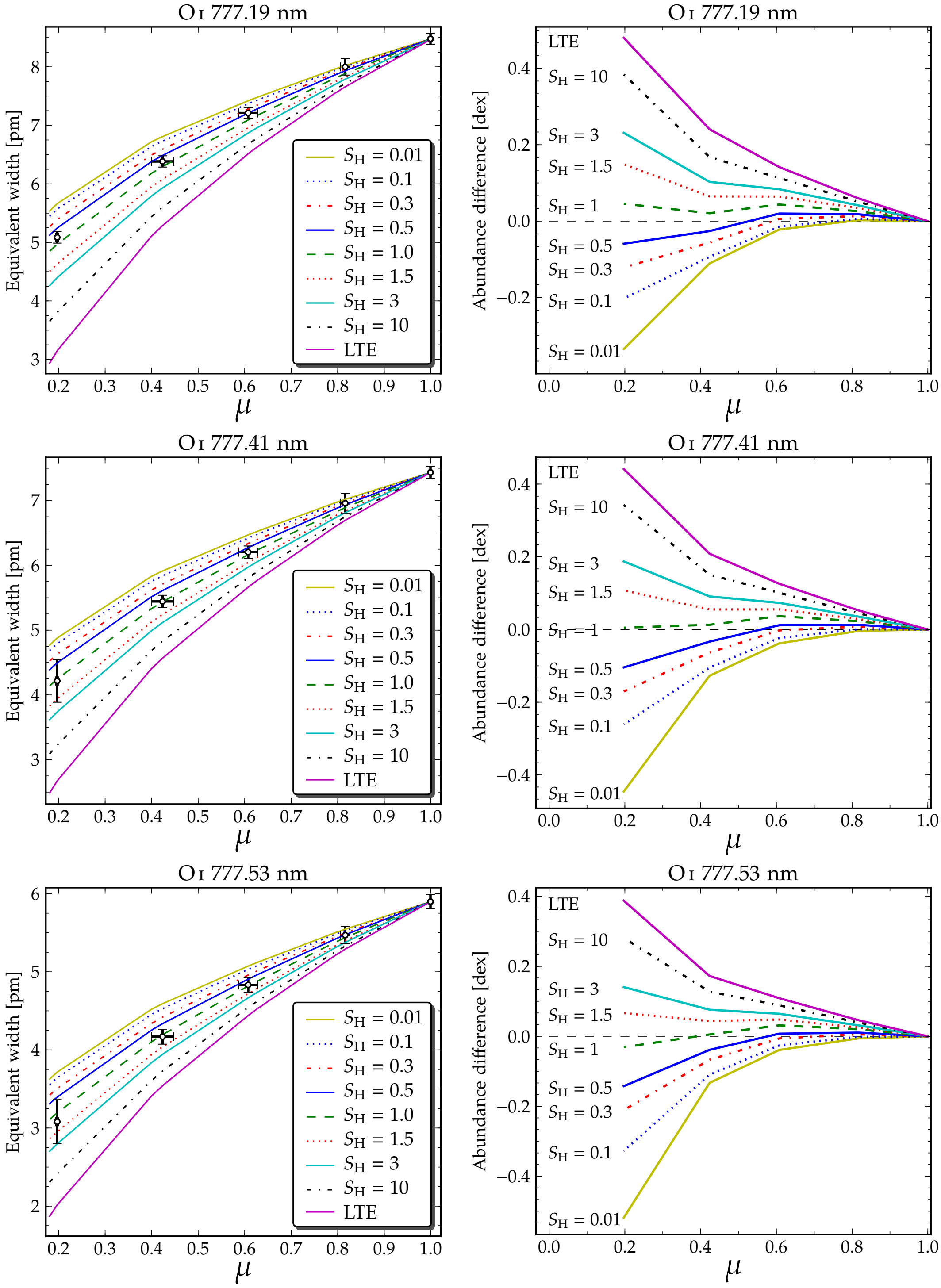

Figure 4.4 *Left panels:* equivalent width vs. μ for the three triplet lines, using 3D LTE and NLTE with different S_H coefficients for hydrogen collisions. The oxygen abundance was adjusted so that the models have the same equivalent width as the observations at disk-centre. *Right panels:* difference in fitted abundance from disk-centre to a given position in μ. Synthetic profiles were fitted against the observations at each μ, and the figures show how much the fitted abundance varies from the fitted value at disk-centre.

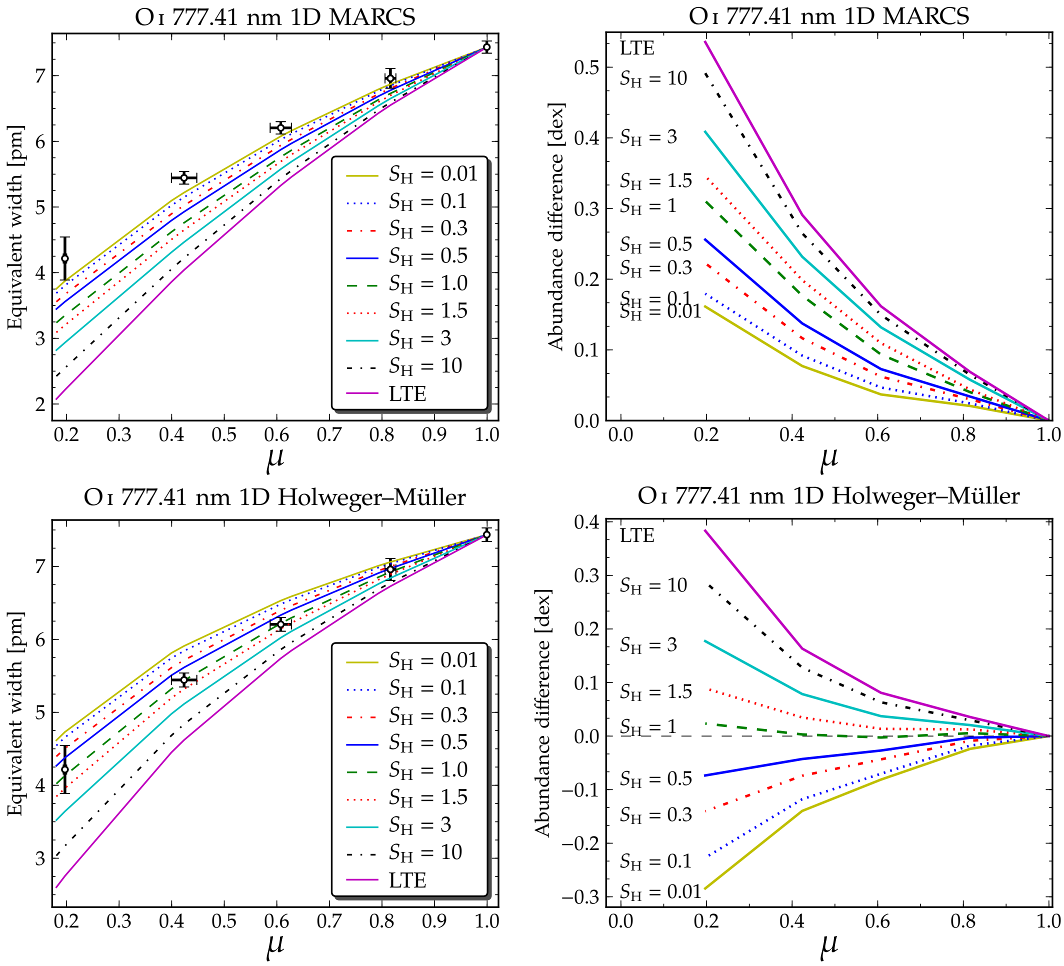

Figure 4.5 Same as Fig. 4.4 but for the 1D models and only for the O I 777.41 nm line.

It can be seen that LTE performs very poorly at the limb (too weak), so that $S_H = 0.01$ does not fare much better (too strong) and that $S_H = 1$ agrees better.

One can also see that the LTE profiles seem to fit the observations better at disk-centre. The disk-centre profiles for $S_H = 1$ are narrower and deeper than the observed. At the limb, in terms of shape alone, $S_H = 1$ profiles have a much better fit. The S_H that best describes the centre-to-limb variation of the line strengths does not seem to be the best at describing the shapes of line profiles at disk-centre. This same effect is more obvious when looking at the granulation variation of the FWHM at disk-centre (see §3.5.4). It may very well be connected with the finding of Chapter 3 that no single S_H agrees well with the observed equivalent widths for both granular and intergranular regions. The reason for these discrepancies is not clear yet.

To better quantify the agreement with the observations of different S_H, a χ^2 minimization was made with the equivalent widths, simultaneously for the three lines and for the five μ values. For each value of S_H, we varied the oxygen abundance and found the value that minimizes the squared difference between observed and predicted equivalent widths, weigthed by the observational error bars. The reduced χ^2 is defined as $1/N \cdot \sum \left(W_{\rm obs} - W_{\rm model}\right)^2 / \sigma^2$, where N is the number of degrees of freedom (in this case,

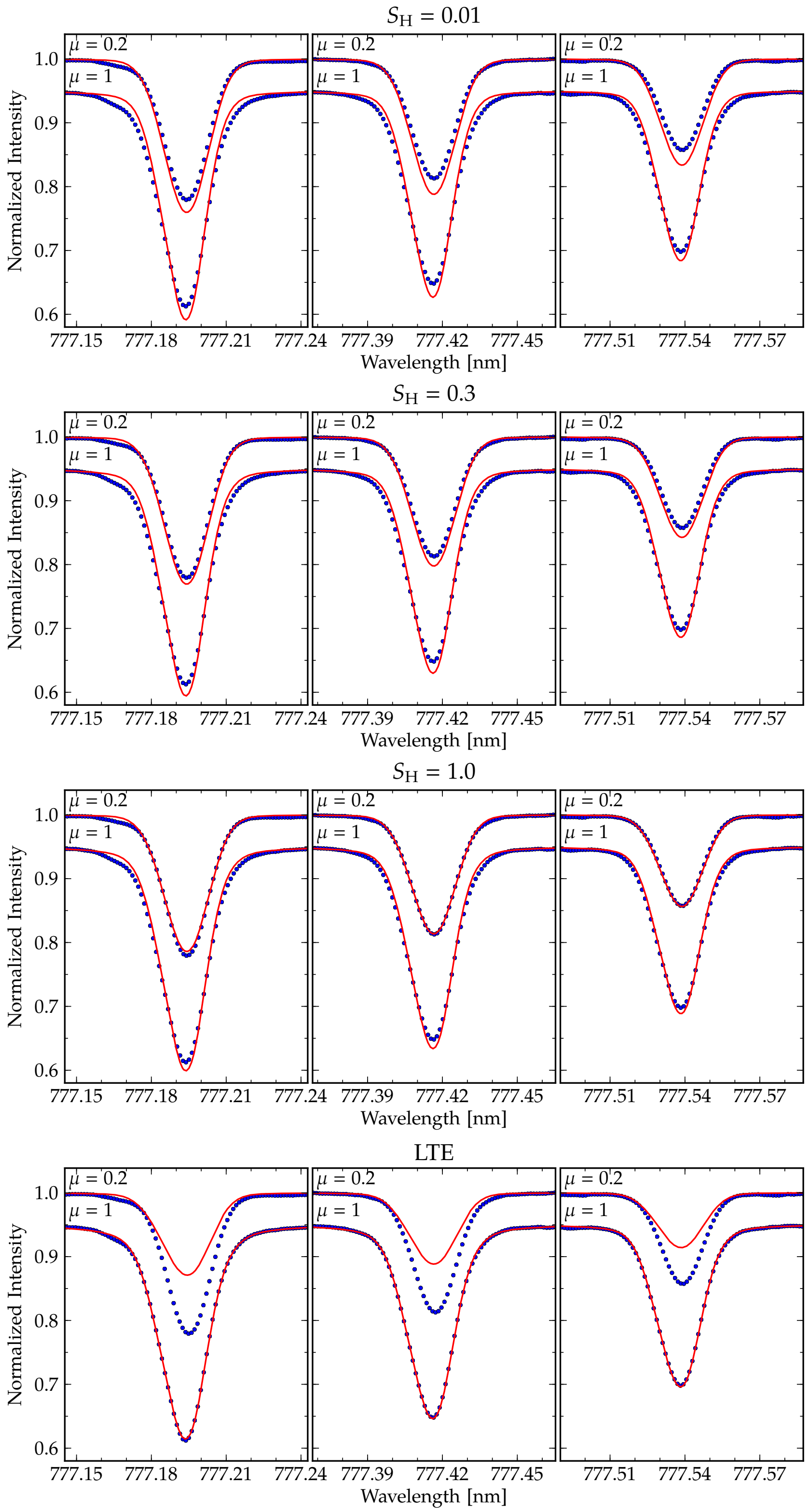

Figure 4.6 Our observations (dots) and 3D synthetic line profiles (solid line). Each panel shows the 777 nm triplet lines at disk-centre and $\mu = 0.2$, for LTE and three different S_H values. The line profiles at disk-centre were fitted to the observations, while at $\mu = 0.2$ the abundance was set fixed to the disk-centre abundance, while the waveshift was adjusted. For clarity, disk-centre line profiles have been subtracted by 0.05.

Table 4.2 Derived disk-centre oxygen abundances ($\log \epsilon_\mathrm{O}$) from from the 3D model.

O I line [nm]	S_H	SST/TRIPPEL	FTS atlas
777.19	0.01	8.50	8.52
	0.1	8.53	8.55
	0.3	8.58	8.60
	0.5	8.61	8.63
	1	8.66	8.68
	1.5	8.73	8.75
	3	8.76	8.77
	10	8.82	8.84
	LTE	8.87	8.88
777.41	0.01	8.54	8.55
	0.1	8.56	8.57
	0.3	8.60	8.61
	0.5	8.63	8.64
	1	8.69	8.69
	1.5	8.74	8.75
	3	8.76	8.77
	10	8.82	8.83
	LTE	8.85	8.86
777.53	0.01	8.58	8.58
	0.1	8.60	8.60
	0.3	8.63	8.64
	0.5	8.65	8.66
	1	8.69	8.70
	1.5	8.74	8.75
	3	8.75	8.76
	10	8.80	8.81
	LTE	8.83	8.83

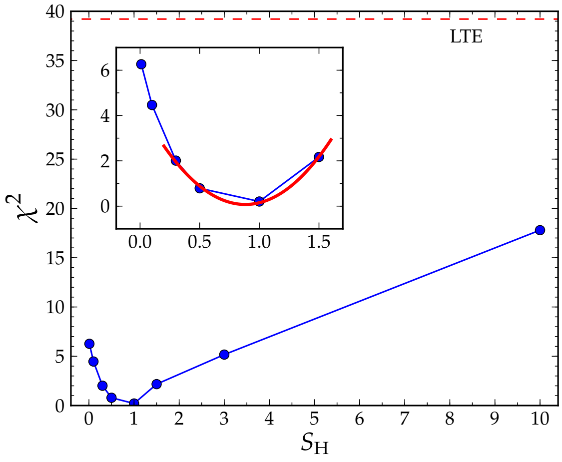

Figure 4.7 Reduced χ^2 as a function of S_H from the minimization of the equivalent widths (see text), for the 3D model. The LTE value is indicated (dashed line). The minimum at $S_\mathrm{H} = 1$ indicates the best agreement with the observations. *Inset:* same plot in more detail for $S_\mathrm{H} < 2$, showing the parabolic fit to the lower χ^2 values (thick solid line).

$N = 15 - 1$). The χ^2 values, as a function of S_H are shown in Fig. 4.7. Comparing for all the S_H, we identify the value that agrees better, using a parabolic fit to the lower χ^2 values.

For the 3D model, we find the χ^2 minimum to be at $S_\mathrm{H} \approx 0.85$. We used this value to derive the oxygen abundance from these lines. Averaging over the three lines we obtain an oxygen abundance of $\log \epsilon_\mathrm{O} = 8.68$ for the 3D model. By repeating the procedure for the 1D Holweger–Müller model we also obtain $S_\mathrm{H} \approx 0.85$, deriving an abundance of 8.66. Although with the 1D MARCS model no S_H reproduces the observations, for comparison we derive an abundance of 8.61 using $S_\mathrm{H} = 0.85$.

Comparison with previous work

At first glance our findings are consistent with the $S_\mathrm{H} = 1$ estimated by AAF04. But these two findings cannot be directly compared, as we use a different 3D model. To compare our methods and observations with AAF04, we repeated our analysis for the same 3D model they use. The best-fitting value is then $S_\mathrm{H} \approx 0.3$, which is close to the observations as $S_\mathrm{H} = 1$ with the new 3D model. Between $S_\mathrm{H} = 0$ and $S_\mathrm{H} = 1$ (the two values tested by AAF04) we find that the latter agrees better with the observations, consistent with the findings of AAF04. But the best fit of $S_\mathrm{H} \approx 0.3$ indicates a model dependence in this derivation, also seen for the 1D models. Interestingly, although the best-fitting S_H varies for the two 3D models, the abundances derived from profile fits with the best choice S_H are almost unchanged between the two models ($\lesssim 0.01$ dex).

Effect of blends and electron collisions on the inferred S_H and abundances

There are a few weak CN and C_2 lines in the 777 nm region. The VALD database also lists some weak atomic lines. Most of these lines are very weak and their effect on the O I lines negligible. At disk-centre the known blends[1] of the O I lines are very faint, and their effect on the abundance obtained by profile fitting is negligible. But as molecular lines get stronger at the higher layers probed by the limb spectra, it is important to determine whether they have any effect on the inferred S_H. To investigate for such effects, we computed the spectra of O I 777 nm over a larger spectral region including additional molecular and atomic lines, with data from J. Sauval (2008, private communication). Our testing showed that the blends have very little influence on the derived S_H value. Because the atomic and molecular data for these weak blending lines is not known accurately, they have not been included in our main analysis.

We also investigated the effect of computing the O I lines simultaneously. Their wings are very extended and overlap, especially in LTE and for 777.41 and 777.53 nm. For LTE at disk-centre, computing the three O I lines simultaneously caused a reduction of 0.002 dex in the fitted oxygen abundance of 777.41 nm line. At the limb there is virtually no difference between computing the lines separately or together, because the lines are much weaker. For the same line strength, the LTE profiles have the most extended wings

---

[1] There are a few unknown blends visible in the disk-centre spectrum. Most notably, the feature at the 'knee' of the wing of the 777.19 nm line. Their effects in the fit were minimized by limiting the profile-fitting region to parts not visibily affected by blends.

when compared with NLTE (the extent of the wings gets smaller with smaller S_{H}), so the issue of overlapping wings gets more important for the LTE profiles. Our single-line approximation is thus fully justified.

We used the revised electron collision data of Barklem (2007). Although this data is believed to be the most accurate currently available, it is important to check to what extent our empirically estimated S_{H} depends on the adopted electron collision rates. To assess this effect, we performed several tests by artificially changing the electron collisions. Due to time constraints, these tests were performed in 1D models, although they were confirmed with a few 3D runs. An interesting find is that, if the electron collision rates are artificially decreased, the best-fitting S_{H} value is still the same (even if we neglect electron collisions altogether). Obviously the fitted abundance values will differ (especially for $S_{\mathrm{H}} < 1$), but the best fitting value remains the same. This result indicates that H I collisions are more important than electron collisions in the centre-to-limb variation of the lines, because the electron pressure decreases more quickly with height. On the other hand, if the electron collision rates are increased by one order of magnitude, it will change the best-fitting S_{H} value. This makes sense, as an increase in the collisions from electrons will shift the result more towards LTE, regardless of the S_{H} used.

4.4.2. [O I] 630.03 nm and Ni I blend

Context

Although the forbidden O I line at 630.03 nm is the strongest of the [O I] lines, it is still very weak in the Sun. Unlike the permitted lines, LTE is a very good approximation in the formation of the [O I] line (see Asplund et al., 2004). Accordingly, we only use the synthetic LTE profiles in the following analysis. As a weak line it is highly susceptible even to faint blends. In particular, it is blended with an Ni I feature at 630.0335 nm (Lambert, 1978; Allende Prieto et al., 2001; Johansson et al., 2003). For the Sun, the contribution of the Ni I component to the blend is about 30%, depending on the Ni abundance used. With such a significant blend, it is paramount to properly account for the Ni contribution. This work is similar to the work of Allende Prieto et al. (2001, hereafter ALA01), which included an analysis of [O I] 630.03 nm with a 3D model (albeit an earlier version), but for the flux profile instead of intensity at different μ values; also Caffau et al. (2008a) and Ayres (2008) has performed similar studies using a different 3D model.

Ni I blend

Properly accounting for the Ni I blend means one needs to know its properties with high precision. Johansson et al. (2003) measured the $\log gf$ for this Ni I transition to be −2.11. Because of the presence of several Ni isotopes and their isotopic splitting, the Ni contribution at 630.03 nm is given as a series of blends. In our treatment we included the five most abundant Ni isotopes, scaling the $\log gf$ by their isotopic abundance (see Table 4.3). We used a fixed Ni abundance of $\log \epsilon_{\mathrm{Ni}} = 6.22$, as inferred from other Ni lines using the present 3D model (Asplund et al., 2009).

Table 4.3 Ni I isotopes used and scaled $\log gf$ values

Ni isotope	%[a]	Wavelength [nm][b]	$\log gf$
^{58}Ni	68.27	630.0335	-2.2757
^{60}Ni	26.10	630.0355	-2.6933
^{61}Ni	1.13	630.0365	-4.0569
^{62}Ni	3.59	630.0375	-3.5549
^{64}Ni	0.91	630.0395	-4.1509

[a] Isotopic fractions from Rosman & Taylor (1998)

[b] Wavelength of main component and isotopic splitting from Johansson et al. (2003)

An important difference between the present work and ALA01 was the treatment of the Ni I blend. We used a fixed Ni abundance of 6.22 and adopted the measured $\log gf$ of −2.11, whereas at the time of ALA01 there was no experimental $\log gf$, and Ni was treated as a free parameter. Their best-fitting $\log(gf\epsilon_{\rm Ni}) = 3.94$ is equivalent to an Ni abundance of 6.05 with the present value of $\log gf$, less than the Ni abundance we used. In ALA01, the blend of the O I and Ni I was done by co-adding the individual flux profiles for the different species. Because these are very weak lines, that was a reasonable approximation. However, the approximation of co-adding the profiles starts to break down as one looks at profiles of lower μ values, where the difference between co-adding and a proper treatment of the blend (summing the opacities for each component) can amount to a few percent of the equivalent width. In this work we opted to treat the blend properly, instead of co-adding the profiles.

Wavelength calibration

Another important point in the treatment of this line is the wavelength calibration. As Ayres (2008) notes, the balance between the components of the blend is sensitive to velocity errors of a few hundred $\mathrm{m\,s^{-1}}$, or a few mÅ. If the wavelength calibration translates the line to be blueshifted from its 'true' location, the fitting will favour a higher oxygen abundance. There is a degeneracy between the wavelength shift and the Ni abundance, which makes it difficult to determine the best-fitting values when both are allowed to vary.

Unfortunately, the absolute wavelength calibration of neither our observations nor the FTS atlas is precise enough for the analysis of this blend, so we adopt a correction to the laboratory wavelength similar to that of Ayres (2008): using strong Fe I lines in the neighbourhood to find the wavelength difference between the 3D model and the observations. By measuring the wavelength difference between the synthetic profiles and the observations for a set of reference Fe I lines, one can effectively put the profiles on the same 'laboratory' wavelength scale. This approach has the advantange of removing the systematics associated with the observations (*e.g.* solar rotation) and any shortcomings in the 3D model (*e.g.* overshooting of convective blueshifts). We chose the three Fe I lines at 629.77, 630.15, and 630.24 nm – because they were available in the limited wavelength window of our observations – to calibrate the wavelength scale. To measure the wavelength difference we fit the theoretical 1D and 3D line profiles of these Fe I lines and allow a wavelength shift of the observations as a free parameter. The mean wavelength shift from the three lines was extracted for line profiles at all the solar disk positions of our observations. The standard deviation between the shifts from the three Fe I lines were 19, 27, 33, 51, 140 $\mathrm{m\,s^{-1}}$ for $\mu = 1, 0.8, 0.6, 0.4, 0.2$, respectively. Except for the $\mu = 0.2$ measurement, the numbers are an encouraging sign of how precise the wavelength calibration is. For the observations at $\mu = 0.2$, we adopted the wavelength shift as given by the Fe I 629.77 nm line because of the scatter between Fe I line indicators.

If the wavelength shift of the synthetic line profile was allowed to be a free parameter in the fit, then the best-fitting shift to the FTS intensity atlas is very close ($< 75\ \mathrm{m\,s^{-1}}$) to the fixed shift obtained by the Fe I line procedure. Its effect on the derived abundance is thus small (< 0.01 dex). Even if one accounts for some uncertainty around the wavelength shift, the effects on the oxygen abundance are weak. A relatively large variarion of ($\pm 330\ \mathrm{m\,s^{-1}}$) around the used waveshift for the FTS intensity atlas has an effect on the oxygen abundance of $\approx \mp 0.015$ dex, although the agreement with the observed profile deteriorates significantly. These variations in the oxygen abundance are much smaller than the ones found by ALA01 when trying different shifts. The difference stems likely from our keeping the nickel abundance fixed, while ALA01 allowed it to be a free parameter in the fit. With nickel fixed, the fitting procedure cannot compensate with more or less nickel, which means that the line shifting has less effect on the oxygen abundance.

Besides the absolute wavelength calibration of the observations, there is also the problem of the uncertainties in the laboratory wavelengths for the oxygen and nickel transitions. The total uncertainty in the wavelength difference between the lines is approx. ±0.236 pm, being ±0.2 pm for [O I] (Eriksson, 1965) and ±0.125 pm for Ni I (Johansson et al., 2003), weighted by the isotopes. We tested the line-profile fitting for the lines using the two extreme cases of wavelength differences allowed by the errors and found that its effect on the derived oxygen abundance is negligible (< 0.01 dex). Once again, this value is less than the 0.05 dex found by ALA01, because we do not have the nickel abundance as a free parameter.

Continuum level and fitting range

The local continuum of the [O I] + Ni I line wings is slightly depressed by the nearby Fe I and Si I lines, and also by $approx70$ weak CN lines between 630.00–630.06 nm, as noted by ALA01. To account for this effect, we multiplied each set of observations by a factor C. For the FTS intensity, atlas $C = 1.0054$ was used. It is important to note that the determination of this local continuum is a major source of the total uncertainty. If, for example, one took just the FTS intensity atlas's continuum and computed the equivalent width for this line, the equivalent width would be ≈ 30% higher. Care was taken in determining the local continuum for our observations, but one should keep the uncertainty attached to it in mind.

Another important but seldom discussed point in the profile fitting is the wavelength

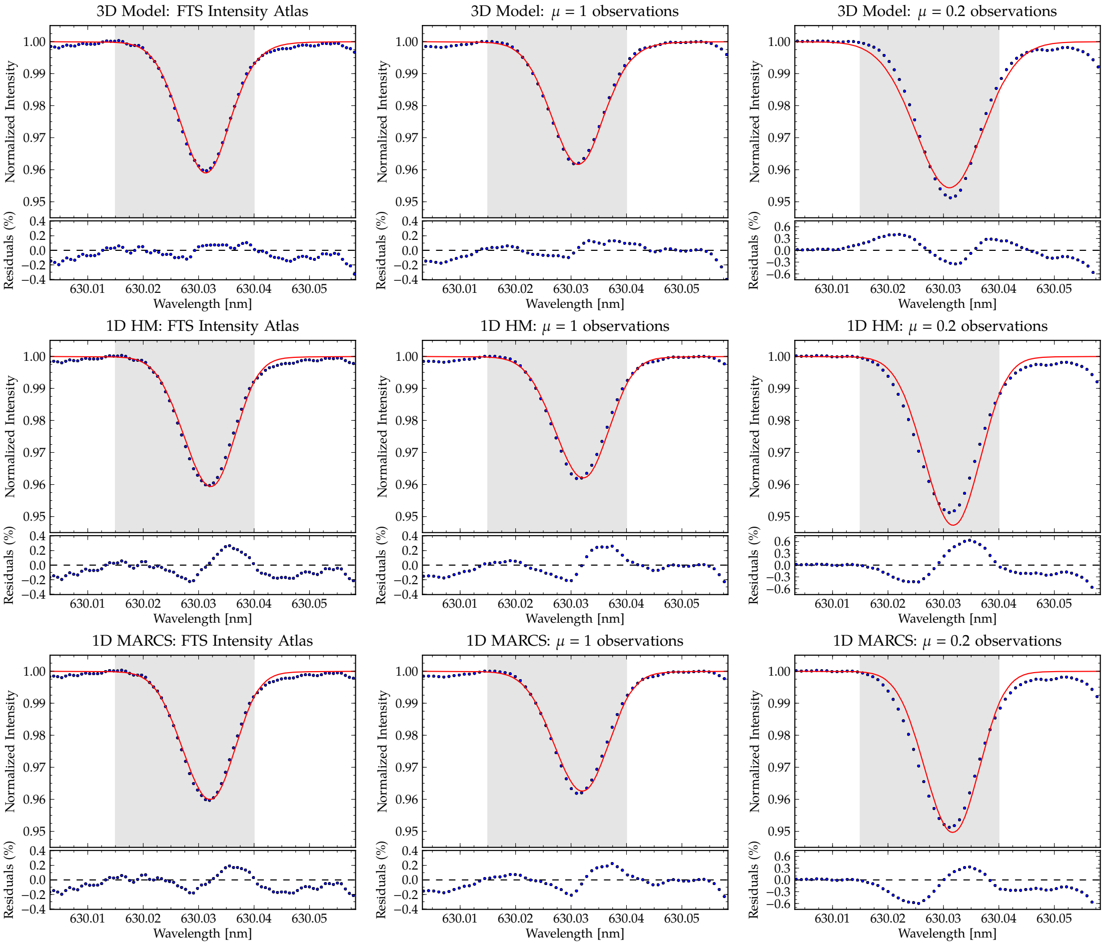

Figure 4.8 Synthetic line profiles (solid lines) for the O i+Ni i 630.03 nm blend vs. observations (circles). Shaded regions indicate the range over which the profiles were fitted. Left panels: fit for FTS Intensity atlas, done over the wavelength range of Allende-Prieto et al. (2001). Middle panels: fit for our observations, disk-centre. Right panels: our observations at $\mu = 0.197$, and profiles from models using abundance fitted at disk-centre, adjusted for continuum. The wavelength shift was measured for each model and disk position separately from Fe i lines (see text). Ni abundance was fixed at 6.22, 6.16, 6.26 for the 3D model, 1D MARCS model and 1D HM model, respectively.

range for fitting the profile. ALA01 did the profile fitting in the range 630.015–630.04 nm, others are not as explicit. Ideally one would like to perform the profile fitting in as broad as possible a range to include the maximum amount of information about the line. The presence of blends, especially unknown features, forces one to narrow the fitting range to avoid the influence on the fit of features not included in the line synthesis. We adopted the same wavelength range as ALA01, as it avoids several weak blends but includes most of the [O i] line.

Comparison with observations

The line profiles for the [O i] + Ni i blend were computed for a fixed $\log \epsilon_{\rm Ni}$ and assuming LTE. In the fit for this line profile we only allowed one free parameter: the oxygen abundance. The waveshift for each position was obtained by the Fe i lines method, and

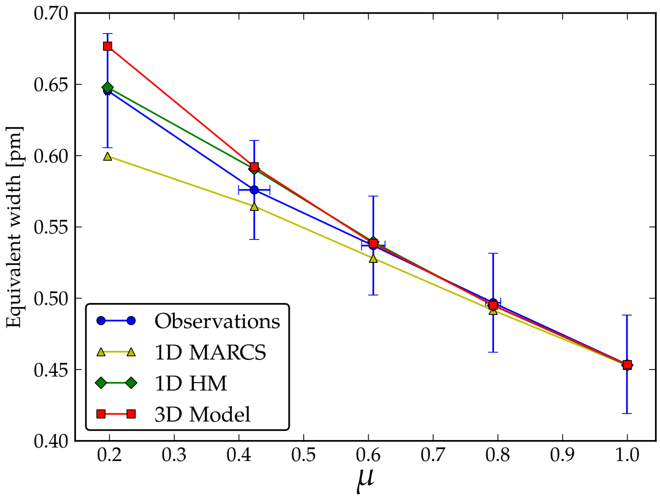

Figure 4.9 Equivalent width vs. μ for the [O I]+Ni I 630.03 nm lines blend, for our observations and different models at different positions in the solar disk.

the local continuum multiplication factor C obtained empirically, as noted above.

We present the results for the equivalent width analysis over the observed positions in the solar disk, the profile fitting of our observations at $\mu = 1$, 0.2, and the FTS intensity atlas for comparison with other studies. Some results from line fitting are in Fig. 4.8, and the equivalent width results are in Fig. 4.9. Fitting the line profile to the FTS intensity atlas we obtain an oxygen abundance of $\log \epsilon_{\mathrm{O}} = 8.66$, while we obtain 8.64for our observations at $\mu = 1$. In the variation of equivalent width with μ in Fig. 4.9, one can see that the 3D model predicts a slightly stronger line as μ decreases. In terms of fitting the line profiles for different μ, the variation in fitted abundance for the 3D model is never more than 0.02 dex for the disk-centre abundance. In the rightmost column of Fig. 4.8, we plot the observations at $\mu = 0.2$ with a synthetic profile using the oxygen abundances derived from the disk-centre fits (our observations), the continuum level adjusted independently. The 3D model at $\mu = 0.2$ is slightly stronger than the observations, and the line profile is slightly wider and not as deep as the observations. Still, in terms of best-fitting abundance, the difference is minimal.

For the 1D models we applied the same wavelength correction with Fe I lines, repeating the procedure for line profiles synthesized with the 1D Holweger–Müller and MARCS models. The best-fitting macroturbulence was also extracted from these Fe I lines and then used for [O I]+Ni I. The Holweger–Müller (HM) model does a good job describing the line strengths, as shown by the equivalent widths in Fig. 4.9. However, a closer inspection of the line profiles shows a red wing that is too strong. This may possibly indicate an excess of nickel: $\log \epsilon_{\mathrm{Ni}} = 6.26$ was used for this model, as derived with the same model using other Ni lines. Looking at Fig. 4.8, in particular at the residuals, it is clear that the agreement is not as good as for the 3D model. This is expected, because the 1D models do not reproduce the convective motions in the photosphere realistically (unlike the 3D model), even when using micro and macroturbulences. In particular for the HM at $\mu = 0.2$, the macroturbulence derived from the Fe I lines is probably low, as the line profile is noticeably deeper than the observations, while the equivalent widths are very similar. For the MARCS model, the trend in equivalent width vs. μ is different. The model predicts slightly weaker line strengths than the observations. The fitted line profiles at disk-centre also indicate an excess of intensity in the red wing. The line profile at low μ with the disk-centre abundance shows a slightly weaker line than the observations. The oxygen abundances from profile fitting with the FTS disk-centre atlas for the HM and MARCS models were, respectively, 8.69 and 8.66.

Comparison with previous work

An easy comparison to be made is with ALA01. Some things have been done differently in the present study. We computed a proper blend of the two transitions (adding line opacities), instead of computing separate line profiles for each line and co-adding them. We also performed a more precise wavelength calibration using Fe I lines. And finally, we employed a more recent 3D model and a higher Ni abundance. Fitting the flux profiles against the FTS flux atlas and using the same fitting range in ALA01, we obtained an oxygen abundance 0.07 dex lower. The reason for this difference is mainly the higher Ni abundance used (6.22 vs. 6.05), which translates to a ≈ -0.07 dex difference in the derived oxygen abundance. The proper blending of the line instead of co-adding profiles causes a difference of -0.01 dex in oxygen. The proper wavelength calibration using Fe I lines instead of only correcting for gravitational redshift causes a difference of +0.01 dex.

Fitting the line profiles with $\log \epsilon_{\mathrm{Ni}} = 6.22$ instead of 6.05 leads to closer agreement with the observed disk-centre profile ($\chi^2_{6.22} \approx 0.53\chi^2_{6.05}$), but worse agreement for the observed flux profile ($\chi^2_{6.22} \approx 1.51\chi^2_{6.05}$).

4.4.3. O I 615.81 nm

Context

The O I 615.81 nm line is a triplet, with components at 615.8149, 615.8172, and 615.8187 nm, according to the NIST database. The last is the strongest component. The components are so close that they are unresolved in the solar spectrum. Its position in the solar spectrum is far from optimal. The line is close to a strong (≈ 4.8 pm) Fe I line at 615.77 nm, and there are multiple weak blends around. The VALD database lists several atomic lines in this region, but besides the strong Fe I line, only the Nd II 615.782 nm, Ni I 615.800 nm, and Fe I 615.803 nm lines have any measurable effect, though they are still just barely noticeable. Spectral synthesis using only these lines is still not enough to explain the solar spectrum. However, there seem to be several molecular lines in this region. These are mostly CN lines, with a few C_2 lines. The molecular lines are important for our analysis, and their effect is discussed below. It should be noted that, even accounting for the molecules, there are still unidentified features in this spectral region, most notably the feature at around 615.793 nm.

The presence of these blends depresses the continuum level around the O I lines, so that it becomes a significant source of uncertainty. Our analysis, whether computing the equivalent widths from the observations or fitting the line profiles, suffers from the same problems. For example, if one assumed this oxygen line has no blends and takes the continuum level of the FTS disk-centre intensity atlas, then the equivalent width could be up to 33% higher than our estimate for the oxygen-only contribution. This effect is amplified as one looks at spectra closer to the limb because the different blends

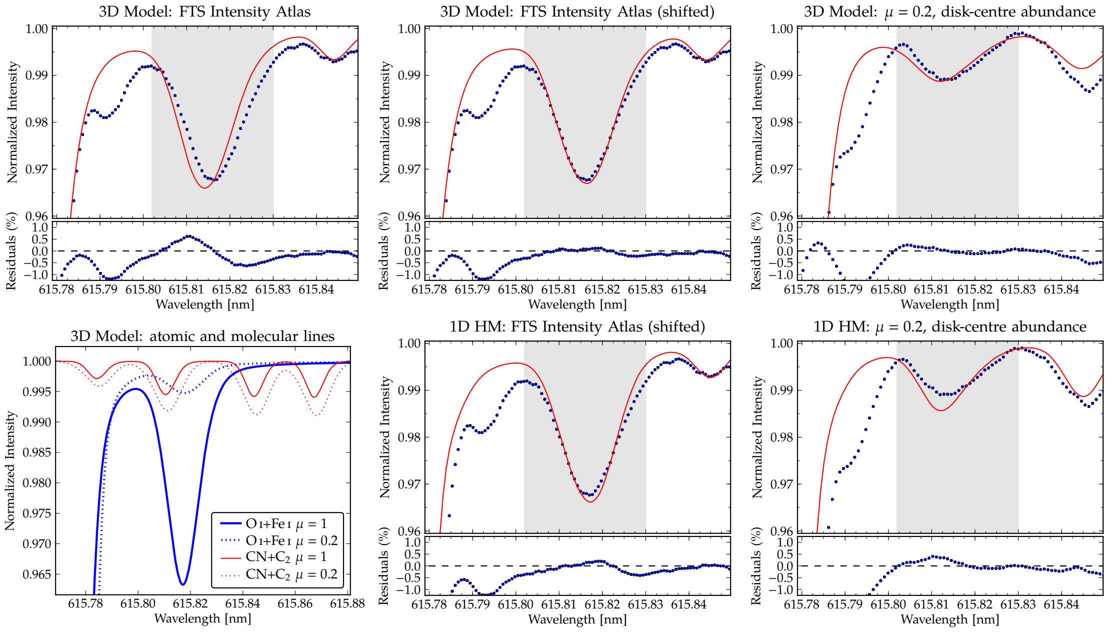

Figure 4.10 Synthetic LTE line profiles for the O I 615.81 nm lines (including blends from Fe I, one C_2, and five CN lines). All panels except lower left show synthetic profiles (solid) vs. observations (circles). Top left panel: location of the O I line with respect to the observations, using waveshift from Fe I lines and laboratory wavelengths from the NIST database. Middle panels: disk-centre line profiles for the 3D and 1D Holweger–Müller models with the O I lines artificially shifted to the red. Right panels: limb line profiles for the 3D and 1D Holweger–Müller models, using the same shift as in the middle panels. Disk-centre profiles were fitted for abundance, while the disk-centre abundance was used for the limb profile. Lower left panel: synthetic profiles illustrating the effects of the atomic and molecular blends at disk-centre and limb. Shaded regions indicate the range over which the disk-centre profiles were fitted.

vary differently in strength over the solar disk, which makes a precise determination of the continuum level difficult. Unlike the stronger O I 777 nm triplet, the predicted NLTE effect is rather weak for the O I 615.8 nm lines: Asplund et al. (2004) predict it to be −0.03 dex when neglecting H I collisions.

Wavelength calibration

A similar approach to the wavelength calibration of [O I] 630.03 nm was used. Because a precise wavelength calibration for this line is not as crucial as [O I], we derived the wavelength calibration using only the nearby Fe I 615.77 nm line. It is important to make the wavelengths of the O I consistent with this Fe I line because they lie on its red wing, and a different wavelength difference between them would imply either a lower or higher blend influence.

By using the reference laboratory wavelengths from the NIST database for the Fe I 615.77 nm and O I 615.81 nm lines and calibrating with the waveshift of Fe I lines, the synthetic O I profiles are shifted from the observations. This can be seen in the left panels of Fig. 4.10. The 3D synthetic profile is blueshifted relative to the observations, while the opposite happens for the 1D models. None of them matches the observations perfectly. For the 3D case, the shift to the observations is about 0.89 km s^{-1}, or 1.8 pm. This could mean that there is a significant error in the laboratory wavelengths, the predicted line shifts from the 3D models are inconsistent for the Fe I and O I lines, or there are blending features causing a shift in the profile. Including known molecular and weak atomic lines is not the explanation. In the top middle panel of Fig. 4.10 we artificially shifted the O I lines, so that the synthetic profile matches the FTS intensity atlas. For the rest of the analysis, we use these artificially shifted profiles (both for 3D and 1D models), but the derived abundance from fitting the disk-centre profiles remains essentially the same if the profiles are not shifted (but as seen in Fig. 4.10, the agreement with the observations is worse). The results for the equivalent widths are not affected by this shift.

Molecular blends and comparison with observations

We included several CN and C_2 lines in the 615.8 nm region (J. Sauval, 2008, private communication). The line data are given in Table 4.4. These data were obtained from from J. Sauval (2008, private communication). The molecular line data is uncertain, especially wavelengths for CN lines. With this uncertainty in mind, we adjusted some of the wavelengths and $\log gf$ of the CN lines from Table 4.4. The two (9, 4) band lines at 615.8522 and 615.8796 nm were redshifted by 7.2 and 11.6 pm, respectively, so that they match two features in the solar disk-centre spectrum. Furthermore, the $\log gf$ values of these two lines have been increased so that they fit the observed features reasonably. For consistency the $\log gf$ values of the three other CN lines have been increased by the same amount. For the 3D model this increase in $\log gf$ amounts to 0.35 dex, and we note that CN lines from different bands do not necessarily require the same correction in abundance or $\log gf$. However, we used the same $\log gf$ correction because the data for the different CN lines have similar uncertainties. Additionally, the (10, 4) band line at 615.8223 nm has also been redshifted by 9.3 pm. As detailed below, the inclusion of molecules is paramount for understanding the solar spectrum at the limb.

Our synthetic profiles included a total of ten blends: the three O I lines, the strong Fe I line, and the molecular lines outlined above. There are other atomic lines in the region, not included because they are very weak. The profile fits in Fig. 4.10 include all these blends. In the lower left panel of Fig. 4.10 is shown the synthetic spectrum of only O I and Fe I compared with the molecules, at the disk-centre and limb. At 10.741 eV, the oxygen lines have a high excitation energy, making them very weak at the higher layers of the atmosphere probed by the limb spectra when compared to disk-centre. The molecules, on the other hand, are formed in cooler regions and are thus significantly stronger at the limb than at disk-centre. As is visible in the figure, at disk-centre the molecules blended with oxygen have a very small contribution to the total line strength, yet at the limb most of the line strength comes from molecules. This type of blending can explain the observations well. As seen in the top right panel of Fig. 4.10, the line profile shape and strength using the oxygen abundance fitted at disk-centre is very close to the observed profile[2]. Because the molecular lines to the blue of the oxygen line dominate at the limb, the line centre is significantly blueshifted as is also confirmed by the observations. (The wavelength calibration using the strong Fe I line proved important to establish this.)

---

[2] The oxygen abundance was the only adjusted parameter in the disk-centre fit, and all other lines have the same abundance and parameters throughout the analysis.

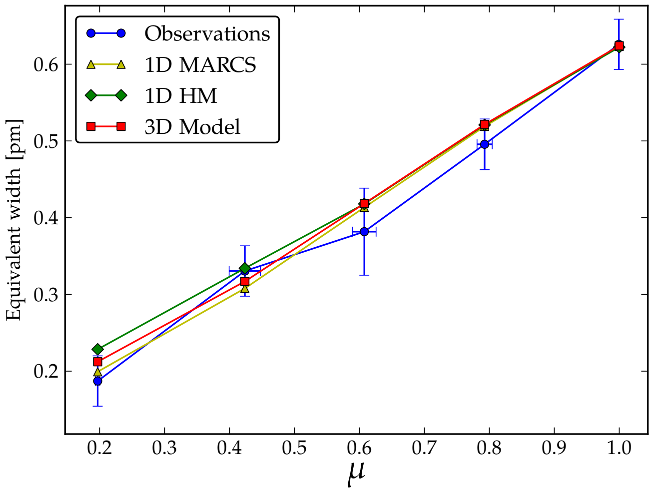

Figure 4.11 Equivalent width vs. μ for the three O I 615.81 nm lines, including the Fe I, CN and C_2 blends.

Table 4.4 Molecular lines included in the 615.8 nm region.

Mol.	Wavelength [nm]	System	Band	$\log gf$	E_{low} [eV]
CN	615.7850	A–X	(7, 2)	-1.498	1.800
C_2	615.8106	$d^3\Pi_g - a^3\Pi_u$	(0, 2)	-1.652	0.508
CN	615.8109	A–X	(6, 1)	-2.140	1.093
CN	615.8223	A–X	(10, 4)	-1.613	2.066
CN	615.8522	A–X	(9, 4)	-1.959	1.062
CN	615.8796	A–X	(9, 4)	-1.924	1.088

Furthermore, the variation in equivalent width in Fig. 4.11 is another confirmation that models including the molecules reproduce the observations satisfactory.

The fitted oxygen abundances with the disk-centre FTS atlas were $\log \epsilon_{\mathrm{O}} = 8.62$ (3D model), 8.72 (1D HM), 8.61 (1D MARCS). For our own observations at disk-centre the abundance values were higher by about 0.05 dex, difference that can be attributed to the difficulty finding the continuum level. The carbon and nitrogen abundances used to compute the molecular abundances were different for the 3D and 1D models and consistent with the abundances derived from each model from other molecular features. For 1D models the macroturbulence was derived from nearby Fe I lines, and a microturbulence of $\xi_{\mathrm{turb}} = 1.0\,\mathrm{km\,s^{-1}}$ was used.

The molecular blends can help to explain the centre-to-limb variation in this spectral region. As seen in Fig. 4.11, both 1D and 3D models can explain the variations similarly well (although the fitted abundances at disk-centre vary). However, the uncertainty of the molecular line data and the wavelength shift of oxygen make this agreement less convincing. These uncertainties do not allow us to reliably test the line formation across the solar disk and the effects of different models. As for O I 777 nm, we also experimented with NLTE effects and different S_{H}. But for the 615 nm lines the NLTE effects are so weak that with all the mentioned uncertainties, it is not possible at this time to extract any reliable conclusions about, for example, the H I collisional efficiency.

4.4.4. Lines from other species than O I

In Fig. 4.12 we present the centre-to-limb variation of the equivalent width for a few other lines than oxygen included in our observations. The properties of these lines are listed in Table 3.2. Nearby blends have been included for the Si I 615.57 nm and Ca I 616.60 nm. Their wings influence each other, so both of them have been included in each of their line profiles, as is a nearby strong Si I line at 615.51 nm. For the Ca I 616.60 nm line, we also include the very weak O I triplet at 615.60 nm, which influences the line slightly. Data for all the extra blending lines were extracted from the VALD database.

While the agreement between the 3D model and the lines in Fig. 4.12 is generally worse than for the oxygen lines, it is in most cases an improvement over the 1D models. For most of the Fe I lines the 1D models predict a much weaker line at the limb, while the 3D model prediction usually follows the observations. What happens with the Sc II 630.06 nm is very similar with the figure for [O I] 630.03 nm. This is probably because this line of a ionized rare element is not very sensitive to the local temperature. In the case of Si I 615.57 nm, blends are likely to influence the behaviour of the line. This line is in a relatively crowded spectral region. For Fe I 615.93 nm from $\mu \approx 0.4$ to the limb the 1D models predict a decrease in line strength, while the 3D model predicts an increase. The observations in this case seem to follow neither and maintain a constant line strength. But it should be noted that weak blending features on the wings of Fe I 615.93 nm make the continuum level difficult to determine, hence the big uncertainties in equivalent width. The Fe I 629.77 and 615.16 nm lines have a similar variation with μ, which is reasonably reproduced by the 3D model while the 1D models show larger discrepancies and the wrong trend with μ.

At this time we refrain from drawing conclusions about NLTE effects in these lines. However, these may be addressed in the future if there is enough atomic data for these atoms.

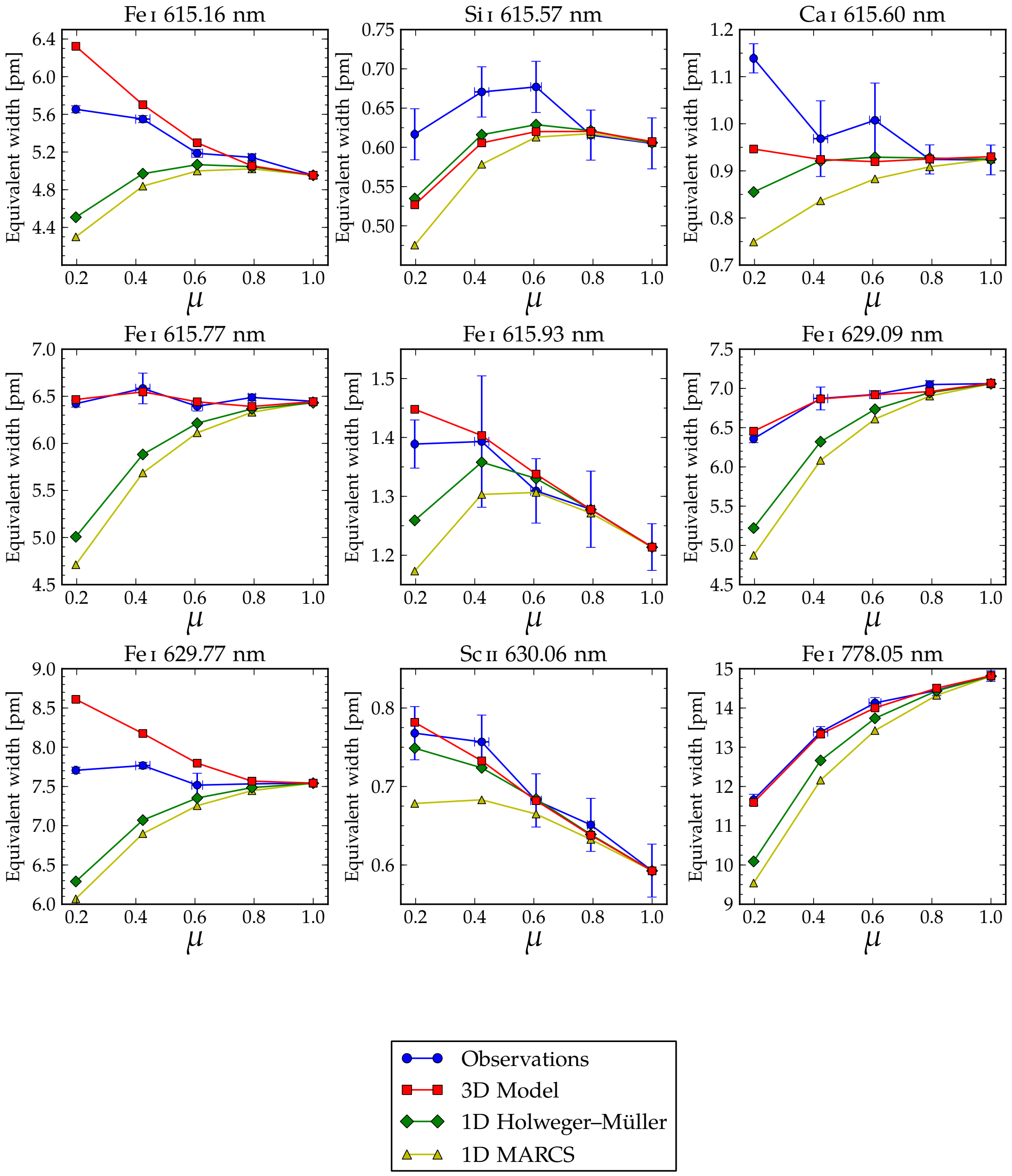

Figure 4.12 Centre-to-limb variations of line equivalent widths. The 1D models were computed with a microturbulence of $\xi_{\rm turb} = 1.0\,{\rm km\,s^{-1}}$ and a macroturbulence extracted from nearby Fe i lines. The abundance of each element has been adjusted so that the models fit the observations at disk-centre. The line profiles of Si i 615.57 nm and Ca i 615.60 nm include weak nearby blends (see text). All the line profiles were computed assuming LTE.

4.5. Conclusions

The study of oxygen lines at different positions in the solar disk has proven very fruitful. From departures of LTE to constraints in blends and line data, the detailed line profiles for different μ values give us a wealth of new information. The relevance of these tests is to ascertain whether the temperature structure of the models can reasonably explain the formation of these lines, and so can be considered reliable for inferring the much debated solar oxygen abundance. Although for abundance analysis the FTS atlases should be the preferred choice, given their superior resolution and S/N, our high-resolution spectra have proven decisive in identifying the shapes and variations of lines and blends over a range of formation temperatures.

Using detailed 3D NLTE radiative transfer, we computed the level populations and synthetic profiles for oxygen lines. The O I 777 nm triplet is of particular interest. These lines suffer from NLTE effects, the size of which is determined by inelastic collisions with electrons and neutral hydrogen. Because of the lack of analytical or experimental data regarding the efficiency of the neutral hydrogen collisions, one has to treat it almost as a free parameter, which the centre-to-limb variation of the lines helps for getting an empirical estimate. In a similar approach to AAF04, we determined the empirical value for the multiplication factor of the classical recipe for hydrogen collisions, S_H. For the 3D model and the 1D Holwer–Müller model, the best fit is for $S_H \approx 0.85$. For the 3D model used by AAF04, we find a lower value. These differences illustrate the model dependency of the centre-to-limb derivation of S_H. The 1D MARCS model does not even reproduce the observed equivalent widths with any value of S_H.

A more decisive test of the 3D and other models for the O I 777 nm lines will have to wait until better data for hydrogen collisions is available. Nevertheless, finding an S_H that describes the observations provides a self-consistent way of determing the extent of the NLTE effects and to extract a reliable value for the oxygen abundance. As seen in Table 4.2, the oxygen abundance varies quickly with the chosen S_H, especially for $0.3 \lesssim S_H \lesssim 3$, making a self-consistent estimate of the hydrogen collisions of paramount importance. The last remaining discrepancy with the empirical S_H approach is that the best-fitting NLTE profiles at disk-centre are slightly narrower and deeper than the observed. It is not clear that this discrepancy can be improved on the model side or whether it is a consequence of using the classical Drawin (1968) formulæ.

The weak 615.81 nm O I line also shows departures from LTE, albeit on a much smaller scale than the 777 nm counterparts. Unfortunately the weakness of the NLTE effects and the presence of blends make it very difficult to estimate S_H from the centre-to-limb variation of this line. When looking at the line profiles, especially as one gets closer to the limb, we find a line blueshift and strength that are inconsistent with the synthetic spectra, when only oxygen is considered. With a high excitation energy, synthetic models indicate that at the limb the oxygen line should be much weaker than observed. However, if one includes a few molecular blends present in the region, the line strength and blueshift effects can almost be reproduced perfectly in the synthetic spectra. At the limb the molecules blended with the oxygen are stronger than the oxygen contribution. Uncertainties in the input data for the molecular lines and continuum placement errors in the observations mean that the results are not precise enough to discern between the different S_{H} for the weak NLTE effects.

Blends also play a determinant role in the [O I] 630.03 nm line. The unresolvable blend with Ni in this line has been a major source of uncertainty in an otherwise good indicator for the oxygen abundance (formed in LTE, relatively independent of temperature). A good knowledge of the Ni I line properties is essential. For that we use the recent measurement of its $\log gf$ value (Johansson et al., 2003) and the recent determination of the nickel abundance for the 3D model (Asplund et al., 2009). Establishing the correct contribution of nickel in the blend will not guarantee a correct determination of the oxygen abundance. Because the oxygen and nickel lines are so close together, a shift in their wavelengths will affect the inferred oxygen abundance, because the fitting procedure will compensate for the quantity of oxygen that best matches the observations. It should be noted that because the nickel abundance is kept fixed, the effect of the wavelength shift on the oxygen abundance is not as significant as if it was allowed to vary (*e.g.*, ALA01): we estimate it to be less than 0.02 dex. In any case, for this line, allowing a wavelength shift in the fitting is not desirable, and a precise absolute wavelength calibration must be obtained. Ayres (2008) makes use of Fe I lines to calibrate the wavelength scale, as the FTS atlas by itself is not precise enough. In this work we used a similar approach of calibration using Fe I lines to ensure the accuracy of the results. The line profile fits for the FTS intensity atlas using the 3D model agree remarkably between model and observations, with less than 0.2% difference for most of the line profile. Since it is not very sensitive to temperature, this line displays a small centre-to-limb variation in strength. Even with the observational uncertainties inherent in such a weak line, we can see that the 3D model provides a very good description of the observations. This agreement gives us confidence in the 3D model, confirming its robustness at inferring the oxygen abundance from this line.

Overall, we find that the 3D model reproduces the observations very well. Despite its one-dimensional nature not allowing for the most accurate shape of the observed profiles, the Holweger–Müller model also reproduces the observed equivalent widths, which is not surprising because it is semi-empirical. The 1D theoretical MARCS model falls short of its description of centre-to-limb variation of the O I 777 nm and [O I] 630.03 nm lines, probably because its temperature structure departs from the solar temperature structure.

Using the best fitting $S_{\mathrm{H}} = 0.85$ and abundance results from disk-centre line profile fits, we infer an oxygen abundance of 8.68 for the 3D model using the 777 nm lines. This value can be compared to the value of 8.66 derived from the [O I] 630.03 nm line and the value of 8.62 derived from the O I 615.82 nm line (dependent on the assumed strength of the molecular lines). The good performance of the 3D model in reproducing not only the observed line shapes and shifts, but also the centre-to-limb variation of the oxygen lines, is a good indicator of the quality of the inferred abundances.

CHAPTER 5

Summary and future outlook

Can one trust the 3D model atmospheres to infer the chemical composition of stars? This is the question of this thesis. The answer, in short, is yes. But how can one determine if the models are appropriate for chemical composition studies?

The photospheric abundances are derived using spectral lines of various elements. A synthetic spectrum, calculated using a model of the star's atmosphere, is then compared with the observed spectrum and the abundance adjusted to fit the observations. Several uncertainties surround this procedure: from the atomic and molecular line data to observational uncertainties. But the uncertainties this thesis is concerned with are the model uncertainties. A reliable determination of the element abundances can only happen if the thermal and dynamic structures of the model are realistic, if they are an accurate description of the star's photosphere. One needs additional information to verify if this is the case. The Sun is the ideal probe for this type of testing. While it is not currently possible to measure its temperature profile directly, its surface being resolved in great detail and at different viewing angles allows several tests of the photosphere, which can be used to constrain the models. Several of this tests were performed, and are summarized below.

While it is of great importance to settle the debate on the solar chemical composition, it is also very interesting to apply the new model atmospheres to other stars. Using the Sun as a test-bench has thus a dual purpose. If the solar models are realistic, then one expects them to also be realistic for other late-type, cool stars.

The tests undertaken in this thesis can be divided in two groups: tests of the temperature structure and tests of the line formation. The former, detailed in Chapter 2, look at the temperature gradient and absolute temperatures in the solar photosphere. The latter, detailed in Chapters 3 and 4, test the model predictions on how spectral lines are formed in a variety of conditions and different depths in the photosphere.

5.1. Chapter 2

In Chapter 2 several solar models were tested, including the theoretical 3D LTE and 1D NLTE models, as well as the 1D Holweger–Müller semi-empirical model. The tests include the centre-to-limb variation (CLV) of the continuum intensity, an indicator of the photospheric temperature gradient and the absolute continuum fluxes, which provide an absolute temperature scale.

For the continuum CLV an excellent agreement between the 3D model and the observations is found, surpassing even the Holweger–Müller model, and significantly better than the 1D theoretical models.

For the continuum fluxes all the models show a good agreement with the observations. The 3D model predicts a slightly smaller continuum flux, but reproduces the shape of the flux distribution well. The Holweger–Müller seems to have the correct flux, but the flux distribution is not so accurate.

For all the tests the solar 1D NLTE models are found to be not very different from the 1D LTE models, which confirms LTE as a good approximation for the solar photosphere. The 1D NLTE models are only tested in this chapter. The last test performed in Chapter 2 is the distribution of continuum intensities in the solar granulation, which by definition can only be tested for the 3D model. The results show that the model predictions agree very well with the observations and also with the CO^{5}BOLD model, a 3D model developed independently by another group (B. Freytag, H.-G. Ludwig, M. Steffen, S. Wedemeyer-Böhm et al.). In sum, the tests conducted in Chapter 2 indicate that the temperature structure of the 3D model is very realistic and an improvement over 1D theoretical models.

5.2. Chapter 3

In Chapter 3 the tests shift towards line formation at high spatial resolution, in particular of oxygen lines. Oxygen is determinant in the downward revision of the solar metallicity, so it is of particular interest to compare the 3D model predictions with the observations for oxygen lines.

The solar abundances are derived using high-quality spectral atlases of the Sun, that represent the mean spatial and temporal Sun. Asplund et al. (2004) show that the 3D model reproduces these mean spectra very accurately. But one question that can be asked is if it also reproduces the lines in detail across the solar granulation, and not just their mean properties. To attack this problem new solar data was obtained. Using the Swedish 1-m Solar Telescope, high spatial and spectral resolution observations of oxygen and other lines were obtained at several positions in the solar disk. The quality of the data compares very favourably with other data obtained with the same instrument. The oxygen lines tested were the O I 615.81 nm line, the [O I] 630.03 nm line and the O I 777 nm triplet. Because the latter are known to show departures from LTE, 3D NLTE calculations were performed for the oxygen line formation.

With the new observations several tests were performed. These included testing the dynamics of the photosphere through the line shifts, asymmetries and widths, as well as of the line formation by looking at the distribution of line strengths over the solar granulation. Overall, the 3D model predictions are in excellent agreement with the observations. This is particularly true for the oxygen lines. In some of the tests of weak lines it was difficult to obtain a clear answer, as noise dominated the observations. For most lines the 3D model accurately predicts the variation of line strengths, shifts and shapes over the granulation.

5.3. Chapter 4

In Chapter 4 the observations detailed in Chapter 3 are used, but to study the centre-to-limb variation (CLV) of the spatial and temporal mean spectra. Again, this was used as a probe for the line formation of important oxygen lines used to derive the solar oxygen abundance. The CLV of the lines looks at the line formation at different depths in the photosphere, which all contribute for the disk-centre or disk-averaged mean spectra used to derive the solar abundances.

For the oxygen NLTE calculations, in particular for the O I 777 nm triplet, there is some uncertainty regarding the efficiency of collisions with H I. These are usually taken from classical expressions and scaled by a factor S_{H}. The scaling factor is crucial for an accurate abundance, as it influences the line strengths significantly. Building up on the work of Allende Prieto et al. (2004), the CLV of the O I 777 nm lines is used to empirically derive this scaling factor. For the 3D model we find a very good fit for $S_{\mathrm{H}} \approx 0.85$.

For the [O I] 630.03 nm line LTE is a very good approximation. However, this line is blended with a Ni I line. These lines are carefully modeled, properly accounting for the Ni contribution, with a precise wavelength calibration and using the most recent atomic data and Ni abundance. For the CLV the best agreement is found with the Holweger–Müller model, although he 3D model also performs well and within the observational error bars. However, it is when fitting the line profiles that the 3D model shines. Without the free parameters of micro- and macro-turbulence, it reproduces the observed line profile very well, with differences well under 0.2% for most of the disk-centre profile.

The O I 615.85 nm line is known to show departures from LTE, albeit very small. With the CLV it is found that the observed feature is much stronger than all the model predictions at the limb, which cannot be explained by the oxygen line alone. After some experimentation it was found that molecular features become very significant in this region at the limb. Including nearby CN and C_2 lines in the spectral synthesis, the observed CLV and line profiles can be reproduced very well by the 3D and other models. But this comes at the cost of uncertainties in the molecular lines.

Overall the agreement of the 3D model predictions with the observed line profiles and CLV of the oxygen lines. Its predictions are also good for most of the studied lines from other elements, where it consistently performs better than the 1D theoretical and semi-empirical models.

5.4. Where to, from here?

The tests undertaken here have highlighted the great degree of realism present in the 3D solar photosphere models. They imply a realistic temperature structure and dynamics of these models, which confirms their usefulness for inferring chemical abundances. Their use in chemical composition analyses represents a major step forward in the modeling of stellar atmospheres. And in the modeling of the quiet solar photosphere, which is now believed to be known in great detail.

Having established that the 3D models provide a good description of the solar photosphere, the next step is to extend the 3D modeling to other stars. This is being done, and there are currently two groups developing grids of 3D model atmospheres for a range of temperatures, gravities and metallicities (Trampedach, 2007; Ludwig et al., 2009). Of particular interest are stars where the 3D effects (*i.e.*, the differences between 1D and 3D theoretical models) are considerable. One such example are metal-poor red giant stars. As evidenced by the recent work of Collet et al. (2006) and Collet et al. (2007), the predicted 3D mean temperature structure can be lower than the 1D models by several hundreds of degrees, which results in lower abundances with the 3D models (up to −1 dex). These results, together with the increasing availability of 3D models for more types of stars, indicate interesting times ahead for stellar atmospheres, with far-reaching consequences as several indicators of the galactic chemical evolution are revisited.

Yet these efforts can be hampered by NLTE effects in the structure of stellar photospheres. The tests with the 1D NLTE solar models show that the effect of departures from LTE on the structure of solar models is small. While reassuring for the solar 3D LTE models used, these results mean that the Sun is not the ideal test-bench for the NLTE effects on the photospheric structure, and shortcomings in the modeling cannot be identified so easily. However, the photospheric structure is known to be affected by NLTE effects for other stars, particularly metal-poor red giant stars (Short & Hauschildt, 2006). Accounting for the 3D *and* NLTE on the photospheric structure will require a self-consistent relaxation of both the LTE and convection approximations, which is not yet possible due to stringent computational requirements. From the few individual elements for which the radiative transfer has been solved in 3D NLTE, it is known there is some interplay between the 3D and NLTE effects, and that a correction for each cannot always be separately applied. Thus, a consistent simultaneous treatment of the 3D and NLTE effects is necessary. Not yet available, these 3D NLTE models of stellar photospheres can be seen as the 'holy grail' of stellar atmospheres, the last step in overcoming the approximations of classical models.

REFERENCES

Allende Prieto, C., Asplund, M., & Fabiani Bendicho, P. 2004, A&A, 423, 1109 (AAF04)

Allende Prieto, C., Asplund, M., García López, R. J., & Lambert, D. L. 2002, ApJ, 567, 544

Allende Prieto, C., Lambert, D. L., & Asplund, M. 2001, ApJ, 556, L63 (ALA01)

Altrock, R. C. 1968, Sol. Phys., 5, 260

Anders, E. & Grevesse, N. 1989, Geochim. Cosmochim. Acta, 53, 197

André, M. K., Oliveira, C. M., Howk, J. C., et al. 2003, ApJ, 591, 1000

Anstee, S. D. & O'Mara, B. J. 1995, MNRAS, 276, 859

Asplund, M. 2005, ARA&A, 43, 481

Asplund, M., Carlsson, M., & Botnen, A. V. 2003, A&A, 399, L31

Asplund, M., Grevesse, N., & Sauval, A. J. 2005a, in Astronomical Society of the Pacific Conference Series, Vol. 336, Cosmic Abundances as Records of Stellar Evolution and Nucleosynthesis, ed. T. G. Barnes, III & F. N. Bash, 25–+

Asplund, M., Grevesse, N., Sauval, A. J., Allende Prieto, C., & Blomme, R. 2005b, A&A, 431, 693

Asplund, M., Grevesse, N., Sauval, A. J., Allende Prieto, C., & Kiselman, D. 2004, A&A, 417, 751

Asplund, M., Grevesse, N., Sauval, J., & Scott, P. 2009, ARA&A, 47, 481

Asplund, M., Nordlund, Å., Trampedach, R., Allende Prieto, C., & Stein, R. F. 2000a, A&A, 359, 729

Asplund, M., Nordlund, Å., Trampedach, R., & Stein, R. F. 2000b, A&A, 359, 743

Ayres, T. R. 1998, in IAU Symposium, Vol. 185, New Eyes to See Inside the Sun and Stars, ed. F.-L. Deubner, J. Christensen-Dalsgaard, & D. Kurtz, 403–+

Ayres, T. R. 2008, ApJ, 686, 731

Ayres, T. R., Plymate, C., & Keller, C. U. 2006, ApJS, 165, 618

Bahcall, J. N., Basu, S., Pinsonneault, M., & Serenelli, A. M. 2005, ApJ, 618, 1049

Balthasar, H., Grosser, H., Schroeter, C., & Wiehr, E. 1990, A&A, 235, 437

Barklem, P. S. 2007, A&A, 462, 781

Barklem, P. S., Belyaev, A. K., & Asplund, M. 2003, A&A, 409, L1

Barklem, P. S. & O'Mara, B. J. 1997, MNRAS, 290, 102

Barklem, P. S., O'Mara, B. J., & Ross, J. E. 1998, MNRAS, 296, 1057

Basu, S. & Antia, H. M. 2008, Phys. Rep., 457, 217

Botnen, A. 1997, Master's thesis, Inst. Theor. Astrophys. Oslo (1997)

Botnen, A. & Carlsson, M. 1999, in Astrophysics and Space Science Library, Vol. 240, Numerical Astrophysics, ed. S. M. Miyama, K. Tomisaka, & T. Hanawa, 379–+

Brault, J. W. & Neckel, H. 1987, ftp://ftp.hs.uni-hamburg.de/pub/outgoing/FTS-Atlas

Brott, I. & Hauschildt, P. H. 2005, in ESA Special Publication, Vol. 576, The Three-Dimensional Universe with Gaia, ed. C. Turon, K. S. O'Flaherty, & M. A. C. Perryman, 565–+

Byrd, R. H., Lu, P., & Nocedal, J. 1995, SIAM Journal on Scientific and Statistical Computing, 16, 1190

Caffau, E., Ludwig, H.-G., Steffen, M., et al. 2008a, A&A, 488, 1031

Caffau, E., Sbordone, L., Ludwig, H.-G., et al. 2008b, A&A, 483, 591

Carlsson, M., Stein, R. F., Nordlund, Å., & Scharmer, G. B. 2004, ApJ, 610, L137

Centeno, R. & Socas-Navarro, H. 2008, ApJ, 682, L61

Claas, W. J. 1951, Rech. Astr. Obs. Utrecht, Vol. 12, Part 1

Colina, L., Bohlin, R. C., & Castelli, F. 1996, AJ, 112, 307

Collados, M. & Vazquez, M. 1987, A&A, 180, 223

Collet, R., Asplund, M., & Trampedach, R. 2006, ApJ, 644, L121

Collet, R., Asplund, M., & Trampedach, R. 2007, A&A, 469, 687

Collet, R., Asplund, M., & Trampedach, R. 2008, Memorie della Societa Astronomica Italiana, 79, 649

Cortie, A. L. 1897, MNRAS, 57, 141

Cunto, W., Mendoza, C., Ochsenbein, F., & Zeippen, C. J. 1993, A&A, 275, L5+

Danilovic, S., Gandorfer, A., Lagg, A., et al. 2008, A&A, 484, L17

Drawin, H. W. 1968, Zeitschrift fur Physik, 211, 404

Eriksson, K. & Toft, S. C. 1979, A&A, 71, 178

Eriksson, K. B. S. 1965, Ark. Fys., 30, 199

Fabbian, D., Asplund, M., Barklem, P. S., Carlsson, M., & Kiselman, D. 2009, A&A, 500, 1221

Fontenla, J. M., Avrett, E. H., & Loeser, R. 1993, ApJ, 406, 319

Freytag, B. & Höfner, S. 2008, A&A, 483, 571

Freytag, B., Steffen, M., & Dorch, B. 2002, Astronomische Nachrichten, 323, 213

Goldberg, L. & Aller, L. H. 1943, Atoms, stars and nebulae

Goldberg, L., Muller, E. A., & Aller, L. H. 1960, ApJS, 5, 1

Grevesse, N. & Noels, A. 1993, Physica Scripta Volume T, 47, 133

Grevesse, N. & Sauval, A. J. 1998, Space Science Reviews, 85, 161

Grevesse, N., Sauval, A. J., & van Dishoeck, E. F. 1984, A&A, 141, 10

Gudiksen, B. V. & Nordlund, Å. 2005, ApJ, 618, 1020

Gustafsson, B., Bell, R. A., Eriksson, K., & Nordlund, Å. 1975, A&A, 42, 407

Gustafsson, B., Edvardsson, B., Eriksson, K., et al. 2008, A&A, 486, 951

Hanslmeier, A., Mattig, W., & Nesis, A. 1990, A&A, 238, 354

Hanslmeier, A., Nesis, A., & Mattig, W. 1993, A&A, 270, 516

Hauschildt, P. H. & Baron, E. 1999, Journal of Computational and Applied Mathematics, 109, 41

Holweger, H. 1967, Zeitschrift fur Astrophysik, 65, 365

Holweger, H. & Müller, E. A. 1974, Sol. Phys., 39, 19

Hummer, D. G., Berrington, K. A., Eissner, W., et al. 1993, A&A, 279, 298

Johansson, S., Litzén, U., Lundberg, H., & Zhang, Z. 2003, ApJ, 584, L107

Kiselman, D. 1991, A&A, 245, L9

Kiselman, D. 1993, A&A, 275, 269

Kiselman, D. 1994, A&AS, 104, 23

Kiselman, D. 1998, A&A, 333, 732

Kiselman, D. & Asplund, M. 2003, in IAU Symposium, Vol. 210, Modelling of Stellar Atmospheres, ed. N. Piskunov, W. W. Weiss, & D. F. Gray, 62P–+

Kiselman, D. & Nordlund, Å. 1995, A&A, 302, 578

Kochukhov, O., Freytag, B., Piskunov, N., & Steffen, M. 2007, in IAU Symposium, Vol. 239, IAU Symposium, ed. T. Kuroda, H. Sugama, R. Kanno, & M. Okamoto, 68–70

Koesterke, L., Allende Prieto, C., & Lambert, D. L. 2008, ApJ, 680, 764

Kopp, G., Lawrence, G., & Rottman, G. 2005, Sol. Phys., 230, 129

Kupka, F. G., Ryabchikova, T. A., Piskunov, N. E., Stempels, H. C., & Weiss, W. W. 2000, Baltic Astronomy, 9, 590

Kurucz, R. L. 2005a, Memorie della Societa Astronomica Italiana Supplement, 8, 14

Kurucz, R. L. 2005b, Memorie della Societa Astronomica Italiana Supplement, 8, 189

Kurucz, R. L., Furenlid, I., Brault, J., & Testerman, L. 1984, Solar flux atlas from 296 to 1300 nm (National Solar Observatory Atlas, Sunspot, New Mexico: National Solar Observatory, 1984)

Kučera, A., Rybák, J., & Wöhl, H. 1995, A&A, 298, 917

Lambert, D. L. 1968, MNRAS, 138, 143

Lambert, D. L. 1978, MNRAS, 182, 249

Lambert, D. L. 1993, Physica Scripta Volume T, 47, 186

Langangen, Ø., Carlsson, M., Rouppe van der Voort, L., & Stein, R. F. 2007, ApJ, 655, 615

Ludwig, H.-G., Caffau, E., Steffen, M., et al. 2009, ArXiv e-prints

Maltby, P., Avrett, E. H., Carlsson, M., et al. 1986, ApJ, 306, 284

Meléndez, J. & Asplund, M. 2008, A&A, 490, 817

Mihalas, D., Dappen, W., & Hummer, D. G. 1988, ApJ, 331, 815

Müller, E. A., Baschek, B., & Holweger, H. 1968, Sol. Phys., 3, 125

Nave, G., Johansson, S., Learner, R. C. M., Thorne, A. P., & Brault, J. W. 1994, ApJS, 94, 221

Neckel, H. & Labs, D. 1994, Sol. Phys., 153, 91

Nissen, P. E., Primas, F., Asplund, M., & Lambert, D. L. 2002, A&A, 390, 235

Nordlund, Å. 1982, A&A, 107, 1

Nordlund, Å. 1984, in Small-Scale Dynamical Processes in Quiet Stellar Atmospheres, ed. S. L. Keil, 174–+

Nordlund, Å. & Galsgaard, K. 1995, A 3D MHD Code for Parallel Computers, Tech. rep., Astronomical Observatory, Copenhagen University

Pereira, T. M. D., Asplund, M., & Trampedach, R. 2008, in Precision Spectroscopy in Astrophysics, ed. N. C. Santos, L. Pasquini, A. C. M. Correia, & M. Romaniello, 313–314

Pierce, A. K. & Slaughter, C. D. 1977, Sol. Phys., 51, 25

Pierce, A. K., Slaughter, C. D., & Weinberger, D. 1977, Sol. Phys., 52, 179

Piskunov, N. E., Kupka, F., Ryabchikova, T. A., Weiss, W. W., & Jeffery, C. S. 1995, A&AS, 112, 525

Puschmann, K., Vázquez, M., Bonet, J. A., Ruiz Cobo, B., & Hanslmeier, A. 2003, A&A, 408, 363

Ralchenko, Y., Kramida, A., Reader, J., & NIST ASD Team. 2009, NIST Atomic Spectra Database (version 3.1.5), http://physics.nist.gov/asd3

Rosman, K. J. R. & Taylor, P. D. P. 1998, Pure Appl. Chem., 70, 217

Russell, H. N. 1929, ApJ, 70, 11

Rutten, R. J. 1998, Space Science Reviews, 85, 269

Scharmer, G. B., Bjelksjo, K., Korhonen, T. K., Lindberg, B., & Petterson, B. 2003a, in Presented at the Society of Photo-Optical Instrumentation Engineers (SPIE) Conference, Vol. 4853, Innovative Telescopes and Instrumentation for Solar Astrophysics. Edited by Stephen L. Keil, Sergey V. Avakyan . Proceedings of the SPIE, Volume 4853, pp. 341-350 (2003)., ed. S. L. Keil & S. V. Avakyan, 341–350

Scharmer, G. B., Dettori, P. M., Lofdahl, M. G., & Shand, M. 2003b, in Presented at the Society of Photo-Optical Instrumentation Engineers (SPIE) Conference, Vol. 4853, Innovative Telescopes and Instrumentation for Solar Astrophysics. Edited by Stephen L. Keil, Sergey V. Avakyan . Proceedings of the SPIE, Volume 4853, pp. 370-380 (2003)., ed. S. L. Keil & S. V. Avakyan, 370–380

Scott, P., Asplund, M., Grevesse, N., & Sauval, A. J. 2009, ApJ, 691, L119

Serenelli, A., Basu, S., Ferguson, J., & Asplund, M. 2009, submitted to ApJ

Short, C. I. & Hauschildt, P. H. 2005, ApJ, 618, 926

Short, C. I. & Hauschildt, P. H. 2006, ApJ, 641, 494

Short, C. I. & Hauschildt, P. H. 2009, ApJ, 691, 1634

Skartlien, R. 2000, ApJ, 536, 465

Sneden, C., Johnson, H. R., & Krupp, B. M. 1976, ApJ, 204, 281

Socas-Navarro, H. & Norton, A. A. 2007a, ApJ, 660, L153

Socas-Navarro, H. & Norton, A. A. 2007b, ApJ, 660, L153

Sordo, R., Vallenari, A., Bouret, J.-C., et al. 2009, Memorie della Societa Astronomica Italiana, 80, 103

Spickler, P. T., Benner, D. C., & Russel, III, J. M. 1996, Sol. Phys., 165, 23

Steenbock, W. & Holweger, H. 1984, A&A, 130, 319

Stein, R. F. & Nordlund, Å. 1998, ApJ, 499, 914

Storey, P. J. & Zeippen, C. J. 2000, MNRAS, 312, 813

Thuillier, G., Floyd, L., Woods, T. N., et al. 2004, Advances in Space Research, 34, 256

Trampedach, R. 2007, in American Institute of Physics Conference Series, Vol. 948, Unsolved Problems in Stellar Physics: A Conference in Honor of Douglas Gough, ed. R. J. Stancliffe, G. Houdek, R. G. Martin, & C. A. Tout, 141–148

Trujillo Bueno, J. & Shchukina, N. 2009, ApJ, 694, 1364

Uitenbroek, H., Tritschler, A., & Rimmele, T. 2007, ApJ, 668, 586

Unsöld, A. 1948, Zeitschrift fur Astrophysik, 24, 306

Unsöld, A. 1955, Physik der Sternatmospharen, MIT besonderer Berucksichtigung der Sonne. (Berlin, Springer, 1955. 2. Aufl.)

Vernazza, J. E., Avrett, E. H., & Loeser, R. 1981, ApJS, 45, 635

Vögler, A., Bruls, J. H. M. J., & Schüssler, M. 2004, A&A, 421, 741

Wedemeyer-Böhm, S. & Rouppe van der Voort, L. 2009, A&A, 503, 225

Willson, R. C. & Hudson, H. S. 1988, Nature, 332, 810

Appendices

APPENDIX A

Results for the old 3D model

The analysis undertaken in this thesis concerns the new improved 3D model of Trampedach et al. (in preparation). Because it was available from the start of this thesis, most of the analysis was also performed on the 3D model of Asplund et al. (2000a), hereafter the 'old' 3D model. The main differences between these two models are the treatment of radiative transfer (number of opacity bins, old model lacked multi-group opacity binning), more recent opacities and the use of improved codes.

For reference, the figures from the analysis with the old 3D model are reproduced here. They are shown in the same order as they appear in this thesis for the new 3D model. Below they are ordered by the chapter in which the original figures appear. The analysis performed on the old 3D model is not as complete as for the new 3D model. The discrepancies are listed below. Nevertheless, it still encompasses the bulk of the tests made to the new 3D model.

A.1. From Chapter 2

Here some figures of Chapter 2 are reproduced for the old 3D model. In some of the figures below, where several models appear in the legends, the '3D Model' description corresponds to the old 3D model. Not all tests were carried out with the same amount of the detail for this 3D model.

The absolute flux calculations for the old 3D model were performed with an older version of the radiative transfer code. The new version was used to compute the results for the new 3D model and for the 1D models, and includes extra sources of continuum opacity. These have the effect of decreasing the flux in the ultraviolet and in the peak of the distribution. Thus, when comparing the old 3D model with the 1D models in Fig. A.5 there is a significant difference for $\lambda < 400$ nm, that is mostly due to the lack of opacity in the old code rather than a difference in the models.

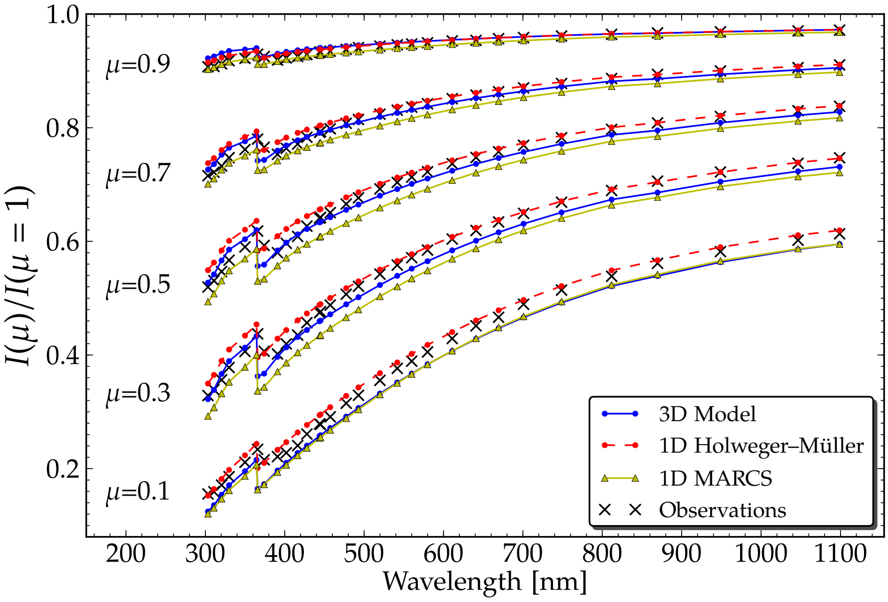

Figure A.1 Same as the top panel of Fig. 2.3, but for the old 3D model.

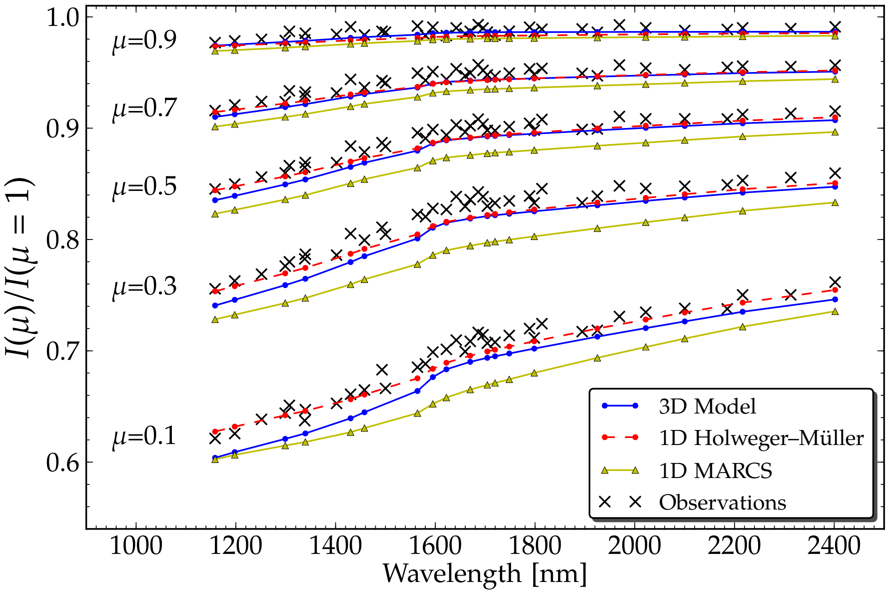

Figure A.2 Same as the top panel of Fig. 2.4, but for the old 3D model.

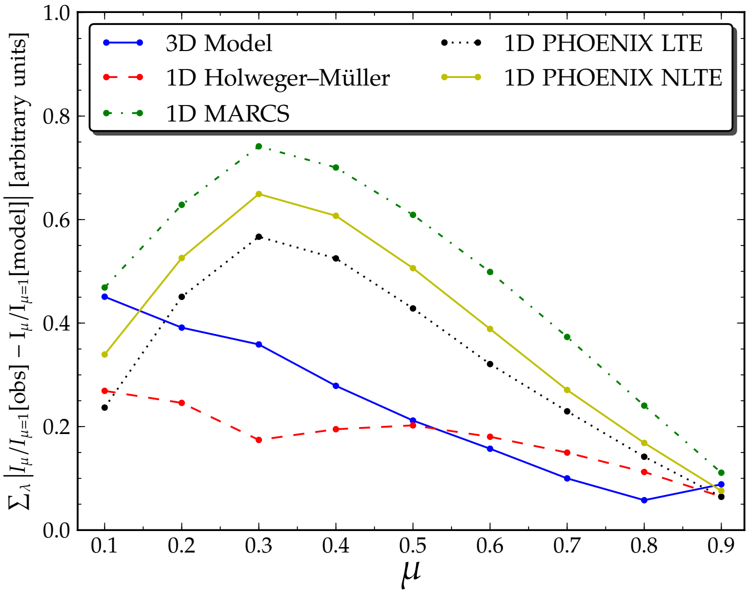

Figure A.3 Same as Fig. 2.5, but for the old 3D model.

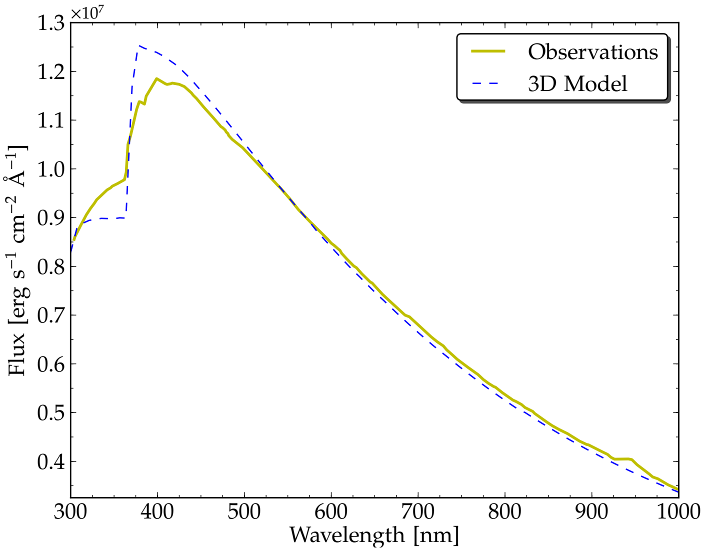

Figure A.4 Same as the top panel of Fig. 2.7, but for the old 3D model. The old 3D model has been evaluated a smaller number of wavelength points.

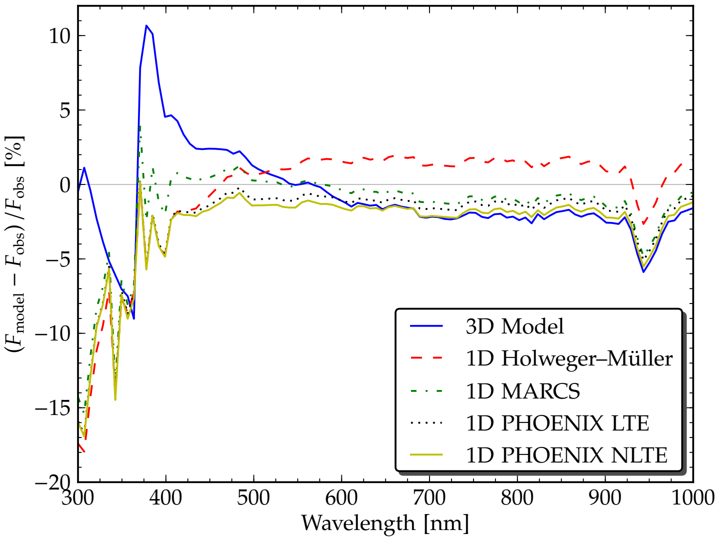

Figure A.5 Same as the top panel of Fig. 2.8, but for the old 3D model. The old 3D model has been evaluated a smaller number of wavelength points.

A.2. From Chapter 3

Here some figures of Chapter 3 are reproduced for the old 3D model. In this analysis, again for saving computational time, the old 3D model predictions were computed for less snapshots (five snapshots in LTE and four in NLTE, compared with 20 and 10 respectively in Chapter 3). While this does not affect the results significantly, it can be noticed in some of the figures that the contours for the old 3D model cover a smaller area than the observations. This is because with only five snapshots the statistical significance is smaller and the two-dimensional histograms occupy a smaller area. Also in Figs. A.11 and A.12, the results for the O I 777 nm lines are shown for LTE, instead of NLTE as in Chapter 3.

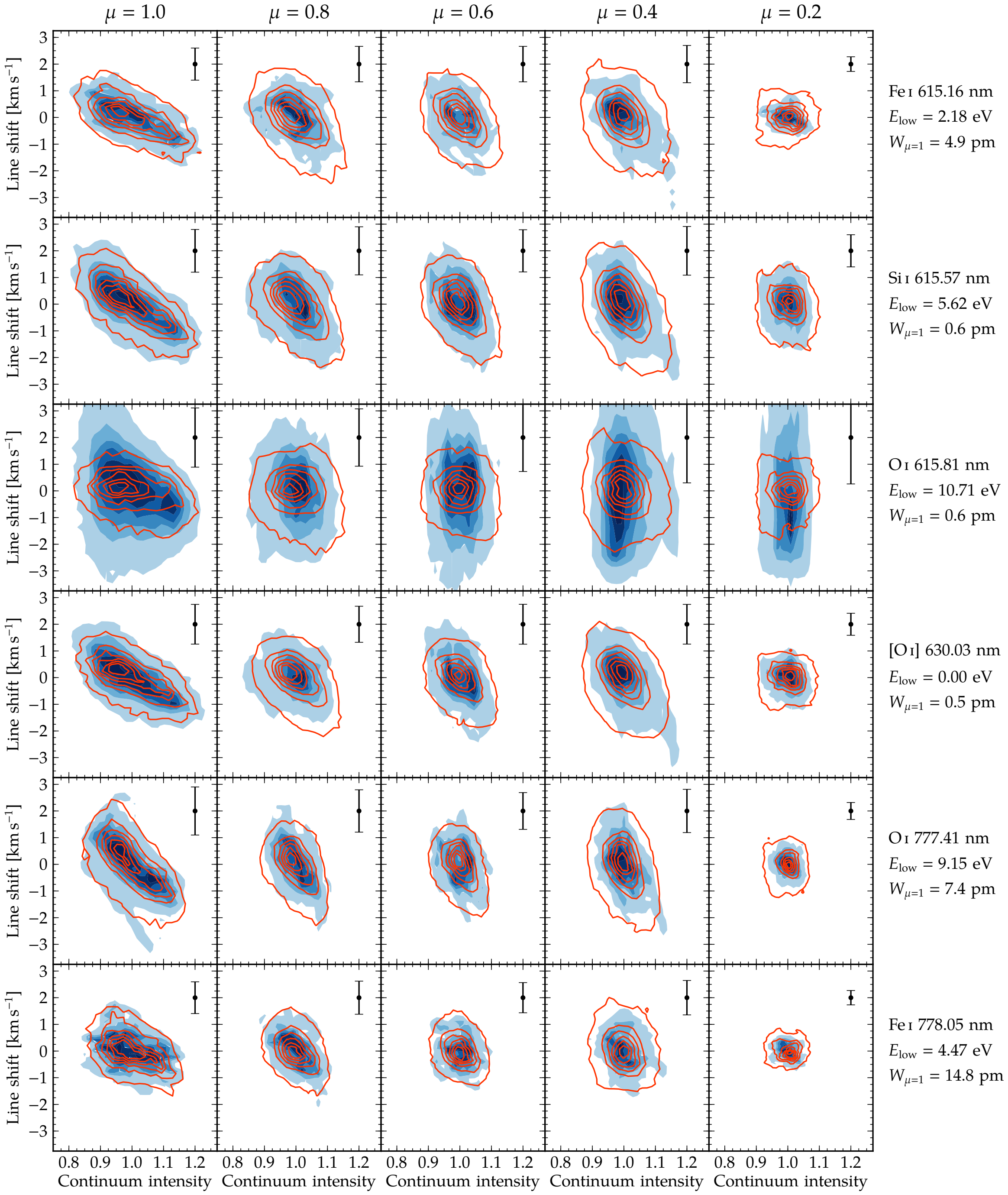

Figure A.6 Same as Fig. 3.7, but for the old 3D model.

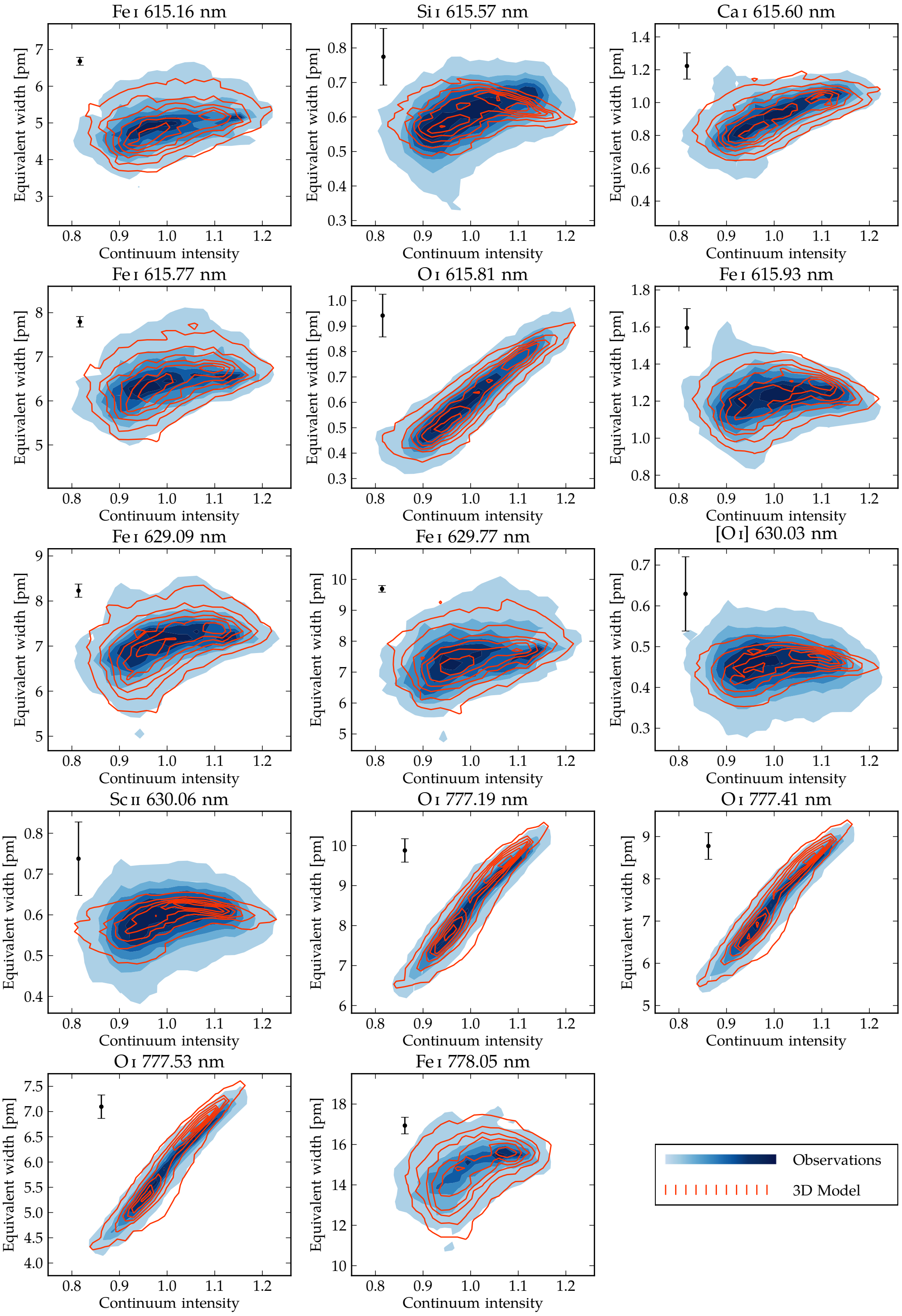

Figure A.7 Same as Fig. 3.8, but for the old 3D model.

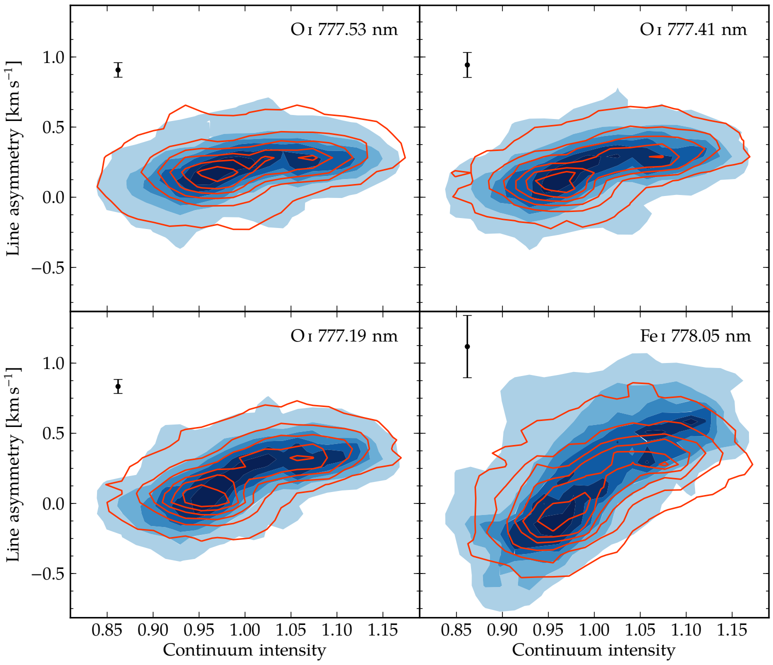

Figure A.8 Same as Fig. 3.9, but for the old 3D model.

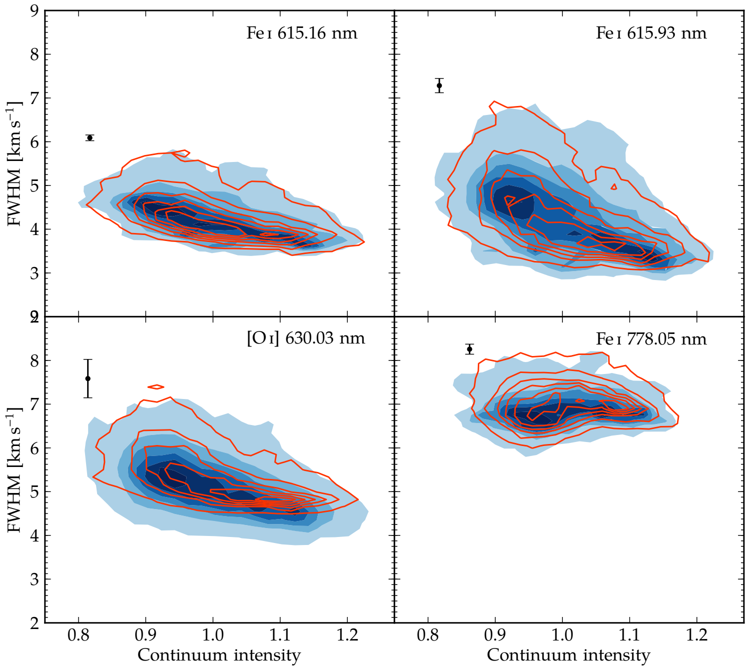

Figure A.9 Same as Fig. 3.11, but for the old 3D model.

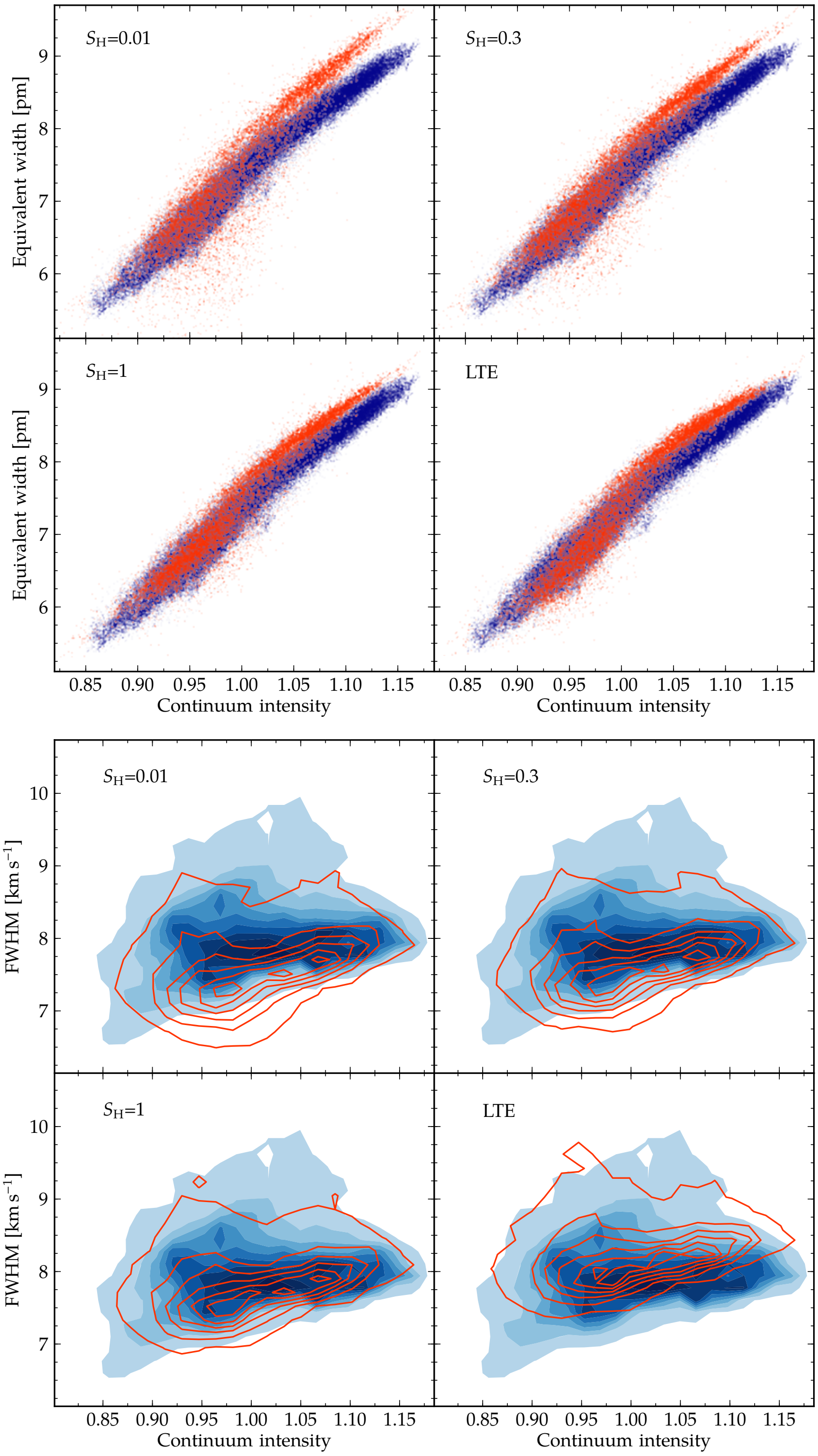

Figure A.10 Same as Fig. 3.12, but for the old 3D model.

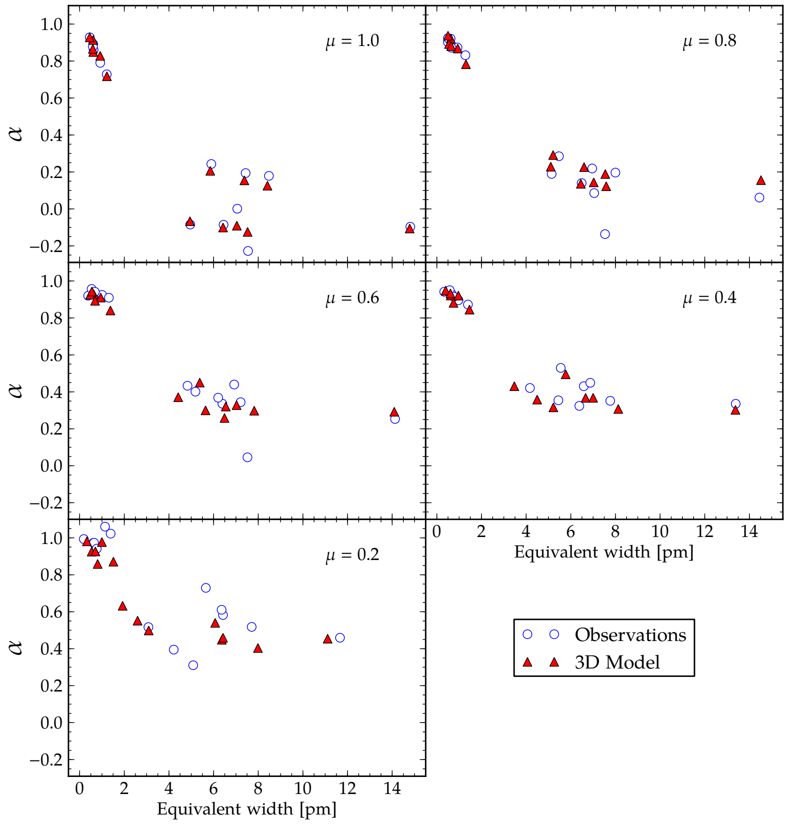

Figure A.11 Same as Fig. 3.13, but for the old 3D model. *Important note:* for the O I 777 nm lines the results here are shown for LTE, whereas in Fig. 3.13 the NLTE ($S_H = 1$) results are shown.

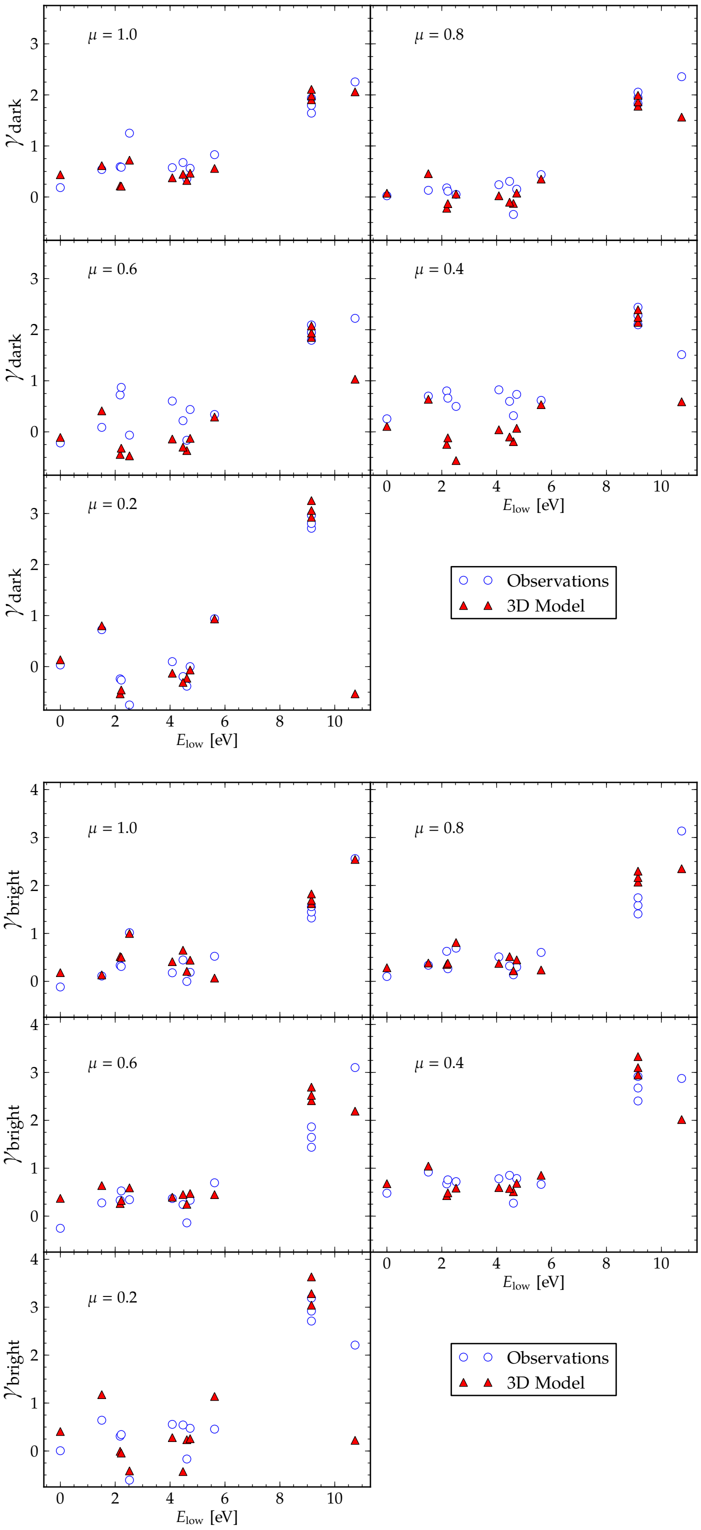

Figure A.12 Same as Fig. 3.14, but for the old 3D model. *Important note:* for the O I 777 nm lines the results here are shown for LTE, whereas in Fig. 3.14 the NLTE ($S_H = 1$) results are shown.

A.3. From Chapter 4

Here some figures of Chapter 4 are reproduced for the old 3D model. The main difference in this analysis to the old 3D model is that the NLTE calculations were carried out for a smaller number of S_H scaling factors. Here only six values were used, whereas Chapter 4 has eight. The rest of the analysis was performed identically.

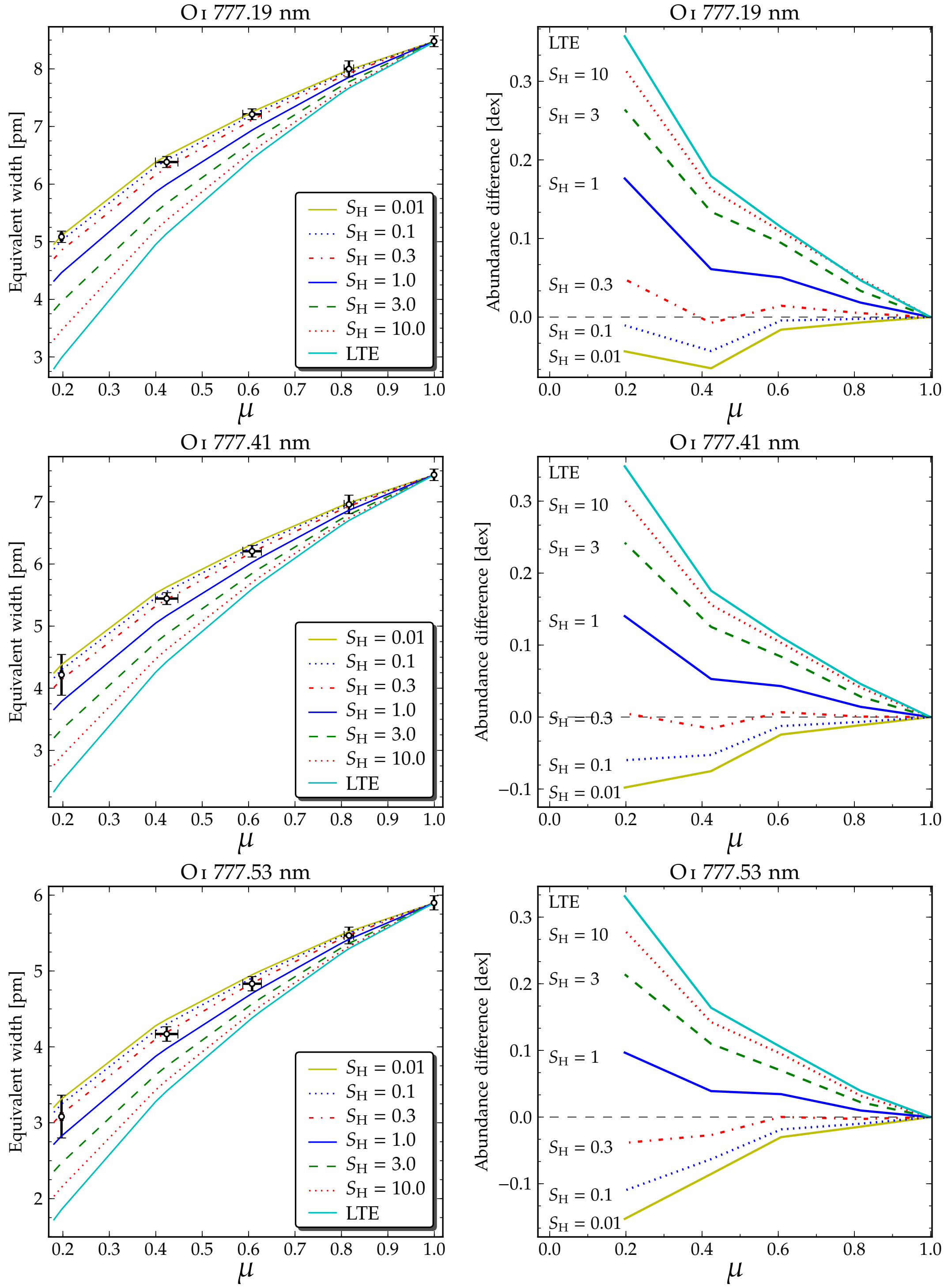

Figure A.13 Same as Fig. 4.4, but for the old 3D model.

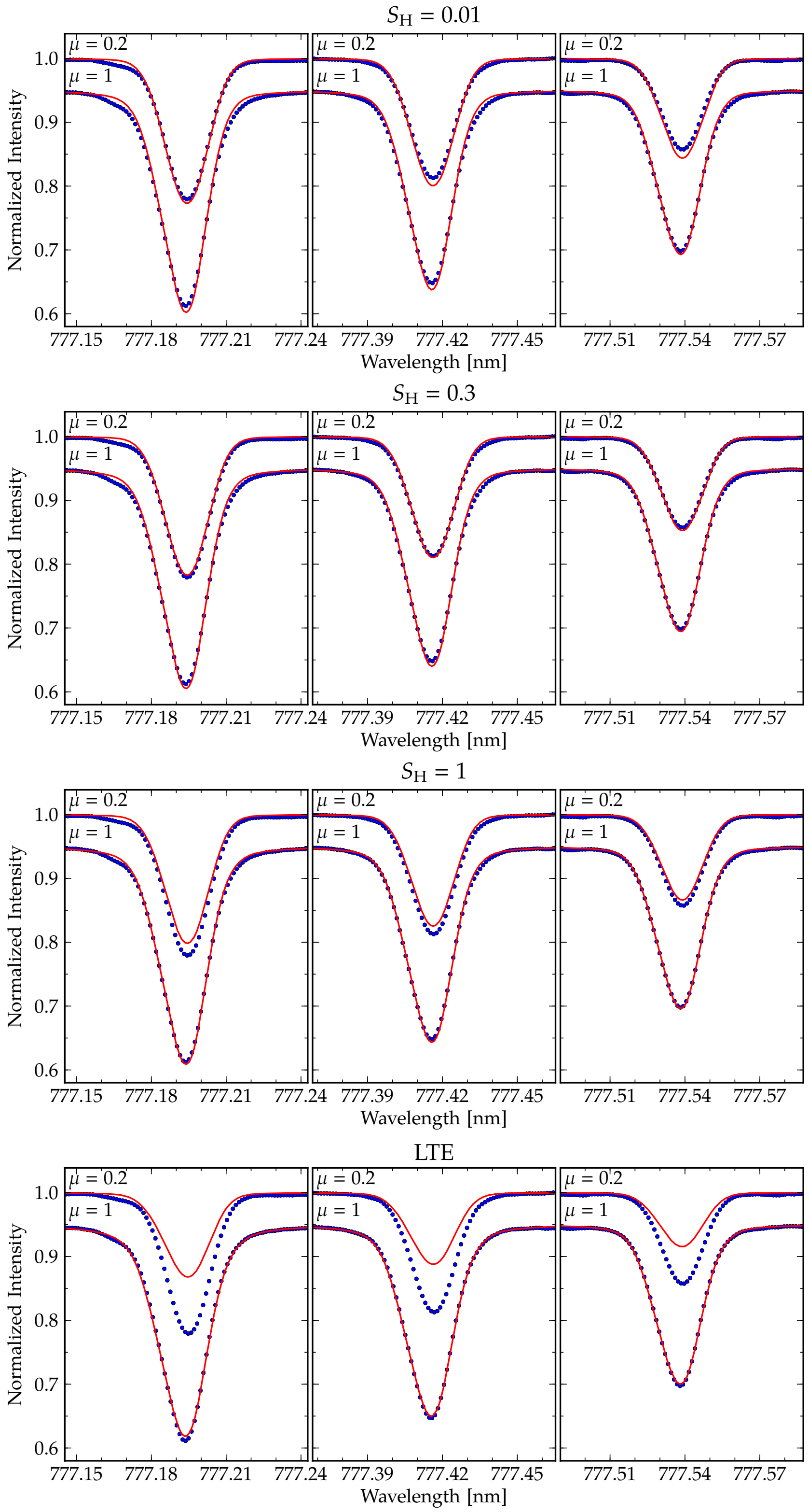

Figure A.14 Same as Fig. 4.6, but for the old 3D model.

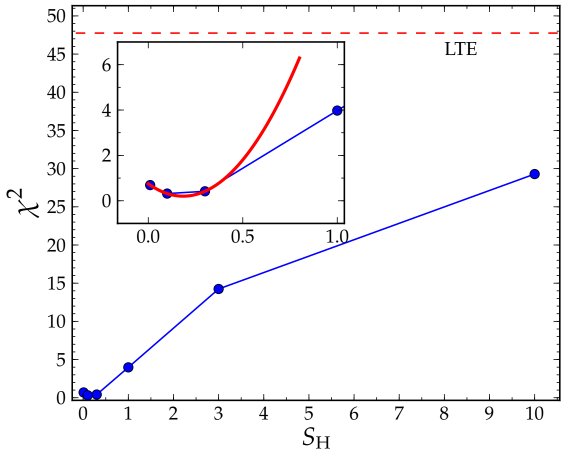

Figure A.15 Fig. 4.7, but for the old 3D model.

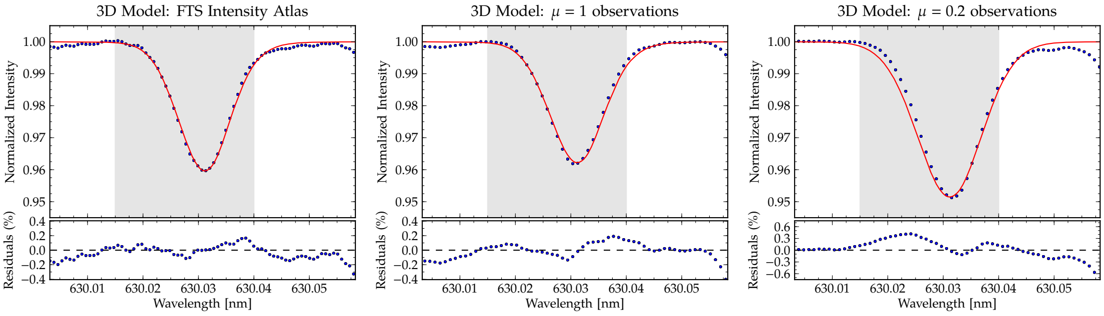

Figure A.16 Same as the first row of Fig. 4.8, but for the old 3D model.

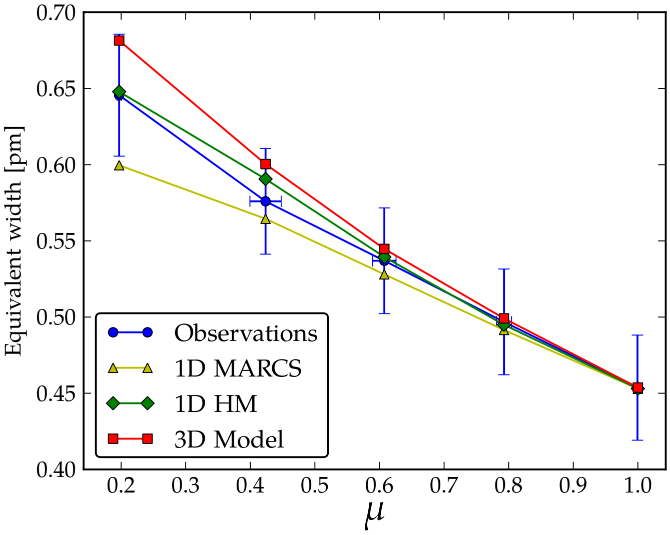

Figure A.17 Same as Fig. 4.9, but for the old 3D model.

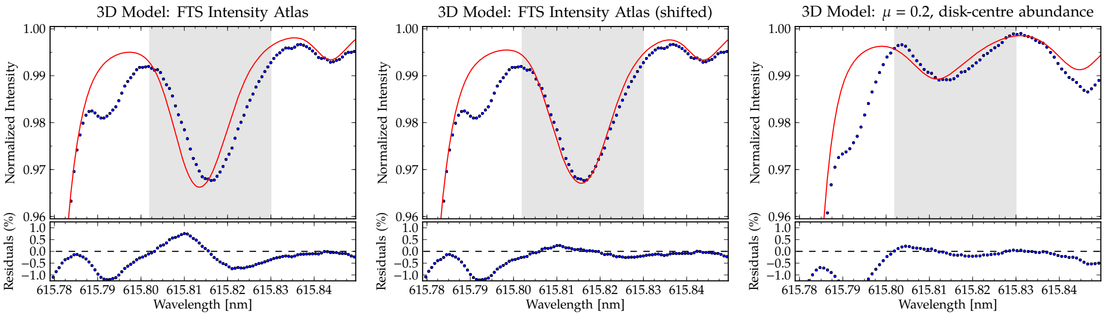

Figure A.18 Same as first row of Fig. 4.10, but for the old 3D model.

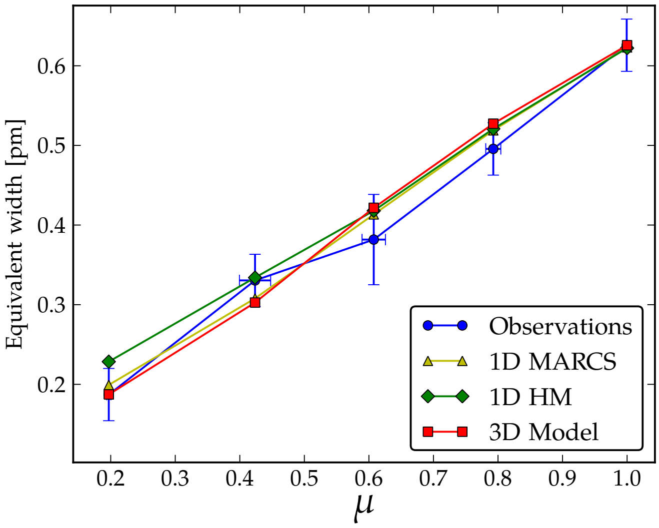

Figure A.19 Same as Fig. 4.11, but for the old 3D model.

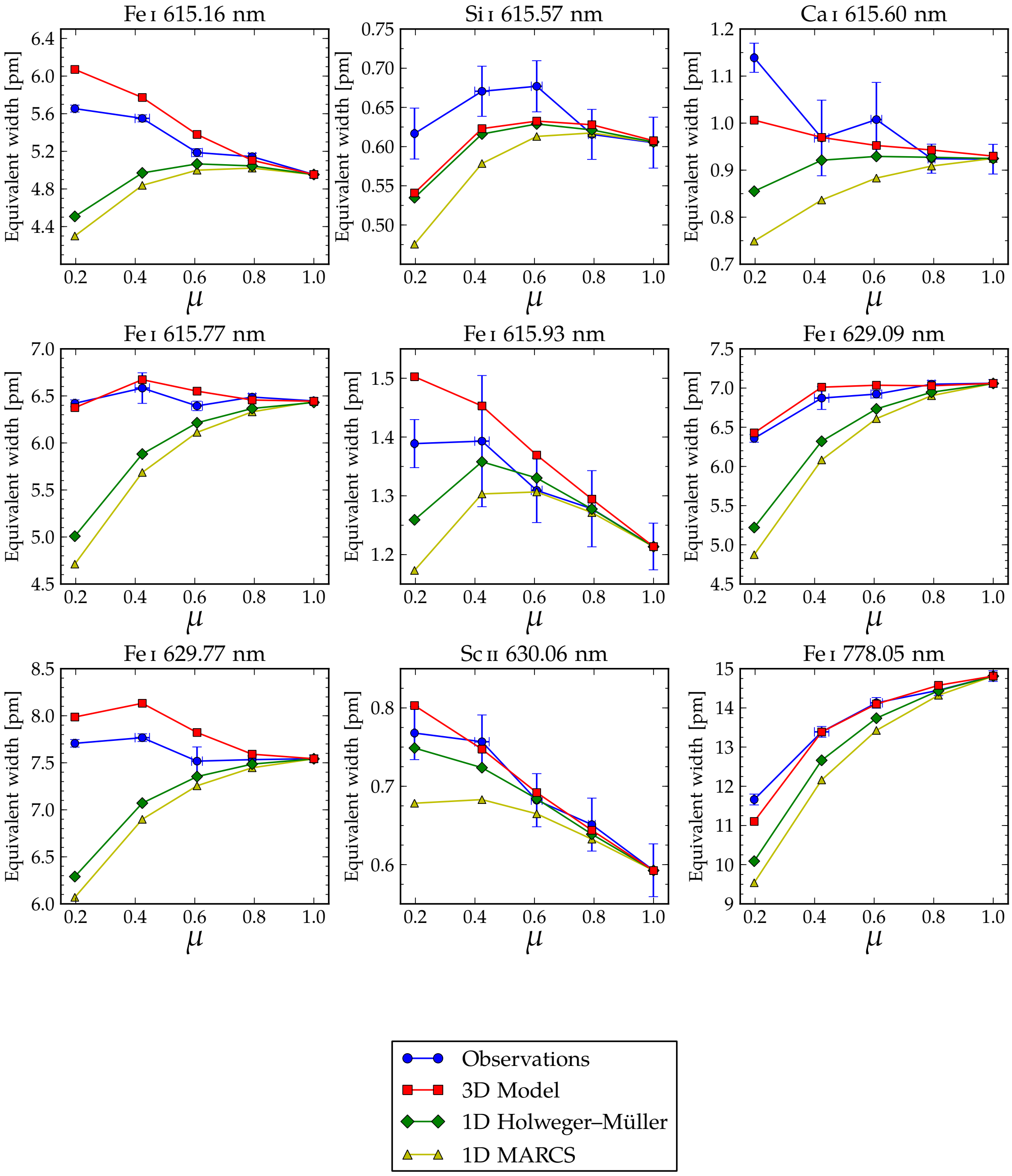

Figure A.20 Same as Fig. 4.12, but for the old 3D model.

APPENDIX B

Line quantities in solar granulation

In this appendix the line quantities in the solar granulation at high-spatial resolution are reproduced in greater detail. For the sake of brevity they were omitted from Chapter 3, where for most of the line quantities only a selection of the lines was shown. Here we shown the results for all the lines considered in the analysis (see Table 3.2), for the observations and for the 3D model.

The results are shown in the same order as they appear in Chapter 3. The line shifts are shown in three figures, for the three spectrograph regions, with the lines ordered by wavelength.

In Fig. B.6 a new quantity is shown: the relative intensity of the line minimum. This intensity is obtained, as described in Sect. 3.3.7, with the same procedure to extract the line centre wavelength – by fitting a parabola to a few points around the line minimum. This quantity reflects how the depth of each line is sensitive to the variations in the continuum intensity.

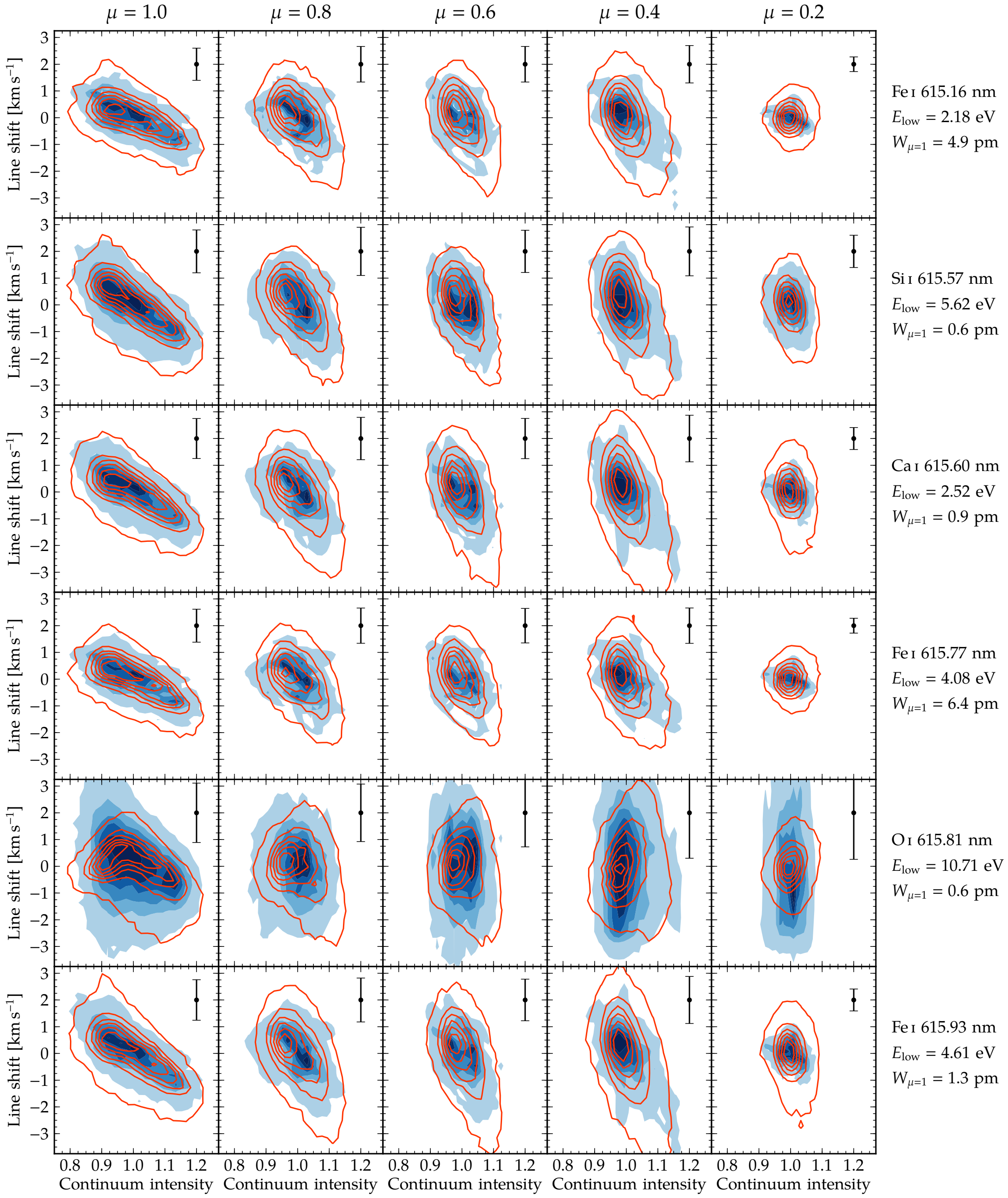

Figure B.1 Line shifts for the lines in the 615 nm region and several μ values. Legend as in Fig. 3.7.

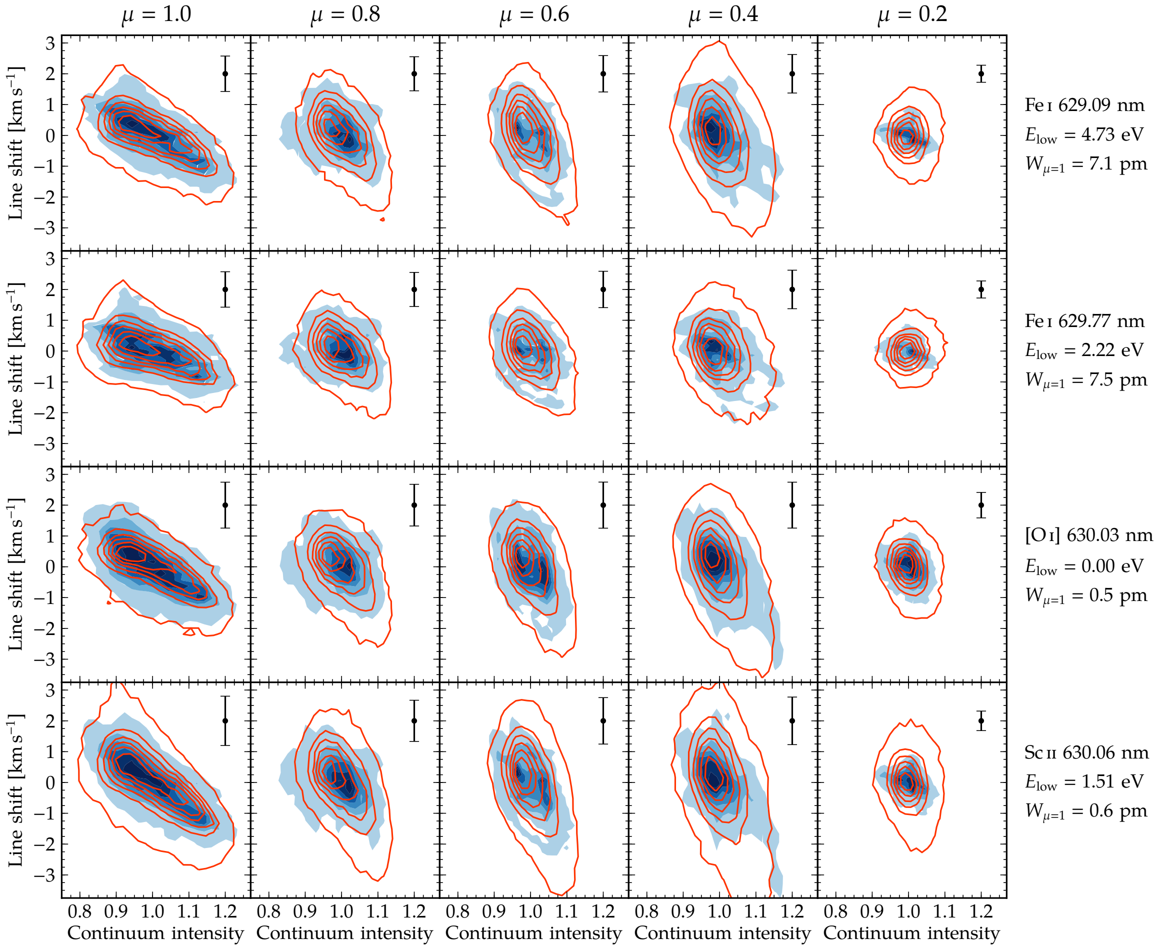

Figure B.2 Line shifts for the lines in the 630 nm region and several μ values. Legend as in Fig. 3.7.

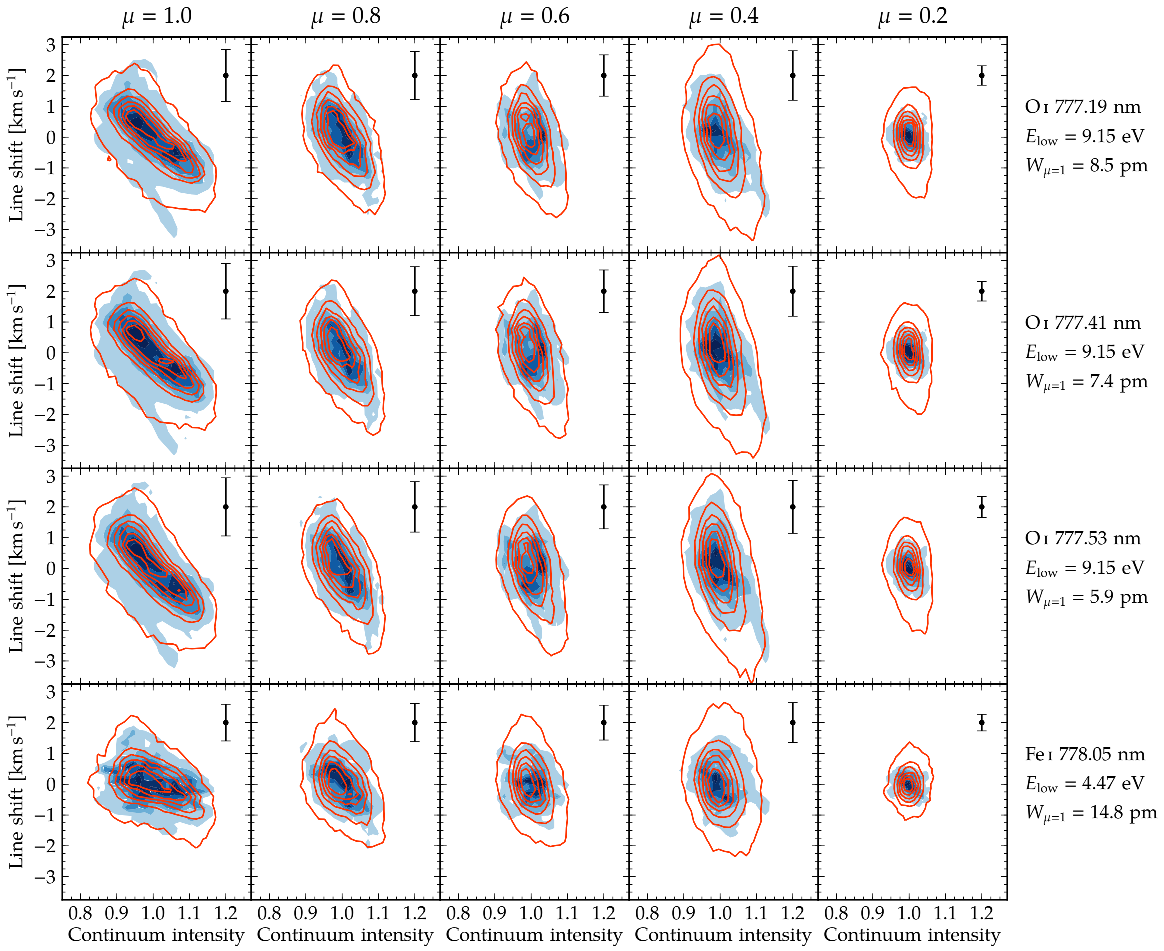

Figure B.3 Line shifts for the lines in the 777 nm region and several μ values. Legend as in Fig. 3.7.

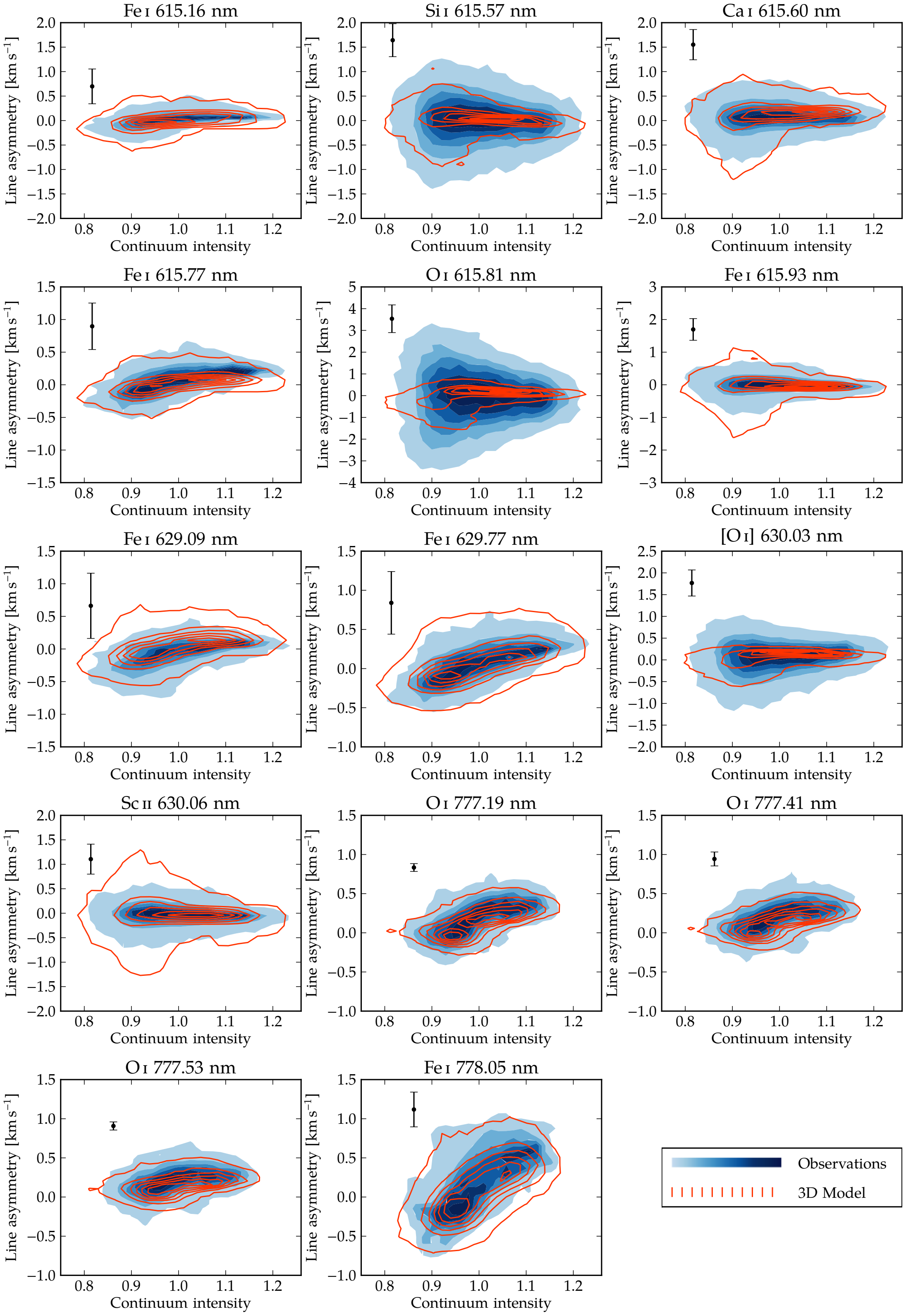

Figure B.4 Distribution of line asymmetries over the solar granulation at disk-centre. All line profiles were computed assuming LTE, except the O I 777 nm lines, showing the NLTE results for $S_H = 1$.

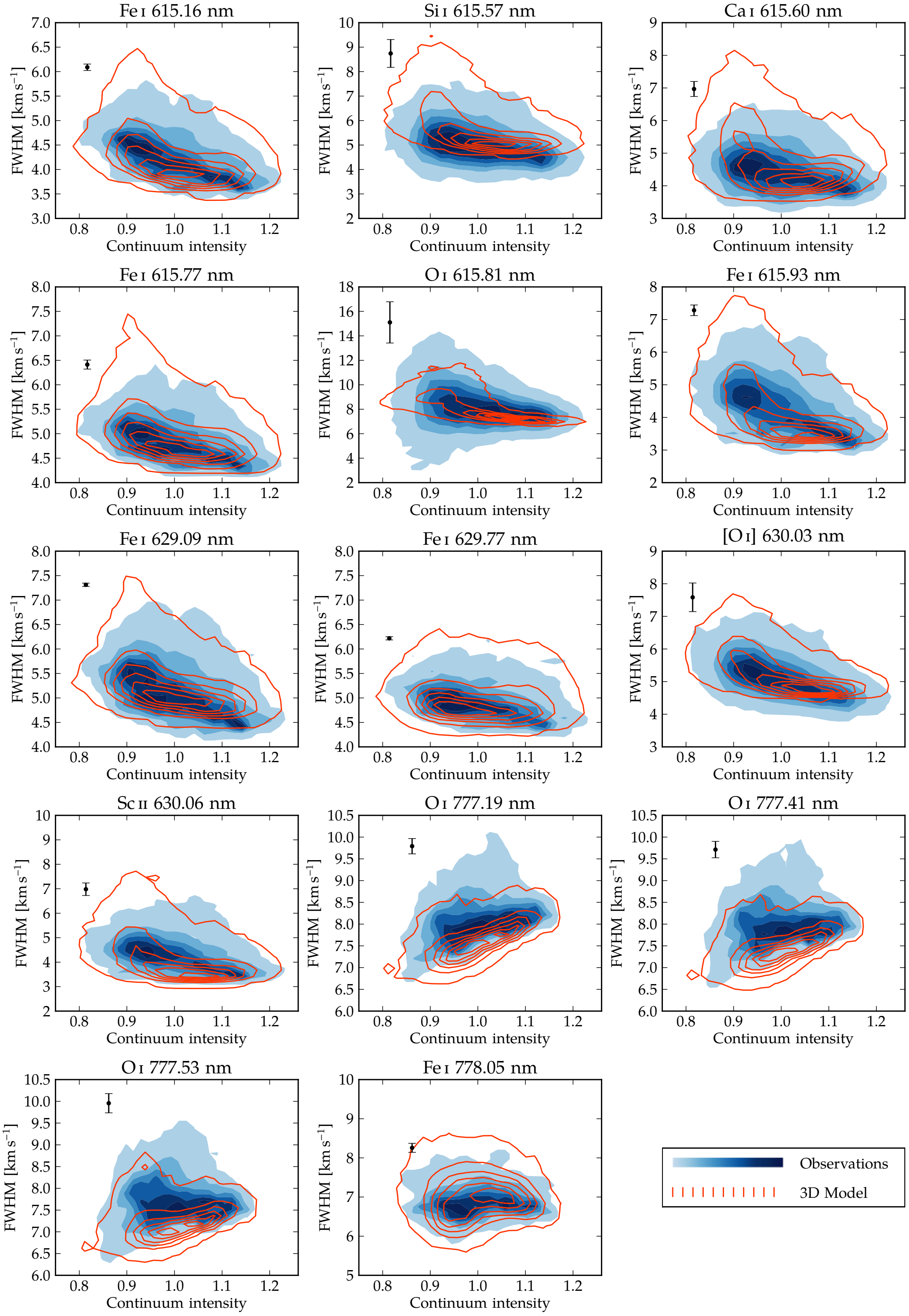

Figure B.5 Distribution of line FWHM over the solar granulation at disk-centre. All line profiles were computed assuming LTE, except the O i 777 nm lines, showing the NLTE results for $S_{\rm H} = 1$.

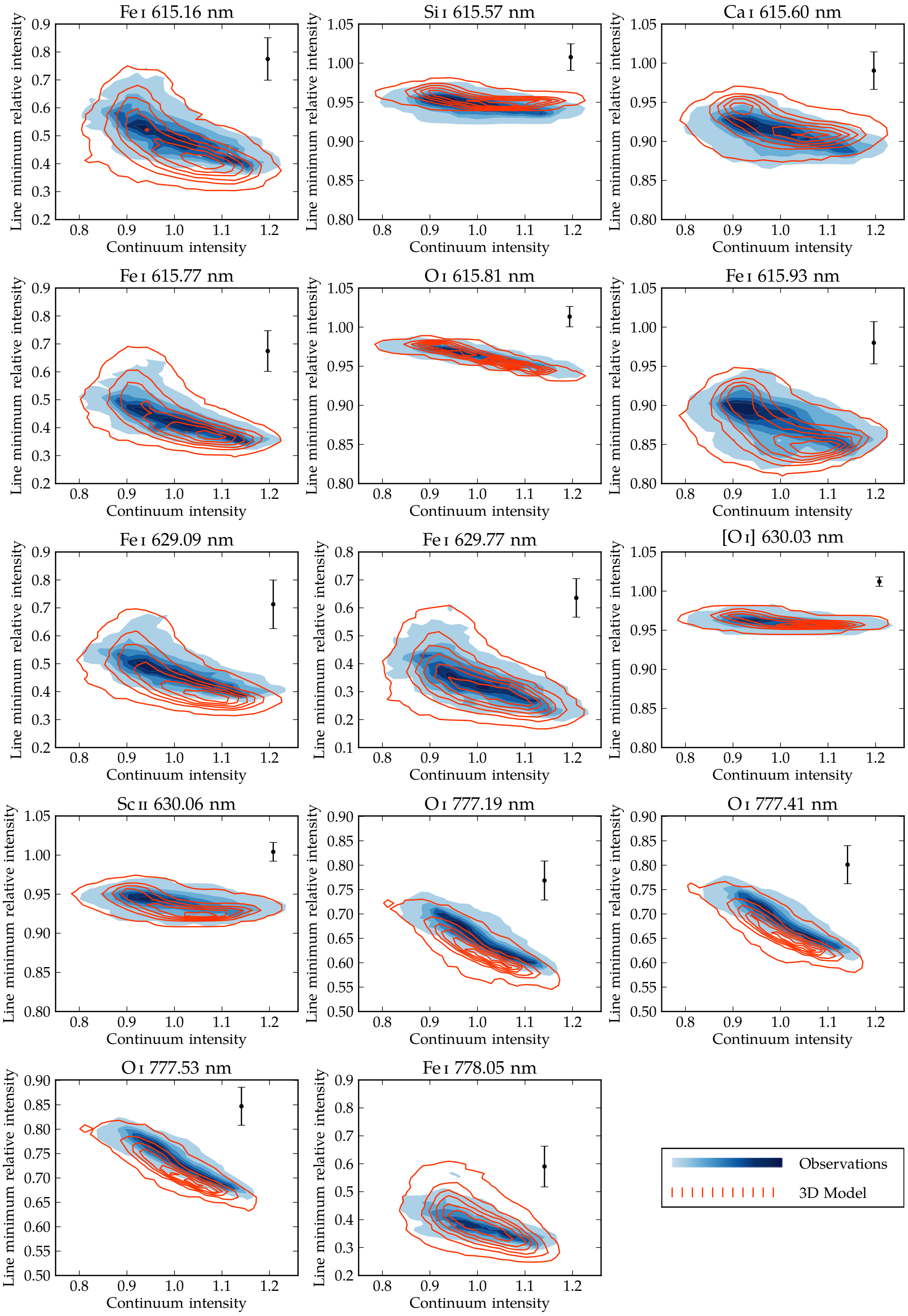

Figure B.6 Distribution of the line minimum relative intensity over the solar granulation at disk-centre. All line profiles were computed assuming LTE, except the O I 777 nm lines, showing the NLTE results for $S_{\mathrm{H}} = 1$.